





This is to certify that the dissertation entitled

THE ELECTRON PARAMAGNETIC RESONANCE CHARACTERIZATION OF FERROUS NITROSYL NON-HEME IRON MODELS AND ENZYMES

presented by

Matthew D. Krzyaniak

has been accepted towards fulfillment of the requirements for the

Ph.D degree in Chemistry

John L. McCracken Major Professor's Signature

August 30, 2010

Date

**PLACE IN RETURN BOX** to remove this checkout from your record.  
**TO AVOID FINES** return on or before date due.  
**MAY BE RECALLED** with earlier due date if requested.

<b>DATE DUE</b>	<b>DATE DUE</b>	<b>DATE DUE</b>

THE ELECTRON PARAMAGNETIC RESONANCE CHARACTERIZATION OF  
FERROUS NITROSYL NON-HEME IRON MODELS AND ENZYMES

By

Matthew D. Krzyaniak

A DISSERTATION

Submitted to  
Michigan State University  
in partial fulfillment of the requirements  
for the degree of

DOCTOR OF PHILOSOPHY

Chemistry

2010

## ABSTRACT

### THE ELECTRON PARAMAGNETIC RESONANCE CHARACTERIZATION OF FERROUS NITROSYL NON-HEME IRON MODELS AND ENZYMES

By

Matthew D. Krzyaniak

Non-heme iron oxygenases represent a class of enzyme that activate dioxygen and catalyze a diverse range of thermodynamically challenging reactions. Phenylalanine hydroxylase(PheH) is a non-heme Fe enzyme that catalyzes the hydroxylation of the C<sub>4</sub> position of the phenol side chain of phenylalanine(phe) to yield tyrosine and Tyrosine hydroxylase(TyrH) catalyzes the hydroxylation of the C<sub>3</sub> position of the phenol side chain of tyrosine(tyr) to yield L-DOPA. These two enzymes contain a highly conserved iron binding motif termed the facial triad with 2 histidine ligands and a carboxylate facially coordinating the iron. This work focuses on the EPR characterization of these two enzymes and a series of model complexes containing the same N, N, O facial binding motif. The catalytically relevant oxidation state for non-heme iron oxygenases is Fe(II) which is EPR silent, this problem was overcome by studying Fe(II)-NO complexes where the NO acts as an oxygen surrogate and couples to the Fe(II) generating an EPR active S=3/2 system. Using <sup>2</sup>H electron spin echo envelope modulation(ESEEM) spectroscopy we have shown that in TyrH and PheH there is a structural change that occurs in the active site upon substrate addition which results in movement of the pterin co-substrate closer to the Fe(II) center. <sup>2</sup>H ESEEM has also shown that in TyrH and PheH a change in the orientation of the Fe-NO bond with respect primary substrate occurs on co-substrate

binding. Hyperfine sub-level correlation spectroscopy was used to characterize the magnetic environment of the model complexes including the chelating ligand and solvent molecules. These results were applied to aid in the understanding of the HYSCORE spectra collected on TyrH and PheH.

## ACKNOWLEDGEMENTS

First and foremost I'd like thank my collaborators without whom none of this work would have been possible. My work on phenylalanine hydroxylase was in collaboration with Gülbenk Anarat, a graduate student in the lab of John Caradonna at Boston University. The non-heme iron model system was provided by Patrick Cappillino another graduate student in the Caradonna lab. The work on tyrosine hydroxylase was in collaboration with Bekir Eser, a graduate student in the lab of Paul Fitzpatrick at Texas A&M. It was through these collaborations that I was able to pursue my real interests in spectroscopy while maintaining relatively dry hands and avoiding smelly biochem labs.

I'd also like to thank my advisor John McCracken for patiently teaching me about EPR theory and instrumentation. It has been a pleasure working for/with him and I am thankful for all the knowledge and entertainment he has provided me. He has this special talent to spin the most mundane of things into an entertaining story.

Also thanks to all the friends I've made along the way at MSU, with a special shout out to the current and former members of the Weliky and McCusker groups. You helped me to maintain my sanity through grad school.

I need to put a special thanks in here to my former undergraduate mentors, Dr. Yiwei Deng and Dr. Sheila Smith of the University of Michigan – Dearborn. It was through the work in your labs that motivated me to pursue a graduate education.

Lastly my family, your support and encouragement has kept me going through school.

## TABLE OF CONTENTS

LIST OF TABLES.....	vii
LIST OF FIGURES.....	viii
LIST OF ABBREVIATIONS.....	xi
CHAPTER I	
1.1 Oxygen Activation.....	1
1.2 N,N,O Facial Triad.....	3
1.3 Structure of Tetrahydrobiopterin Dependent Hydroxylases.....	5
1.4 Mechanism.....	7
1.5 Fe-NO as a Spectroscopic Probe.....	8
1.6 Purpose.....	9
1.7 Experimental.....	9
1.7.1 TyrH Preparation.....	9
1.7.2 PheH Preparation.....	12
1.7.3 CW-EPR.....	16
1.8 Theory.....	16
1.9 Results.....	18
1.10 Simulation Notes.....	23
1.11 Discussion.....	26
1.12 Conclusions.....	32
1.13 References.....	33
CHAPTER II	
2.1 Introduction.....	38
2.2 Fe-NO Electronic Structure.....	38
2.3 N,N,O Model System.....	42
2.4 Water Analysis.....	43
2.5 Hydrogen Hyperfine Coupling.....	44
2.6 Experimental.....	47
2.7 Results.....	49
2.7.1 Ferric CW-EPR.....	49
2.7.2 {FeNO} <sup>7</sup> CW-EPR.....	51
2.7.3 {FeNO} <sup>7</sup> HYSCORE.....	52
2.7.4 Water Analysis.....	56
2.7.5 Ligand Hyperfine Analysis.....	61
2.8 Discussion.....	62
2.9 Conclusions.....	68
2.10 References.....	70
CHAPTER III	
3.1 Introduction.....	73
3.2 Experimental.....	76
3.3 Results.....	80

3.4 $^2\text{H}$ ESEEM Simulation Notes.....	85
3.5 Discussion.....	88
3.6 Conclusions.....	95
3.7 References.....	97
CHAPTER IV	
4.1 Introduction.....	100
4.2 HYSCORE Results.....	100
4.3 Histidine Hyperfine Coupling Analysis.....	103
4.4 Exchangeable Hydrogen Analysis.....	107
4.5 $^2\text{H}$ ESEEM on PheH.....	109
4.6 Conclusions.....	114
4.7 References.....	115
APPENDIX I	
MATLAB Simulation Scripts.....	116
APPENDIX II	
Electron Spin Echo Envelope Modulation Spectroscopy.....	124

## LIST OF TABLES

Table 1.1: Simulation Parameters for TyrH.....	23
Table 1.2: Simulation Parameters for PheH.....	23
Table 2.1: {FeNO} <sup>7</sup> Formalisms.....	39
Table 3.1: Deuterium Hyperfine Couplings.....	89

LIST OF FIGURES  
Images in this dissertation are presented in color

Figure 1.1: General Oxygenase Mechanism.....	2
Figure 1.2: Tetrahydrobiopterin Dependent Aromatic Amino Acid Hydroxylases.....	4
Figure 1.3: Mechanism for Tetrahydrobiopterin Dependent Aromatic Amino Acid Hydroxylases.....	8
Figure 1.4: CW-EPR Spectra of TyrH.....	19
Figure 1.5: CW-EPR Spectra of PheH.....	21
Figure 1.6: CW-EPR Spectra of $\Delta$ PheH.....	22
Figure 2.1: Structures of $\text{FeN}_2\text{O}_1$ , $\text{FeN}_2\text{O}_2$ and $\text{FeN}_2\text{O}_3$ .....	42
Figure 2.2: CW-EPR of ferric $\text{N}_2\text{O}_1$ , $\text{N}_2\text{O}_2$ , and $\text{N}_2\text{O}_3$ .....	50
Figure 2.3: CW-EPR of $\{\text{FeNO}\}^7\text{N}_2\text{O}_1$ , $\text{N}_2\text{O}_2$ , and $\text{N}_2\text{O}_3$ .....	51
Figure 2.4: HYSCORE spectrum of $\{\text{FeNO}\}^7\text{-N}_2\text{O}_1$ recorded at 1980 G.....	53
Figure 2.5: HYSCORE spectrum of $\{\text{FeNO}\}^7\text{-N}_2\text{O}_1$ recorded at 3100 G.....	53
Figure 2.6: HYSCORE spectrum of $\{\text{FeNO}\}^7\text{-N}_2\text{O}_2$ recorded at 1980 G.....	54
Figure 2.7: HYSCORE spectrum of $\{\text{FeNO}\}_7\text{-N}_2\text{O}_2$ recorded at 3100 G.....	54
Figure 2.8: HYSCORE spectrum of $\{\text{FeNO}\}^7\text{-N}_2\text{O}_3$ recorded at 1980 G.....	55
Figure 2.9: HYSCORE spectrum of $\{\text{FeNO}\}^7\text{-N}_2\text{O}_3$ recorded at 3100 G.....	56
Figure 2.10: HYSCORE spectrum of $\{\text{FeNO}\}^7\text{-N}_2\text{O}_1$ in $\text{D}_2\text{O}$ recorded at 3100 G.....	57
Figure 2.11: HYSCORE spectrum of $\{\text{FeNO}\}^7\text{-N}_2\text{O}_1$ recorded at 2800 G.....	58
Figure 2.12: HYSCORE spectrum of $\{\text{FeNO}\}^7\text{-N}_2\text{O}_1$ recorded at 2900 G.....	58
Figure 2.13: HYSCORE spectrum of $\{\text{FeNO}\}^7\text{-N}_2\text{O}_1$ recorded at 3000 G.....	59
Figure 2.14: HYSCORE spectrum of $\{\text{FeNO}\}^7\text{-N}_2\text{O}_1$ recorded at 3100 G.....	59

Figure 2.15: HYSCORE spectrum of $\{\text{FeNO}\}^7\text{-N}_2\text{O}_1$ recorded at 3200 G.....	59
Figure 2.16: $^1\text{H}$ HYSCORE simulation at 2800 G.....	60
Figure 2.17: $^1\text{H}$ HYSCORE simulation at 2900 G.....	60
Figure 2.18: $^1\text{H}$ HYSCORE simulation at 3000 G.....	60
Figure 2.19: $^1\text{H}$ HYSCORE simulation at 3100 G.....	61
Figure 2.20: $^1\text{H}$ HYSCORE simulation at 3200 G.....	61
Figure 2.21: $^{14}\text{N}$ HYSCORE simulation at 3100 G.....	62
Figure 3.1: TyrH reaction.....	73
Figure 3.2: TyrH Catalytic Mechanism.....	74
Figure 3.3: Representative $^2\text{H}$ ESEEM of $\{\text{FeNO}\}^7$ TyrH treated with d-6MPH <sub>4</sub> and treated with d-6MPH <sub>4</sub> and tyr.....	81
Figure 3.4: Representative $^2\text{H}$ ESEEM of $\{\text{FeNO}\}^7$ TyrH treated with d-tyr and treated with 6MPH <sub>4</sub> and d-tyr.....	83
Figure 3.5: Representative $^2\text{H}$ ESEEM of the $\{\text{FeNO}\}^7$ TyrH mutant E332A.....	84
Figure 3.6: $^2\text{H}$ simulations with an angle between the dipole vector and $g_z$ of 0.3 rad.....	86
Figure 3.7: $^2\text{H}$ simulations with an angle between the dipole vector and $g_z$ of 1.3 rad.....	86
Figure 3.8: Summary of ESEEM Results.....	94
Figure 4.1: HYSCORE spectrum of TyrH[6MPH <sub>4</sub> ,tyr] at 1980 G.....	101
Figure 4.2: HYSCORE spectrum of TyrH[6MPH <sub>4</sub> ,tyr] at 3100G.....	101
Figure 4.3: HYSCORE spectrum of PheH[Phe, 5d] at 1980 G.....	102
Figure 4.4: HYSCORE spectrum of PheH[Phe, 5d] at 3100G.....	103
Figure 4.5: $^1\text{H}$ HYSCORE simulations for TyrH at 1980 G and 3100 G.....	104
Figure 4.6: $^1\text{H}$ HYSCORE simulations for PheH at 1980 G and 3100 G.....	105
Figure 4.7: $^{14}\text{N}$ HYSCORE simulations at 3100 G.....	106

Figure 4.6: $^1\text{H}$ HYSCORE simulations at 3100 G for TyrH and PheH.....	107
Figure 4.9: $^2\text{H}$ ESEEM collected on PheH[d-5d] and PheH[d-5d, phe].....	110
Figure 4.10: $^2\text{H}$ ESEEM collected on $\Delta\text{PheH[d-5d]}$ and $\Delta\text{PheH[d-5d, phe]}$ .....	111
Figure 4.11: $^2\text{H}$ ESEEM collected on PheH[d-phe].....	113
Figure A2.1: Energy level diagram and corresponding EPR spectrum.....	125
Figure A2.2: EPR pulse sequences.....	126

## LIST OF ABBREVIATIONS

5d – 5-deaza-6MPH<sub>4</sub>

6MPH<sub>4</sub> – 6-Methyltetrahydropterin

CT – Charge Transferred

CW-EPR – Continuous Wave EPR

d-5d – <sup>2</sup>H-5-deaza-6MPH<sub>4</sub>

d-6MPH<sub>4</sub> – 6-CH<sub>3</sub>-6,7-<sup>2</sup>H-tetrahydropterin

d-phe – L-para-<sup>2</sup>H-Phenylalanine

d-tyr – L-3,5-<sup>2</sup>H-Tyrosine

DOPA – dihydroxy-phenylalanine

EPR – Electron Paramagnetic Resonance

ESEEM – Electron spin echo envelope modulation

EXAFS – Extended X-ray absorption fine structure

FWHM – Full-width half-max

HYSCORE – Hyperfine sub-level correlation

MCD – Magnetic circular Dichroism

PheH – Phenylalanine Hydroxylase

phe – Phenylalanine

PKU – Phenylketonuria

TrpH – Tryptophan Hydroxylase

tyr – Tyrosine

TyrH – Tyrosine Hydroxylase

## XAS – X-ray absorption spectroscopy

**CHAPTER I**  
**CONTINUOUS WAVE ELECTRON PARAMAGNETIC RESONANCE**  
**INVESTIGATION OF TWO AROMATIC AMINO ACID HYDROXYLASES**

**1.1 OXYGEN ACTIVATION**

Molecular oxygen serves as the terminal electron acceptor in a variety of biological processes and serves as the source for the oxygen found in many essential molecules in nature.<sup>1</sup> Thermodynamically, the cleaving of the oxygen-oxygen bond of molecular oxygen and its subsequent reaction with organic molecules is energetically favorable.<sup>2</sup> The thermodynamics are held in check by the slow reactivity of oxygen at ambient temperatures. If this weren't the case, organic molecules would spontaneously oxidize making our atmosphere deadly to life. Thankfully, there is a spin mismatch between the ground states, dioxygen is a triplet while most organic molecules tend to have a singlet ground state, this results in slow kinetic reactivity between the two.<sup>3</sup> To overcome this kinetic barrier, nature has developed a variety of catalysts in the form of metalloenzymes.<sup>4</sup> Transition metals such as iron or copper are able to coordinate the triplet oxygen and through electron transfer processes are able to activate the oxygen and form intermediates that can participate in reactions with organic substrates.<sup>5</sup> This work is focused on these metalloenzymes and specifically those containing a non-heme iron, so only that aspect of oxygen activation will be further discussed.

The mono-nuclear metalloenzymes which incorporate oxygen atoms into organic molecules can broadly be classified as oxygenases and can be sub divided into two

different classes, mono-oxygenases and di-oxygenases. These two classes of oxygenases are distinguished by the number of oxygen atoms that they incorporate into the organic substrate, mono-oxygenases add a single oxygen atom to the product, on the other-hand both oxygen's are added to the substrates in di-oxygenases. The di-oxygenases can be divided further into two groups intra-molecular di-oxygenases in which both oxygen atoms are incorporated into a single product and inter-molecular di-oxygenases which utilize a second substrate which is also hydroxylated. <sup>2</sup>

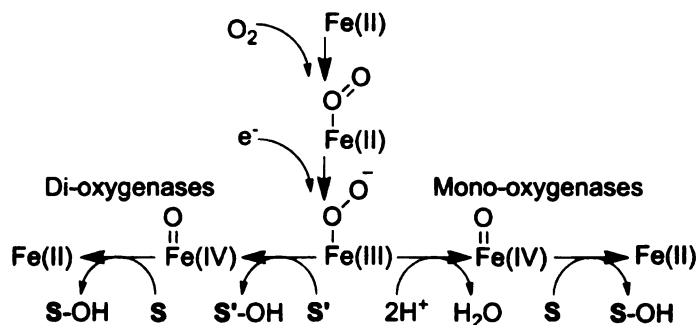


Figure 1.1: General Oxygenases Mechanism

A general mechanism for the reaction of mono-nuclear oxygenases is shown in figure 1.1.<sup>3</sup> The mono-nuclear oxygenases function, first, through the direct binding of dioxygen to the metal in the active site. Many of the proposed mechanisms suggest that the oxygen is then reduced by two electrons, one provided by the metal and the other from a co-factor or co-substrate.<sup>1</sup> This intermediate, a ferric peroxy adduct, contains an activated oxygen that can now readily participate in chemical reactions. In the case of the monooxygenases, this adduct is doubly protonated, releasing a water molecule and forming what has been proposed as a high-valent ferryl-oxo intermediate. This iron-oxo intermediate is highly reactive and will readily hydroxylate unactivated organic

substrates.<sup>3</sup> The di-oxygenases are suggested to proceed through a very similar mechanism, instead of the release of water, the ferric peroxy adduct reacts directly with the substrate.<sup>1,3</sup> In both cases, the systems are generally designed to tightly control this oxygen activation and minimize side reactions.<sup>6</sup>

## 1.2 N,N,O FACIAL TRIAD

Based on structural studies of non-heme iron(II) oxygenases, a common structural motif has emerged as the foundation for catalyzing a highly versatile group of chemical reactions.<sup>7</sup> This motif coordinates the iron with 2 histidines and a carboxylate in a facial fashion, leaving three labile coordination sites onto which substrates or co-substrates can bind. This coordination geometry represents a contrast to the heme oxygenases which generally only have one open coordination site where oxygen binds.<sup>5</sup> As a result the non-heme Fe di-oxygenases allow for a very different set of hydroxylation reactions than the heme oxygenases.<sup>8</sup> However, these non-heme di-oxygenases have not been studied nearly as extensively as their heme counterparts.<sup>9</sup> The non-heme iron active sites have ligands that do not exhibit the intense  $\pi \rightarrow \pi^*$  absorption features seen from the porphyrin ligand in the heme enzymes.<sup>10</sup> In addition, the reduced Fe(II) sites do not exhibit charge transfer (CT) transitions and are generally not detectable by Electron Paramagnetic Resonance(EPR), and while the oxidized Fe(III) sites do exhibit EPR signals reflecting spin Hamiltonian parameters and CT features, their information content has not been developed.<sup>11</sup>

One particularly interesting family of mono-nuclear non-heme iron hydroxylases uses the co-factor tetrahydrobiopterin as a reductant to catalyze the hydroxylation of

aromatic amino acids.<sup>12 13</sup> This family of tetrahydrobiopterin dependent aromatic amino acid hydroxylases includes tyrosine hydroxylase(TyrH), phenylalanine hydroxylase(PheH) and tryptophan hydroxylase(TrpH), each of which catalyze a very important hydroxylation reaction that can be seen in figure 1.2.<sup>14 15</sup>

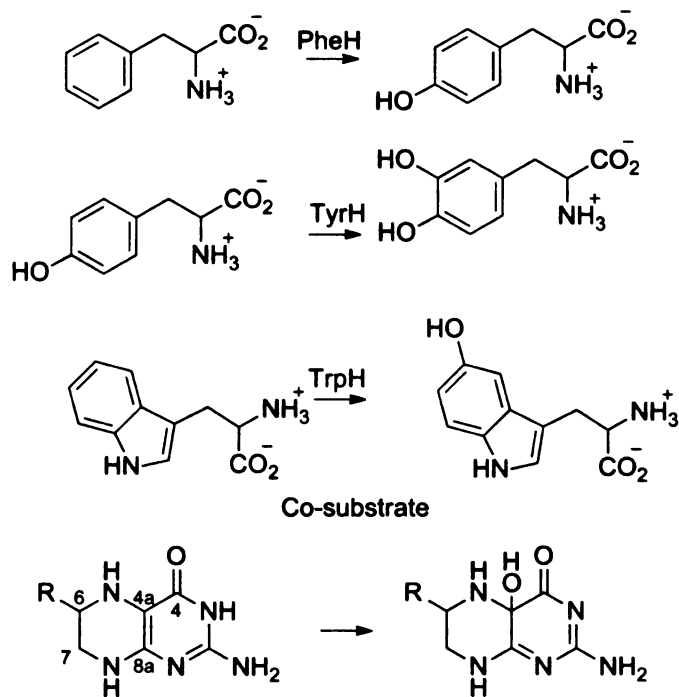


Figure 1.2: Tetrahydrobiopterin Dependent Aromatic Amino Acid Hydroxylases

TyrH catalyzes the hydroxylation of tyrosine into dihydroxy-phenylalanine(DOPA), this reaction is the rate limiting step to the biosynthesis of the catecholamine neurotransmitters which includes dopamine, norepinephrine and epinephrine.<sup>13</sup> This enzyme has been implicated with a number of neurological disorders such as Parkinson's or Segawa's syndrome, both of which have been successfully treated with DOPA replacement therapy.<sup>12</sup> Dysfunction of PheH causes Phenylketonuria(PKU), a disorder

which manifests itself in severe mental retardation caused by the neurotoxicity of phe and its metabolites.<sup>12</sup> TrpH produces 5-hydroxytryptophan, the precursor and rate limiting step for the biosynthesis of serotonin and melatonin.<sup>13</sup> Understanding the structural characteristics of these three enzymes will be important for addressing a range of different neurological and psychological disorders.

### **1.3 STRUCTURE OF TETRAHYDROBIOPTERIN DEPENDENT HYDROXYLASES**

Crystal structures have been described for the three aromatic amino acid hydroxylases. These crystal structures have largely been determined for different truncated variants of the inactive oxidized enzyme containing Fe(III). PheH is one exception, three structures exist of the truncated catalytic domain which contains Fe(II). One structure is of the binary complex with co-substrate, tetrahydrobiopterin(PDB:1J8U),<sup>16</sup> the other two are of the ternary complexes with co-substrate, BH<sub>4</sub>, and primary substrate analogs thienylalanine(PDB:1KW0,1MMK)<sup>17</sup> or norleucine(PDB:1MMT)<sup>18</sup>. In addition to these ferrous structures, a number of lower resolution ferric structures exist for PheH. The other two enzymes, TyrH and TrpH, have not been crystallographically characterized to the same extent as PheH. The catalytic domain of ferric TyrH, with(PDB:1TOH)<sup>19</sup> and without the co-substrate(PDB:2TOH)<sup>20</sup> have been reported. TrpH has been crystallized in the ferric form with co-substrate(PDB:1MLW)<sup>21</sup> and with primary substrate trp(PDB:3E2T)<sup>22</sup>.

All three hydroxylases have significant sequence similarity and based on the above structural studies have shown structural homology of their catalytic cores.<sup>13</sup> Based

on these two pieces of evidence and the similarity of the chemical reaction of these enzymes much of what has been learned from the more characterized PheH has been used interchangeably with the other two enzymes in the family.<sup>6</sup>

A comparison of the catalytic domain of ferric PheH to that of ferrous PheH shows no difference in the relative structure at the active site.<sup>16,23</sup> This comparison however is only of the binary enzyme with co-substrate, so while no large scale changes are observed in the catalytic domain, this does not necessarily translate to the ternary or quaternary complex.

Examination of the PheH crystal structures show a range of structural changes in the catalytic core as a result of substrate and co-substrate binding.<sup>18,17</sup> For example comparison of the binary PheH structure with that of the ternary enzyme reveals that a flexible loop consisting of residues 131-145 and specifically Y138 packs against the amino acid binding site.<sup>17</sup> A site directed mutagenesis study on the analogous loop in TyrH indicated that the residue analogous to Y138 was responsible for optimizing the coupling between co-substrate oxidation and the hydroxylation of primary substrate.<sup>24</sup> Further fluorescence anisotropy studies suggest that presence of the pterin modulates the motion of this loop.<sup>25</sup>

A second important observation from the PheH crystal structures is that the presence of the primary substrate affects a change in the active site which brings the position of the pterin closer to the iron. The binary structure of PheH has a distance of 6 Å between the Fe and the position of the pterin that gets hydroxylated, the C<sub>4a</sub> position. Comparison of the binary enzyme to the ternary enzyme shows that binding of the amino

acid decreases this distance to 4.5 Å. Thus, the binding of the amino acid substrate analog initiates a conformational change in PheH that pushes the pterin co-substrate closer to the iron.<sup>17</sup>

Interestingly, in the ternary crystal structure, the pterin co-substrate and the primary substrate never directly coordinate the iron. These substrates do however, displace two of the iron coordinating solvent molecules, leaving the iron five coordinate: 2 his, 1 glu(bound bidentate) and a single water. The pterin is positioned in the active site through a network of hydrogen bonds to the enzyme backbone consisting of residues 248-251. On addition of substrate, the pterin is brought closer to the iron by a movement of the backbone and its position near the iron is defined by hydrogen bonding to glu286. This movement of the pterin displaces two solvent molecules. The Fe ligands, Glu330 and His285, together with the pterin approximately form a plane perpendicular to the third Fe ligand, His290. There is no structural evidence in regard to primary substrate binding in the absence of co-substrate; however, in the ternary complex, the substrate analog was seen to bind in a relatively hydrophobic pocket, stacking on His285 and positioning it near the remaining open coordination site. Both substrate and co-substrate must be present for enzyme turnover.

#### **1.4 MECHANISM**

Based on the general mechanism given above and what is known about the structure and reaction products, a specific chemical mechanism for the action of the tetrahydrobiopterin aromatic amino acids has been proposed. Seen in figure 1.3 is the proposed mechanism for the hydroxylation of phe in PheH.<sup>13</sup> The cycle begins when both

substrate and co-substrate bind in the enzyme, this binding converts the iron from 6 to 5 coordinate providing an open coordination site to accommodate oxygen. This portion of the mechanism is supported by both the crystal structure evidence and other spectroscopic techniques including MCD.<sup>26</sup>

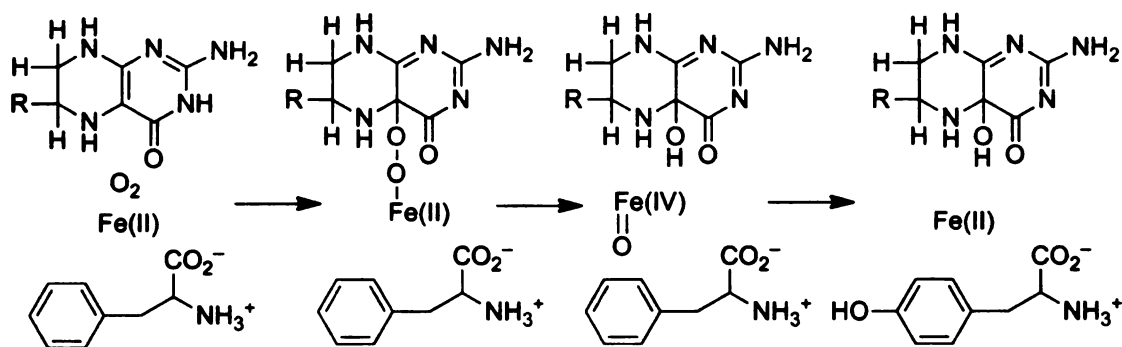


Figure 1.3: Mechanism for Tetrahydrobiopterin Dependent Aromatic Amino Acid Hydroxylation

Following oxygen binding to the iron, an iron-peroxy-pterin species forms, oxidizing the pterin and reducing the di-oxygen.<sup>15a, 27</sup> The iron-peroxy-pterin species undergoes heterolytic bond cleavage producing 4a-hydroxypterin and an Fe(IV)-oxo species.<sup>28</sup> An electrophilic substitution reaction occurs between the ferryl-oxo intermediate and the substrate that then undergoes a 1,2-hydrogen shift and tautomerization to yield the hydroxylated amino acid product.<sup>29, 6, 30</sup> After this electrophilic substitution the ferrous enzyme is regenerated.

### 1.5 Fe-NO AS A SPECTROSCOPIC PROBE

As suggested by the mechanism, the ferrous oxidation state is the catalytically relevant form of iron in these enzymes and as mentioned above, spectroscopically studying the enzymes in this oxidation state is challenging. One method, first utilized in

the study of heme's and later in non-heme systems, involves binding the iron with nitric oxide.<sup>31</sup> The binding of NO to the iron serves two purposes: first, NO acts as an oxygen surrogate binding in a similar fashion competitively blocking oxygen binding<sup>32</sup>; second, the NO antiferromagnetically couples with the iron converting the EPR silent  $S = 2$  metal into an EPR active  $S = 3/2$  complex.<sup>31</sup> This method has been used in a recent study by the Abu-Omar group to examine a strain of bacterial PheH.<sup>33</sup> They presented evidence that in the ternary complex NO mimics O<sub>2</sub> binding and displaces the sole water molecule observed in the crystal structure.<sup>33</sup>

## **1.6 PURPOSE**

In this thesis, the Fe(II)-NO complex will be used to study the tetrahydrobiopterin dependent aromatic amino acid hydroxylases using a variety of EPR methods. Through collaborations, our group has obtained two of the three hydroxylases, TyrH and PheH. As an initial experiment to determine if we could produce the Fe(II)-NO adduct for both of these enzymes, continuous wave EPR experiments were performed. These experiments will tell us if we were successful in producing an EPR active species and if there are quantifiable changes in the spectrum due to substrate interactions.

## **1.7 EXPERIMENTAL**

### **1.7.1 TyrH PREPARATION**

6-Methyltetrahydropterin (6MPH<sub>4</sub>) and 6-methylpterin were purchased from Schircks Laboratories (Jona, Switzerland). 6-(2-Hydroxy-1-methyl-2-nitrosohydrazino)-N-methyl-hexanamine (MAHMA NONOate), ethylenediamine tetraacetic acid (EDTA), 3-(N-morpholino)propanesulfonic acid (Mops), L-tyrosine and glycerol were purchased from

Sigma-Aldrich (St. Louis, MO). L-3,5-<sup>2</sup>H-Tyrosine and deuterium gas were from Cambridge Isotopes (Andover, MA). Potassium chloride and ferrous ammonium sulfate were from Fisher (Pittsburg, PA). 6-CH<sub>3</sub>-6,7-<sup>2</sup>H-tetrahydropterin (d-6MPH<sub>4</sub>) was synthesized by reduction of the commercially available 6-methylpterin to the level of tetrahydropterin using deuterium gas, as previously described.<sup>34</sup> All other chemicals were of the highest purity commercially available.

Wild-type TyrH was expressed in *E. coli* and purified as previously described.<sup>35 36</sup> In order to remove the ferric iron from the protein, the ammonium sulfate pellet at the end of the purification was resuspended in 5 mM EDTA, 200 mM Hepes, (pH 7.5), 10% glycerol and 0.1 M KCl, and incubated on ice for one hour. The enzyme solution was then dialyzed against the same buffer without EDTA and concentrated using Amicon Ultra-15 and Ultra-4 centrifugal filters (Millipore Corp., MA). The enzyme samples for ESEEM were brought to a final glycerol concentration of 30% (v/v) during the concentration stage. The iron content of the apo-enzyme was measured using a Perkin-Elmer Analyst 600 atomic absorption instrument.<sup>37</sup> The typical iron content of an apo enzyme preparation was  $\leq 0.1$  equivalent.

NO Samples for EPR were prepared using MAHMA NONOate as the nitric oxide donor. Stock solutions of MAHMA NONOate were prepared in 0.01 M NaOH just before the experiment and were always kept on ice. Exact concentrations of the MAHMA NONOate solutions were determined from the UV absorbance at 250 nm in 0.01 M KOH, using an extinction coefficient of 7.3 mM<sup>-1</sup>cm<sup>-1</sup>.<sup>38</sup> Highly concentrated stock solutions of tyrosine and 3,5-<sup>2</sup>H-tyrosine (~50 mM) were prepared by bringing the

solution to a final pH of ~10. The exact concentrations of the tyrosine stock solutions were determined using an extinction coefficient of  $1.34 \text{ mM}^{-1}\text{cm}^{-1}$  at 275 nm in 0.1 M HCl. Stock solutions of the protiated and deuterated  $6\text{MPH}_4$  were prepared in 2 mM HCl, and an extinction coefficient of  $17.8 \text{ mM}^{-1}\text{cm}^{-1}$  in 2 M perchloric acid was used to determine the concentrations. Ferrous ammonium sulfate solutions were prepared fresh by dissolving the appropriate amount of powder in 2 mM HCl. ESEEM samples were prepared inside an anaerobic cuvette at 25 °C. Apo-TyrH (0.9-1.2 mM) and tyrosine (if the complex contained tyrosine) were placed at the bottom of the cuvette. Ferrous ammonium sulfate solution (0.9 equivalent in ~10  $\mu\text{l}$ ) was placed on the lower neck of the cuvette.  $6\text{MPH}_4$  and MAHMA NONOate solutions were either placed in the side arms or on the upper neck of the cuvette, for large and small volumes, respectively. Buffer conditions were 100 mM Mops (pH 7.0), 0.3 M KCl and 30% glycerol. Each MAHMA NONOate molecule releases two molecules of  $\text{NO}$ ,<sup>38</sup> and the half-life of MAHMA NONOate is ~35 s under these buffer and temperature conditions (data not shown). The contents of the cuvette (a total volume of ~250  $\mu\text{l}$ ) were made anaerobic by the application of argon-vacuum exchange for at least 20 minutes. The anaerobic enzyme solution was then mixed with ferrous ammonium sulfate and incubated for 10 minutes. This was followed by mixing with  $6\text{MPH}_4$  (if the complex contained  $6\text{MPH}_4$ ). After a few minutes of incubation, MAHMA NONOate (~0.6 equivalent of the enzyme) at the upper neck of the cuvette was introduced to the enzyme-substrate mixture. After ~3 minutes, ~200  $\mu\text{l}$  of the reaction mixture was quickly transferred to the quartz EPR tubes (4 mm OD, 707-SQ-250M, Wilmad, Buena, NJ) using a glass pipette and immediately

frozen in liquid nitrogen. (UV-Visible experiments performed under similar conditions indicated that the maximum absorbance at 450 nm, which is indicative of NO binding, was reached at about 3 minutes and stayed constant for at least a few minutes). UV-Visible spectra collected at increasing concentrations of MAHMA NONOate showed that NO was saturating under the concentrations used.

### 1.7.2 PheH Preparation

All commercial reagents were of the highest grade available and were used without further purification, with the exception of glycerol, which was treated with activated carbon to remove contaminants<sup>39</sup>. Glycerol, L-Phe, 4-morpholinepropanesulfonic acid (MOPS), KCl, sodium dithionite, ascorbate, sodium nitrite, ferrous ammonium sulfate, *p*-I-L-Phe, were from Sigma (St. Louis, MO). Phenylsepharose and Superdex 200 were purchased from Pharmacia (Uppsala, Sweden). D<sub>2</sub>O (99.9 atom % D) and *per*-<sup>2</sup>H-L-Phe were from Cambridge Isotopes Laboratories (Andover, MA). Diethylamine NONOate (DEA/NO) was purchased from Cayman Chemicals (Ann Arbor, MI). 6-MPH<sub>4</sub><sup>40</sup> and 5-deaza-6-MPH<sub>4</sub><sup>41</sup> was synthesized and characterized by standard methods<sup>42</sup> and was stored at -20°C until use. 5-deaza-6-CH<sub>3</sub>-5,6,7,8-<sup>2</sup>H-pterin (<sup>2</sup>H-5-deaza-6MPH<sub>4</sub>) was synthesized as previously described<sup>41</sup>, except that deuterium gas is used in the reduction step. The *para*-<sup>2</sup>H-L-phe was also synthesized as previously described<sup>43</sup> using *p*-I-L-phe as the starting material. *E.coli* cells were grown in a New Brunswick Bioflo 2000 fermentor (Edison, NJ). Total iron content of samples were routinely quantified using a Varian AA280 atomic absorption spectrometry, with Zeeman GTA120Z graphite furnace attachment, at 248.3 nm. The iron standard was purchased from Fisher (Pittsburgh, PA).

Automated protein purification was performed using a Pharmacia LKB FPLC (Uppsala, Sweden). All electronic absorption spectroscopy (UV/Vis) analyses were performed on a HP-8453 diode array spectrophotometer (Palo Alto, CA). All anaerobic work was performed in a Labconco inert box that was maintained at 4°C (Kansas City, Missouri).  
*wtPheH Fe<sup>2+</sup>-NO*

Recombinant rat wtPheH was over-expressed in *E. coli* BL21(DE3) cells and was purified using a variation of the hydrophobic affinity method<sup>39</sup>, as previously described.<sup>44</sup> The specific activities of wtPheH ranged between 6-7 units/mg (units = micromoles of tyrosine formed/min) with active iron content between 0.7-0.9 Fe/subunit. All protein manipulations required for the preparation of the samples were performed in an inert atmosphere box at 4°C. Approximately 35 mg of protein was used for one sample preparation. The following is the general procedure for wtPheH sample preparation.

All enzyme manipulations and NO formation were prepared in buffer (50 mM MOPS, 300 mM KCl, pH 7.2 at 4 °C) unless otherwise noted. In order to precisely quantitate the concentration of NO produced in our buffer solutions, a Clark-type NO electrode was developed using a method adapted from Stetter *et.al.*<sup>45</sup> A commercially available Clark-type electrode, ISO-NOP (World Precision Instruments, Sarasota FL), was connected to a potentiostat (Bioanalytical Systems Inc., IN) located in an inert atmosphere box. The poise voltage was set to 865 mV for NO detection.<sup>46</sup> The resulting current is proportional to the concentration of NO in solution. The electrode was calibrated daily with fresh solutions of sodium nitrite and potassium iodide (resulting in the formation of 0.025-2.5 mM NO) according to the method suggested by the

manufacturers. The calibration factor  $\mu\text{A}/\mu\text{M}$  was determined with a linear fit program.

NO saturated buffer solutions were prepared by dissolving DEA/NONOate in 10 mL of buffer (50 mM MOPS, 300 mM KCl, pH 7.2 at 4 °C) to a final 2-2.5 mM concentration. The solution was placed in a 10 mL Wheaton vial with a butyl-rubber stopper, crimped with an aluminum seal and left to incubate for one hour with frequent stirring. This sample volume was used to minimize the amount of void volume present between the top of the solution and the bottom of the stopper of the vial. After one hour incubation, the NO concentration reached approximately 2.5-2.7 mM, determined with Clark-type NO-electrode. The maximum saturation of NO at 4°C is reported as 3.2 mM.<sup>46</sup> Once the buffer was saturated with NO, it was then added to wtPheH sample (approximately 0.1 mM), which was reduced with 0.5 equivalents of 6-MPH<sub>4</sub> prior to the addition of NO solution. After 5 minutes of incubation in a vial sealed under N<sub>2</sub> atmosphere, the resulting intense yellow colored solution (Fe<sup>2+</sup>PheH-NO) was transferred to Centricon (30K) microconcentrators (Millipore) and concentrated to a final concentration of 1.5- 2 mM Fe/subunit. Approximately 200  $\mu\text{L}$  of the reaction mixture was quickly transferred to a quartz EPR tube (4 mm OD, 707-SQ-250M, Wilmad, Buena, NJ) using a glass pipette and immediately frozen in liquid N<sub>2</sub>.

If the enzyme needed to be manipulated with protiated or deuterated substrate and/or cofactor, final concentration of 10 – 15 mM of the corresponding chemical (*i.e* L-Phe, para-<sup>2</sup>H-L-Phe, per-<sup>2</sup>H-L-Phe, 5-deaza-6MPH<sub>4</sub>, <sup>2</sup>H-5-deaza-6MPH<sub>4</sub>) was added to the buffer solutions (50 mM MOPS, 300 mM KCl, pH 7.2 at 4 °C) prior to sample preparation. Additionally, in order to achieve the activated “R” state, samples were

incubated at 25 °C for 10 minutes when necessary.

### *Δ1-117PheH*

Recombinant rat  $\Delta 1-117\text{PheH}$  was over-expressed in *E.coli* BL21(DE3) cells, similar to wtPheH, except that no iron was present during cell growth resulting in expression of apo-enzyme. Apo-1-117PheH was purified using methods reported earlier<sup>47</sup> with the following adaptations. The enzyme was precipitated with ammonium sulfate (fractions between 25% - 45% saturation) and purified by anion exchange chromatography followed by size exclusion chromatography. Size exclusion chromatography performed at 0.25 mM subunit, confirm  $\Delta 1-117\text{PheH}$  elutes at a position consistent with the expected tetrameric state of the enzyme that contains the C-terminal domain known to facilitate the oligomeric state (apparent molecular mass, 154 kDa). The enzyme was concentrated back to 1 mM (40-50 mg/ml), snap-frozen in liquid nitrogen, and transferred to an inert atmosphere box for reconstitution with  $\text{Fe}^{2+}$ . All anaerobic solutions were thoroughly degassed by three freeze-pump-thaw cycles on a vacuum line utilizing  $\text{N}_2$  as the inert atmosphere. Protein samples were diluted to 0.05 mM using deoxygenated buffer (50 mM MOPS, 0.3 M KCl, pH 7.2). Ferrous ammonium sulfate (10 mM stock dissolved in 5 mM HCl) was added to a final concentration of 0.9:1  $\text{Fe}^{2+}$ :enzyme and incubated for 15 minutes for reconstitution. Reconstituted  $\text{Fe}^{2+}\Delta 1-117\text{PheH}$  was transferred to Centricon (30K) microconcentrators (Millipore) in  $\text{N}_2$  atmosphere and concentrated to a final concentration of 1.5 - 2 mM Fe/subunit. All protein manipulations required for the sample preparation were identical to the wtPheH sample preparations, that are discussed above, except that the addition of 6-MPH<sub>4</sub> was not necessary in order to reduce the

enzyme, since it was reconstituted in the ferrous oxidation state. The specific activities of the truncated enzyme used for kinetic analysis ranged between 10-14 units/mg with 0.7-0.9 Fe/subunit.

### 1.7.3 CW-EPR

CW-EPR spectra were recorded on a Bruker ESP300E X-band EPR spectrometer equipped with a TE<sub>102</sub> cavity and an Oxford Instruments ESR-900 liquid helium cryostat with a model ITC-502 temperature controller. CW-EPR measurements were made with the following conditions: sample temperature, 4.0 K; microwave frequency, 9.46 GHz; microwave power, 1 mW; magnetic field modulation frequency, 100 kHz; field modulation amplitude, 5 G; conversion time, 163 ms. CW-EPR data were analyzed using the X-SOPHE program available from Bruker Biospin Corporation.

### 1.8 THEORY

The complex formed between Fe(II) and NO produces a characteristic EPR spectrum with principle g values of  $g = 2$  and  $g = 4$ . This spectrum can be interpreted as a  $S = 3/2$  spin state and can be represented by the Hamiltonian:

$$\hat{H} = \hat{S} \cdot \mathbf{D} \cdot \hat{S} + g_0 \beta_e H \cdot \hat{S} \quad [1.1]$$

The first term in the Hamiltonian,  $\mathbf{D}$ , is the term that represents interaction between the electron dipoles of the unpaired electrons, referred to as the zero field interaction. The interaction matrix  $\mathbf{D}$ , is a symmetric and traceless tensor, and in its principle axis can be described by two parameters,  $D$  the magnitude of the interaction and  $E/D$  the shift away

from axial symmetry which can range from 0 to 1/3. At zero magnetic field the electron spin states are degenerate pairs or Kramers doublets, for an  $S = 3/2$  system there are two doublets,  $\pm 1/2$  and  $\pm 3/2$ , when  $D$  is non zero the degeneracy between these doublets is lost and the spin states are separated by  $|D|$ . Fe-NO complexes have a  $|D|$  that is about  $10 \text{ cm}^{-1}$ , our operating frequency at x-band is about  $0.3 \text{ cm}^{-1}$ , this is much too small to excite inter-kramers(between  $\pm 1/2$  and  $\pm 3/2$ ) doublet transitions and only intra-kramers(in the  $\pm 1/2$  and  $\pm 3/2$  manifolds) transitions should be observed.

The second term in the Hamiltonian is the electron Zeeman interaction, this term only appears when the magnetic field is turned on and represents a field dependent splitting within the Kramers doublets. An approximation for the electron Zeeman interaction in the Fe-NO systems is to treat the  $g$  factor as a scalar and allow the principle axis of the system to be defined by the zero field interaction and specifically the principle axis of the zero field interaction is defined by the Fe-NO bond.

One way to discuss highly anisotropic CW-EPR spectra is in terms of their effective  $g$  values. In the case of the Fe-NO  $S = 3/2$  spin system, the observed spectrum is highly anisotropic and is both a function of the electron Zeeman interaction and the zero field interaction. Based on the approximations made above for the electronic Zeeman, it is not exactly applicable to describe the spectrum in terms of its principle  $g$  values.

Instead a set of effective  $g$  values, which depend upon both the zero field interaction and electron Zeeman interaction, need to be described. After diagonalization of equation 1, the eigenvalues can be used to obtain the effective  $g$  values within the Kramers doublets.

In the limit where  $|D| \gg g\beta_e H_0$ , these effective  $g$  value are described by the following

three equations<sup>48</sup>:

$$g_{x,eff} = g_0 \left[ 1 \pm \frac{(1+3(E/D))}{\sqrt{1+3(E/D)^2}} \right] \quad [1.2a]$$

$$g_{y,eff} = g_0 \left[ 1 \pm \frac{(1-3(E/D))}{\sqrt{1+3(E/D)^2}} \right] \quad [1.2b]$$

$$g_{z,eff} = g_0 \left[ 1 \pm \frac{2}{\sqrt{1+3(E/D)^2}} \right] \quad [1.2c]$$

Using these equations, the three principle features of the EPR spectrum can be discussed in terms of the rhombicity of the zero field interaction. The magnitude of the zero field interaction  $|D|$ , in the limit where  $|D| \gg g\beta_e H_0$  has no influence on the EPR features and the rhombicity,  $E/D$ , only has an appreciable effect on  $g_x$  and  $g_y$  serving to split the two features.

## 1.9 RESULTS

To study the effects of substrate and co-substrate binding on the electronic structure of Fe center in TyrH and PheH various derivatives treated with NO were examined. Four derivatives of TyrH were examined: TyrH treated with 6-methyltetrahydropterin, TyrH[6MPH<sub>4</sub>], TyrH treated with L-tyrosine, TyrH[tyr], TyrH treated with L-tyrosine and 6-methyltetrahydropterin, TyrH[tyr,6MPH<sub>4</sub>] and the TyrH mutant E332A treated with L-tyrosine and 6-methyltetrahydropterin, E332A[tyr,6MPH<sub>4</sub>]. Four derivatives of PheH were examined: PheH, PheH[ ], PheH treated with 5-deazapterin, PheH[5d], PheH treated with L-phenylalanine, PheH[Phe], and PheH treated with L-phenylalanine and 5-deazapterin, PheH[Phe, 5d]. In addition to the full length

PheH, three derivatives of a truncated variant were examined:  $\Delta 1$ -117PheH treated with 5-deazapterin,  $\Delta$ PheH[5d],  $\Delta 1$ -117PheH treated with L-phenylalanine,  $\Delta$ PheH[Phe], and

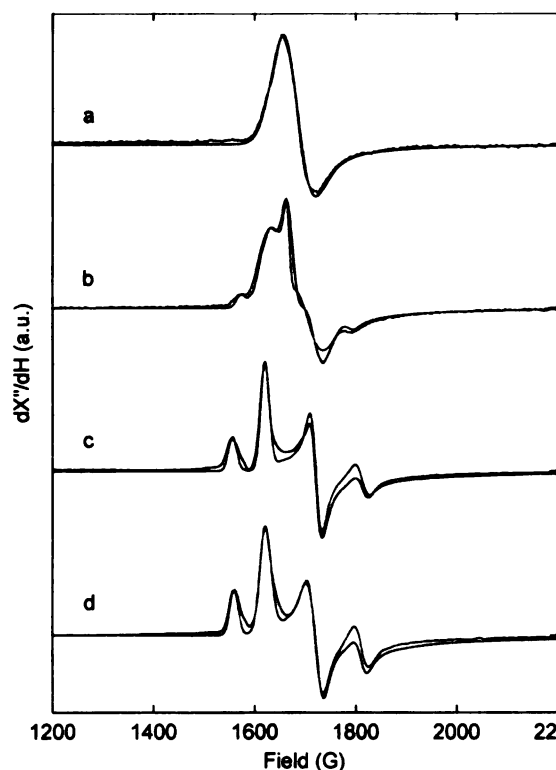


Figure 1.4: CW-EPR spectra of (a) TyrH[6MPH<sub>4</sub>], (b) TyrH[tyr], (c) TyrH[tyr,6MPH<sub>4</sub>], (d) E332A[tyr,6MPH<sub>4</sub>] shown in black with corresponding simulations shown in red.

$\Delta 1$ -117PheH treated with L- phenylalanine and 5-deazapterin,  $\Delta$ PheH[Phe, 5d].

Shown in figure 1.4 are the CW-EPR spectra of the 4 derivatives of TyrH; (a) TyrH[6MPH<sub>4</sub>], (b) TyrH[tyr], (c) TyrH[tyr,6MPH<sub>4</sub>], (d) E332A[tyr,6MPH<sub>4</sub>], experiment is shown in black and the corresponding simulation is shown in red. The CW-EPR spectrum of TyrH[6MPH<sub>4</sub>]

(Figure 1.4a) is characteristic of an axial S = 3/2 species yielding spectral features at effective g values of  $g_{\perp} = 4$  and  $g_{\parallel} = 2$ . The red trace of Figure 1.4a is a simulation of the spectrum performed using spin Hamiltonian (1.1), with  $|D| = 10 \text{ cm}^{-1}$  and  $E/D = 0$ . The

line shape in the  $g = 4$  region was described with two parameters, an intrinsic Gaussian line shape with a FWHM of  $1 \times 10^{-3} \text{ cm}^{-1}$  that was applied uniformly across the EPR spectrum, and an E/D strain,  $\sigma_{E/D} = 0.0130$ , that was adjusted to account for the line shape at  $g = 4$ .

Figure 1.4b shows the EPR spectrum of TyrH[tyr]. This was modeled as a mixture

of two components in our simulation (red trace). The major component, 91% of the observed signal, was simulated with  $g_0 = 2.028$  and  $E/D = 0.0175$ . The inflection-like characteristic of the line shape at  $g = 4$  required an E/D strain broadening of  $\sigma_{E/D} = 0.0107$ . The minor component, 9% of the observed signal, is more rhombic with  $g_0 = 2.023$ ,  $E/D = 0.0425$ , and  $\sigma_{E/D} = 0.0040$ . Simulations of the major and minor components were added with the appropriate weightings to obtain the simulation.

The CW-EPR spectrum of TyrH treated with reduced pterin and L-tyrosine, TyrH[6MPH<sub>4</sub>,tyr] (Figure 1.4c), is composed of two slightly rhombic species. The more axial of the two accounts for 76% of the observed signal and was simulated with  $g_0 = 2.024$ ,  $E/D = 0.0204$  and  $\sigma_{E/D} = 0.0035$ . The second, slightly more rhombic component, was simulated with  $g_0 = 2.02$ ,  $E/D = 0.051$ , and  $\sigma_{E/D} = 0.0040$ . As in Figure 1.4b, simulations of the major and minor components were added with the appropriate weightings to obtain the simulation shown as the red trace in Figure 1.4c.

The CW-EPR spectrum of the TyrH mutant E332A treated with reduced pterin and L-tyrosine, E332A[6MPH<sub>4</sub>,tyr], is composed of two slightly rhombic species, as shown in Figure 1.4d. The more axial of the two accounts for 76% of the observed signal and was simulated with  $g_0 = 2.024$ ,  $E/D = 0.0201$  and  $\sigma_{E/D} = 0.005$ . The second, slightly more rhombic component, was simulated with  $g_0 = 2.019$ ,  $E/D = 0.05$ , and  $\sigma_{E/D} = 0.0040$ . As in Figure 1.4b, simulations of the major and minor components were added with the appropriate weightings to obtain the simulation shown as the red trace in Figure 1.4d.

Shown in figure 1.5 are the CW-EPR spectra of the 4 derivatives of PheH; (a)

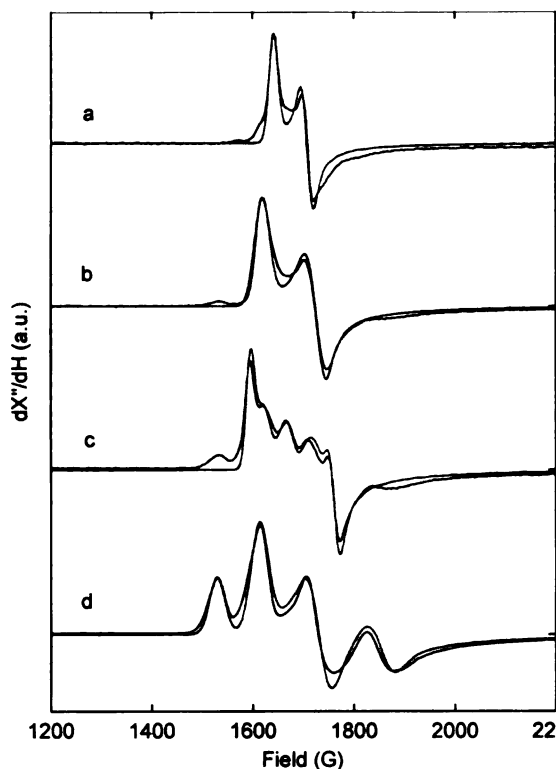


Figure 1.5: CW-EPR spectra of (a) PheH[ ], (b) PheH[5d], (c) PheH[Phe], (d) PheH[Phe, 5d] shown in black with corresponding simulations shown in red.

PheH[ ], (b) PheH[5d], (c) PheH[Phe], (d) PheH[Phe, 5d], experiment is shown in black and the corresponding simulation is shown in red. The CW-EPR spectrum of PheH[ ] (Figure 1.5a) shows the characteristic nearly axial spectrum of a  $S = 3/2$  species. The red trace of Figure 1.5a is a simulation of the spectrum done using the above spin Hamiltonian, with  $|D| = 10 \text{ cm}^{-1}$ ,  $g_0 = 2.0175$  and  $E/D = 0.0135$ . The line

shape in the  $g = 4$  region was described with two parameters, an intrinsic Gaussian line shape with a FWHM of  $1.5 \times 10^{-3} \text{ cm}^{-1}$  that was applied uniformly across the EPR

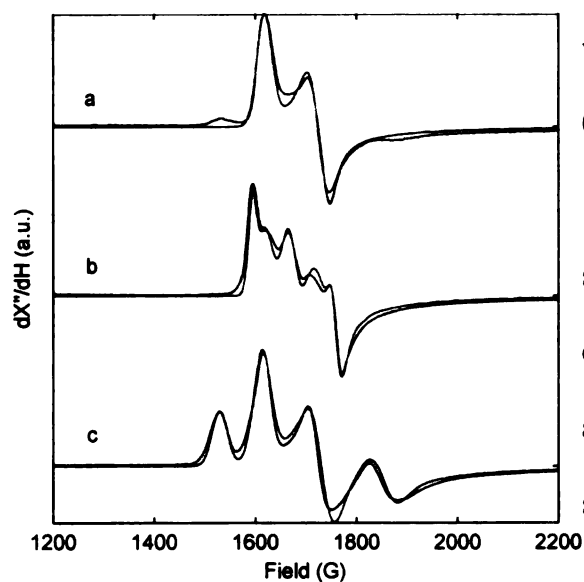
spectrum, and an E/D strain,  $\sigma_{E/D} = 0.0030$ , that was adjusted to account for the line shape at  $g = 4$ .

Figure 1.5b shows the EPR spectrum of PheH[5d]. The spectrum was simulated with a single component with  $g_0 = 2.023$  and  $E/D = 0.0220$ . The line shape at  $g = 4$  required an intrinsic Gaussian line shape with a FWHM of  $2.0 \times 10^{-3} \text{ cm}^{-1}$  that was applied uniformly across the EPR spectrum, and an E/D strain,  $\sigma_{E/D} = 0.0060$ .

The CW-EPR spectrum of PheH[Phe] (Figure 1.5c), is composed of three slightly rhombic species. The most rhombic of the three accounts for 54% of the observed signal

and was simulated with  $g_0 = 2.019$ ,  $E/D = 0.0330$ , Gaussian line shape  $1.5 \times 10^{-3} \text{ cm}^{-1}$  and  $\sigma_{E/D} = 0.003$ . The second, slightly axial more component which accounts for 29% of the signal, was simulated with  $g_0 = 2.019$ ,  $E/D = 0.0225$ , Gaussian line shape  $1.5 \times 10^{-3} \text{ cm}^{-1}$  and  $\sigma_{E/D} = 0.0060$ . The last, axial component, which accounts for 16% of the signal, was simulated with  $g_0 = 2.019$ ,  $E/D = 0.000$ , Gaussian line shape  $1.5 \times 10^{-3} \text{ cm}^{-1}$  and  $\sigma_{E/D} = 0.0060$ . As in Figure 1.4b, simulations of the major and minor components were added with the appropriate weightings to obtain the simulation shown as the red trace in Figure 1.5c.

The CW-EPR spectrum of the PheH[Phe, 5d], is composed of two slightly rhombic species, as shown in Figure 1.5d. The more axial of the two accounts for 66% of the observed signal and was simulated with  $g_0 = 2.0225$ ,  $E/D = 0.0245$ , Gaussian line shape  $1.5 \times 10^{-3} \text{ cm}^{-1}$  and  $\sigma_{E/D} = 0.008$ . The second, slightly more rhombic component,



was simulated with  $g_0 = 2.021$ ,  $E/D = 0.0645$ , Gaussian line shape  $2.0 \times 10^{-3} \text{ cm}^{-1}$ , and  $\sigma_{E/D} = 0.0075$ . As in Figure 1.4b, simulations of the major and minor components were added with the appropriate weightings to obtain the simulation shown as the red trace in Figure 1.5d.

Figure 1.6: CW-EPR spectra of (a)  $\Delta$ PheH[5d], (b)  $\Delta$ PheH[Phe], (c)  $\Delta$ PheH[Phe, 5d] shown in black with corresponding simulations shown in red.

Lastly shown in figure 1.6 are the CW-EPR spectra of the 3 derivatives of  $\Delta$ 1-

117 truncated PheH; (a)  $\Delta$ PheH[5d], (b)  $\Delta$ PheH[Phe], (c)  $\Delta$ PheH[Phe, 5d], experiment is shown in black and the corresponding simulation is shown in red. The parameters used to simulate the truncated PheH spectra were identical to those used for wt enzyme.

### 1.10 SIMULATION NOTES

The parameters used to simulate the CW-EPR spectra of TyrH are shown in table 1.1 and for PheH in table 1.2. These parameters were determined through visual comparison of the experimental data and simulation.

Table 1.1: Simulation Parameters for TyrH

	%	E/D	$\sigma_{E/D}$	$g_0$	Line-width
TyrH[6MPH <sub>4</sub> ]	100	0.0000	0.0130	2	15
TyrH[tyr]	91	0.0175	0.0107	2.028	15
	9	0.0425	0.0040	2.023	15
TyrH[6MPH <sub>4</sub> ,tyr]	76	0.0204	0.0035	2.024	15
	24	0.0510	0.0040	2.02	15
E332A[6MPH <sub>4</sub> , tyr]	76	0.0201	0.0050	2.024	15
	24	0.0500	0.0040	2.019	15

Table 1.2: Simulation Parameters for PheH

	%	E/D	$\sigma_{E/D}$	$g_0$	Line-width
PheH[ ]	100	0.0135	0.0030	2.0175	15
PheH[5-deazapterin]	100	0.0220	0.0060	2.0230	20
PheH[L-phe]	54	0.0330	0.0030	2.0190	15
	29	0.0225	0.0060	2.0190	15
	16	0.0000	0.0060	2.0190	15
PheH[L-phe,5-deazapterin]	66	0.0245	0.0080	2.0225	15
	34	0.0645	0.0075	2.0210	20

The simulations were performed in the Bruker simulation program Xsophe using the Hamiltonian in equation 1.1. Based on this Hamiltonian there are five parameters to fit, the zero field parameters,  $D$  and  $E/D$  and the principle  $g$  values,  $g_x$ ,  $g_y$ ,  $g_z$ . In addition to the Hamiltonian parameters, there were two line-width parameters, the intrinsic line-width and the strain in  $D$  and  $E/D$ , that need to be considered.

In the limit, where  $|D| \gg g\beta_e H$ , it can be seen from equation 2a-c that the EPR spectrum for a  $S = 3/2$  spin system can be characterized in terms of two principle  $g$  features, the feature at  $g = 2$  which corresponds to  $g_z$  and the feature at  $g = 4$  which corresponds to  $g_x$  and  $g_y$  or  $g_{\perp}$ . When considering the features of the Fe-NO spectrum,  $g_z$  was largely disregarded for several reasons. The samples were prepared with NO and in some cases there was residual NO left in solution. The NO radical produces an EPR signal which overlaps with the  $g_z$  feature obscuring any information we could gain in that region. While this could be easily remedied through more careful sample preparation, the second reason further supports neglecting  $g_z$ . In equation 2c, the position of the  $g_z$  feature only has a minor dependence on  $E/D$ . This is further supported by observations from sample simulations, changes in  $E/D$  have a negligible effect on the position of the  $g_z$  feature. Based on these observations the  $g_z$  feature was considered unimportant to accurately fit and instead the simulation efforts were focused on the  $g_{\perp}$  or  $g = 4$  region.

In the simulation program, it has also been observed that when  $|D| < 6 \text{ cm}^{-1}$ , the position of  $g_{\perp}$  is raised to a higher field. This is a result of the higher order terms which manifest themselves upon diagonalization of equation 1.1 that don't entirely cancel. In theory the value of  $|D|$  could be less than  $6 \text{ cm}^{-1}$  however due to our operating frequency,

$\sim 0.3 \text{ cm}^{-1}$ , we can't directly measure the transitions necessary assign a value to  $|D|$ , so we have arbitrarily set the value at  $10 \text{ cm}^{-1}$ . This value of  $10 \text{ cm}^{-1}$  was one utilized in previous studies<sup>32b 49</sup> and is large enough so that  $|D|$  has no effect on the simulation.

It was found that often the  $g_{\perp}$  feature produced in the simulations did not properly line up with experiment, when the exact operating frequency and field was used. In order to adjust the position of  $g_{\perp}$  small adjustments to the value of  $g_0$  were necessary. This overall is an approximation, as is the inclusion of  $g_0$  in equations 1.2a-c. A more accurate interpretation would include three distinct  $g$  value, however, due to the resolution of the experiment at x-band, much like with  $|D|$ , its impossible to accurately determine these values.

The Hamiltonian parameter which has the most substantial influence on the observed spectrum is the rhombicity of the zero field interaction,  $E/D$ . As can be seen in equation 1.2a-c and using the above approximation for  $g_0$ , the only parameter which separates  $g_x$  and  $g_y$  is  $E/D$ . This parameter can have a maximum value of  $1/3$  however for those systems we've examined this value rarely exceeds  $1/20$ . This result exemplifies the axial nature of these Fe-NO complexes.

After the Hamiltonian parameters are fit it is necessary to consider the line-shape to overall produce a satisfying simulation. The line-shape in this system can be influenced by two parameters intrinsic line-width and the zero field strain. The intrinsic line-width represents a Gaussian broadening which is applied uniformly to the spectrum, this broadening is difficult to fully interpret and directly relate back to a physical quantity, such as  $T_2$  or  $T_2^*$ . When deciding the extent of the intrinsic line broadening, this

parameter was adjusted in a rough fashion with particular attention paid to the slope between the maximum near  $g_y$  and the minimum near  $g_y$ .

The line-shape characteristics are also influenced by the zero field strain, which includes two different effects, strain in  $|D|$  and the strain in  $E/D$ . Based on the magnitude of  $|D|$  that we've seen in the Fe-NO complexes, its reasonable to assume that only strain in  $|D|$  that is of the magnitude of  $|D|$  will have any effect on the spectrum. The second parameter, the  $E/D$  strain, represents an uncertainty in  $E/D$  or in a physical sense, a distribution of structures which contribute to a rhombicity in the zero field interaction.

## 1.11 DISCUSSION

From the presence of the characteristic  $g=4/g=2$  CW-EPR spectrum seen in figures 1.3-1.5, we've shown that we were able to produce the  $S = 3/2$  Fe-NO complex with both TyrH and PheH in multiple different states. It can be seen from both the spectra and the parameters seen in table 1.1, when these enzymes are treated with substrate and co-substrate there is a change observed in the rhombicity,  $E/D$ , and the strain associated with  $E/D$ .

The CW-EPR spectra of TyrH were acquired on wt enzyme in various states, with and without substrate and co-substrate This study of TyrH did not include the empty, unloaded enzyme, so there is no "blank" to compare the effect that substrate might have on the EPR spectrum. However, according to the crystal structures recorded for TyrH<sup>20</sup>, the pterin co-factor is not shown to directly coordinate the iron and based on this we could make the assumption that the active site structure of TyrH[6MPH<sub>4</sub>] is close to that of the empty state. While this assumption is not perfect it does provide us a basis with

which to compare the other TyrH spectra. The CW-EPR spectrum of TyrH[6MPH<sub>4</sub>] shows a featureless axial line-shape, the result of having an E/D = 0, this line-shape seems to suggest that the pterin binding has little influence on the electronic structure of the Fe-NO center and does little to perturb it away from axial. In addition, it has an E/D strain greater than any other sample examined, this could be a result of structural dispersion at the active site.

A comparison of the spectrum of TyrH[6MPH<sub>4</sub>] to the spectrum of TyrH[tyr] shows considerable differences between the two. TyrH[tyr] is composed of a mixture of two species, the major component, which composes over 90% of the CW-EPR spectrum, shows a significant increase of E/D compared to TyrH[6MPH<sub>4</sub>] this is accompanied by a 20% decrease in the E/D strain. The changes observed indicate that the substrate tyr has a modest effect on the electronic structure of the TyrH Fe-NO center in comparison to the co-substrate. This change in electronic structure is most likely a result of a structural change due to the presence of tyr near the active site either displacing a Fe ligand or having an influence on the first shell coordination. The decrease in strain suggests that there is more local order with tyr present. The minor component of the spectra shows an increase in rhombicity more than double the one seen in the major component and a much larger decrease in strain.

When TryH is treated with both the substrate and the co-substrate, the CW-EPR spectrum shows a mixture of two non-axial species at  $g = 4$ . The majority species shows an increase in rhombicity over the majority species seen in the spectrum of TyrH[tyr] and a decrease of about 60% in E/D strain. These changes can be interpreted in two ways: the

addition of the tyr affects a structural change which shifts the position the pterin further increasing the rhombicity of the electronic structure of the Fe-NO; or the addition of the pterin shifts the position of the tyr affecting this change. The decrease in strain does suggest that the quaternary complex has a significantly more ordered structure than the ternary complexes. The minor species also shows an increase in E/D in comparison to the minor species TyrH[tyr] and an increase in amplitude.

The TyrH mutant E332A was also examined, this mutant does not hydroxylate tyr but does produce an oxidized pterin species, possibly 4a-hydroperoxypterin.<sup>35 26d</sup> The CW-EPR spectrum of E332A[6MPH<sub>4</sub>, tyr] shows a mixture of two species and splitting much like that seen in wild type TyrH[6MPH<sub>4</sub>, tyr]. Both the major and minor component have an E/D parameter within about 5% of the wild type enzyme, this result seems to indicate that the electronic structure of the mutant and the effects the substrates have on the Fe-NO center are similar to that seen in the wt enzyme.

Overall the CW-EPR spectra acquired on TyrH show differences in the electronic structure of the Fe-NO active site when different substrates are added and differences between the ternary and quaternary complexes. In addition to the natural substrates, selectively deuterated substrates were examined, however no changes were observed. If the labeled position had a significant interaction with the Fe-NO center a change in line-width would have been observed, none was seen so the interaction with the labeled position was too weak to resolve. The quaternary complex in D<sub>2</sub>O was also examined and again no influence from isotopic labeling was observed within the resolution of the experiment.

The CW-EPR spectra of PheH shows very similar changes with respect to substrate binding as was observed in TyrH with a key difference; the major component of the spectra in the PheH samples all show a relative increase in E/D in comparison to the analogous sample of TyrH. Differences between the two enzymes are expected, while their active site structures are similar, they do catalyze different reactions and studies have suggested that they proceed through different kinetic mechanisms.<sup>13</sup>

In the PheH system a “blank”, which consists of the empty state enzyme treated with NO, was examined. The spectrum for this sample shows a splitting at  $g_{\perp}$ , the value of  $E/D \neq 0$ , this means that the electronic structure of the Fe-NO in PheH[ ] is influenced by the protein framework and is restricted from obtaining a purely axial environment like the one seen in TyrH[6MPH<sub>4</sub>]. This difference is most likely an indication of the structural differences between the two enzyme and the broader regulatory differences.<sup>12</sup>

The addition of pterin to PheH[ ] increases the rhombicity of the Fe-NO zero field interaction by 60% or an increase of E/D of 0.009 and broadens the line, we see an increase in both the strain and the intrinsic line-width. These changes indicate that the pterin affects a minor structural change within the enzyme. The increase in line-width suggests that there may be a larger distribution of structures with pterin present and the increase in rhombicity confirms that pterin has a affect on the electronic structure of the Fe-NO.

The spectrum of PheH[ ] treated with phe shows a mixture of three species all of which have a rhombicity different than the one seen in PheH[ ] suggesting that phe has an influence on the electronic structure of Fe-NO. The major species shows an increase in

rhombicity and a decrease in strain over both PheH[ ] and PheH[5d], these changes indicate that in this species the presence of phe has a greater effect on the local structure at the iron than the addition of pterin. There is a decrease in the E/D strain compared to PheH[5d] which means that with phe in the active site there is a slightly less disperse interaction. The intermediate component of PheH[phe] has a set of parameters similar to those obtained for the major component PheH[5d], from this similarity it could be assumed that the phe is binding in a similar fashion and causing the same type of interaction as the pterin. This is merely an assumption and without any higher resolution experiments can't actually be determined. In addition to these two species there is a third more minor component that was largely obscured by the other two. A simulation was provided for this component however there is relative uncertainty in the accuracy of that fit.

Overall the simulations provided for PheH[phe] are not entirely satisfying. While it's true that the simulations do accurately account for the spectral features, the presence of three distinct species is difficult to accept. In part this idea comes from the overlap of the different species seen in the spectrum, a feature that was simulated as two distinct species could have in fact been a single extremely strain broadened (large  $\sigma_{E/D}$ ) species. Our ability to distinguish between these two different possibilities is limited by the resolution of the experiment, so while three species may not be satisfying, the fits provided are the best available.

When PheH[ ] is treated with both phe and 5d, it displays a mixture of two slightly rhombic features at  $g = 4$ . The major component is 25% less rhombic and has more than double the strain in E/D than the major, most rhombic component of

PheH[phe]. The minor component has a rhombicity greater than any seen in the CW-EPR spectra collected in this work, with  $E/D = 0.0645$ . Both of these changes are similar to those observed in TyrH, and can be interpreted in a similar fashion. The presence of a single substrate perturbs the electronic structure away from the initial state and the addition of a second substrate further perturbs the Fe-NO active site. These changes in electronic structure are most likely tied to a physical structural change near the Fe-NO however the zero-field parameters are not very well understood and it is difficult to draw any direct structural correlations.

PheH which has had residue 1-107 truncated was also examined to determine if there were any significant differences in the electronic structure compared to full length enzyme. To within the resolution of the experiment the truncated variety of the enzyme shows no significant differences compared to full length enzyme. This similarity suggests that the active site structure of the full length and truncated enzyme are the same, this however is just an assumption based on the zero field splitting.

Several of the CW-EPR spectra we've collected are composed of mixtures species with different values of  $E/D$ . A multi-component CW-EPR spectra has been observed in both the ferric and ferrous nitrosyl forms of PheH and soybean lipoxygenase.<sup>50 44 33 51 52</sup> Based on the observation of a mixture in both ferrous and ferric PheH, it is reasonable to assume that the mixtures we've observed are independent of the orientation of the NO bond but instead reflects differences in the coordination environment of the Fe-NO. The Fe center in these enzymes is known to be coordinated by 2 histidines and a glutamate; the other sites include solvent and NO. Its possible that the two species observed in the

CW-EPR are the result of freezing in different conformers of bound water or of capturing a mixture, either mono or bidentate, in the ligation of the glutamate side chain. An alternate explanation was suggested from work performed on a series of models. From a combined study of both the EPR spectra and the crystal structures, a relationship between the angle of the Fe-N-O bond and the value of E/D was observed.<sup>53</sup> With a decrease in the Fe-N-O bond angle from 178° → 172° → 160°, the value of E/D was observed to increase from 0.062 → 0.072 → 0.090.<sup>53</sup> This change in E/D is of a similar magnitude (~0.03) to the changes that we've observed upon substrate additions to TyrH and PheH; suggesting that these additions might simply be influencing the coordination sphere near the Fe and in turn having an effect the Fe-N-O bond angle. In addition, the mixtures that we've observed could be a result of freezing in two or more different Fe-N-O bond angles.

## **1.12 CONCLUSIONS**

We've shown that we have been able to produce an EPR active species from NO treated ferrous enzyme which shows changes in the electronic structure in response to substrate additions. The CW-EPR spectra of TyrH and PheH show similarities but are inherently different. These results while interesting do not provide structural data about the enzymes and further work using more advanced, higher resolution EPR techniques will have to be performed.

### 1.13 REFERENCES

1. Kovaleva, E. G.; Lipscomb, J. D., Versatility of Biological Non-Heme Fe(II) Centers in Oxygen Activation Reactions. *Nat Chem Biol* **2008**, *4* (3), 186-193.
2. Abu-Omar, M. M.; Loaiza, A.; Hontzeas, N., Reaction Mechanisms of Mononuclear Non-Heme Iron Oxygenases. *Chem Rev* **2005**, *105* (6), 2227-2252.
3. Sono, M.; Roach, M. P.; Coulter, E. D.; Dawson, J. H., Heme-Containing Oxygenases. *Chem Rev* **1996**, *96* (7), 2841-2887.
4. Holm, R. H.; Kennepohl, P.; Solomon, E. I., Structural and Functional Aspects of Metal Sites in Biology. *Chem Rev* **1996**, *96* (7), 2239-2314.
5. Decker, A.; Solomon, E. I., Dioxygen Activation by Copper, Heme and Non-Heme Iron Enzymes: Comparison of Electronic Structures and Reactivities. *Curr Opin Chem Biol* **2005**, *9* (2), 152-163.
6. Fitzpatrick, P. F., Mechanism of Aromatic Amino Acid Hydroxylation. *Biochemistry-Us* **2003**, *42* (48), 14083-14091.
7. Hegg, E. L.; Que, L., The 2-His-1-Carboxylate Facial Triad - an Emerging Structural Motif in Mononuclear Non-Heme Iron(II) Enzymes. *European Journal of Biochemistry* **1997**, *250* (3), 625-629.
8. (a) Que, L., One Motif - Many Different Reactions. *Nat Struct Biol* **2000**, *7* (3), 182-184; (b) Bruijninx, P. C. A.; van Koten, G.; Gebbink, R. J. M. K., Mononuclear Non-Heme Iron Enzymes with the 2-His-1-Carboxylate Facial Triad: Recent Developments in Enzymology and Modeling Studies. *Chem Soc Rev* **2008**, *37* (12), 2716-2744.
9. Solomon, E. I.; Decker, A.; Lehnert, N., Non-Heme Iron Enzymes: Contrasts to Heme Catalysis. *P Natl Acad Sci USA* **2003**, *100* (7), 3589-3594.
10. Solomon, E. I.; Pavel, E. G.; Loeb, K. E.; Campochiaro, C., Magnetic Circular-Dichroism Spectroscopy as a Probe of the Geometric and Electronic-Structure of Nonheme Ferrous Enzymes. *Coordin Chem Rev* **1995**, *144*, 369-460.
11. Solomon, E. I.; Brunold, T. C.; Davis, M. I.; Kemsley, J. N.; Lee, S. K.; Lehnert, N.; Neese, F.; Skulan, A. J.; Yang, Y. S.; Zhou, J., Geometric and Electronic Structure/Function Correlations in Non-Heme Iron Enzymes. *Chem Rev* **2000**, *100* (1), 235-349.
12. Kappock, T. J.; Caradonna, J. P., Pterin-Dependent Amino Acid Hydroxylases. *Chem Rev* **1996**, *96* (7), 2659-2756.
13. Fitzpatrick, P. F., Tetrahydropterin-Dependent Amino Acid Hydroxylases. *Annu*

*Rev Biochem* **1999**, *68*, 355-381.

14. Lazarus, R. A.; Dietrich, R. F.; Wallick, D. E.; Benkovic, S. J., On the Mechanism of Action of Phenylalanine-Hydroxylase. *Biochemistry-U.S.* **1981**, *20* (24), 6834-6841.
15. (a) Dix, T. A.; Kuhn, D. M.; Benkovic, S. J., Mechanism of Oxygen Activation by Tyrosine-Hydroxylase. *Biochemistry-U.S.* **1987**, *26* (12), 3354-3361; (b) Moran, G. R.; Daubner, S. C.; Fitzpatrick, P. F., Expression and Characterization of the Catalytic Core of Tryptophan Hydroxylase. *J Biol Chem* **1998**, *273* (20), 12259-12266.
16. Andersen, O. A.; Flatmark, T.; Hough, E., High Resolution Crystal Structures of the Catalytic Domain of Human Phenylalanine Hydroxylase in Its Catalytically Active Fe(II) Form and Binary Complex with Tetrahydrobiopterin. *J Mol Biol* **2001**, *314* (2), 279-91.
17. Andersen, O. A.; Flatmark, T.; Hough, E., Crystal Structure of the Ternary Complex of the Catalytic Domain of Human Phenylalanine Hydroxylase with Tetrahydrobiopterin and 3-(2-Thienyl)-L-Alanine, and Its Implications for the Mechanism of Catalysis and Substrate Activation. *J Mol Biol* **2002**, *320* (5), 1095-1108.
18. Andersen, O. A.; Stokka, A. J.; Flatmark, T.; Hough, E., 2.0 Angstrom Resolution Crystal Structures of the Ternary Complexes of Human Phenylalanine Hydroxylase Catalytic Domain with Tetrahydrobiopterin and 3-(2-Thienyl)-L-Alanine or L-Norleucine: Substrate Specificity and Molecular Motions Related to Substrate Binding. *J Mol Biol* **2003**, *333* (4), 747-757.
19. Goodwill, K. E.; Sabatier, C.; Marks, C.; Raag, R.; Fitzpatrick, P. F.; Stevens, R. C., Crystal Structure of Tyrosine Hydroxylase at 2.3 Angstrom and Its Implications for Inherited Neurodegenerative Diseases. *Nat Struct Biol* **1997**, *4* (7), 578-585.
20. Goodwill, K. E.; Sabatier, C.; Stevens, R. C., Crystal Structure of Tyrosine Hydroxylase with Bound Cofactor Analogue and Iron at 2.3 Angstrom Resolution: Self-Hydroxylation of Phe300 and the Pterin-Binding Site. *Biochemistry-U.S.* **1998**, *37* (39), 13437-13445.
21. Wang, L.; Erlandsen, H.; Haavik, J.; Knappskog, P. M.; Stevens, R. C., Three-Dimensional Structure of Human Tryptophan Hydroxylase and Its Implications for the Biosynthesis of the Neurotransmitters Serotonin and Melatonin. *Biochemistry-U.S.* **2002**, *41* (42), 12569-74.
22. Windahl, M. S.; Petersen, C. R.; Christensen, H. E. M.; Harris, P., Crystal Structure of Tryptophan Hydroxylase with Bound Amino Acid Substrate. *Biochemistry-U.S.* **2008**, *47* (46), 12087-12094.
23. Erlandsen, H.; Fusetti, F.; Martinez, A.; Hough, E.; Flatmark, T.; Stevens, R. C., Crystal Structure of the Catalytic Domain of Human Phenylalanine Hydroxylase Reveals the Structural Basis for Phenylketonuria. *Nat Struct Biol* **1997**, *4* (12), 995-1000.

24. Daubner, S. C.; McGinnis, J. T.; Gardner, M.; Kroboth, S. L.; Morris, A. R.; Fitzpatrick, P. F., A Flexible Loop in Tyrosine Hydroxylase Controls Coupling of Amino Acid Hydroxylation to Tetrahydropterin Oxidation. *J Mol Biol* **2006**, *359* (2), 299-307.
25. Sura, G. R.; Lasagna, M.; Gawandi, V.; Reinhart, G. D.; Fitzpatrick, P. F., Effects of Ligands on the Mobility of an Active-Site Loop in Tyrosine Hydroxylase as Monitored by Fluorescence Anisotropy. *Biochemistry-Us* **2006**, *45* (31), 9632-9638.
26. (a) Loeb, K. E.; Westre, T. E.; Kappock, T. J.; Mitic, N.; Glasfeld, E.; Caradonna, J. P.; Hedman, B.; Hodgson, K. O.; Solomon, E. I., Spectroscopic Characterization of the Catalytically Competent Ferrous Site of the Resting, Activated, and Substrate-Bound Forms of Phenylalanine Hydroxylase. *J Am Chem Soc* **1997**, *119* (8), 1901-1915; (b) Kemsley, J. N.; Mitic, N.; Zaleski, K. L.; Caradonna, J. P.; Solomon, E. I., Circular Dichroism and Magnetic Circular Dichroism Spectroscopy of the Catalytically Competent Ferrous Active Site of Phenylalanine Hydroxylase and Its Interaction with Pterin Cofactor. *J Am Chem Soc* **1999**, *121* (7), 1528-1536; (c) Wasinger, E. C.; Mitic, N.; Hedman, B.; Caradonna, J.; Solomon, E. I.; Hodgson, K. O., X-Ray Absorption Spectroscopic Investigation of the Resting Ferrous and Cosubstrate-Bound Active Sites of Phenylalanine Hydroxylase. *Biochemistry-Us* **2002**, *41* (20), 6211-6217; (d) Chow, M. S.; Eser, B. E.; Wilson, S. A.; Hodgson, K. O.; Hedman, B.; Fitzpatrick, P. F.; Solomon, E. I., Spectroscopy and Kinetics of Wild-Type and Mutant Tyrosine Hydroxylase: Mechanistic Insight into O-2 Activation. *J Am Chem Soc* **2009**, *131* (22), 7685-7698.
27. Eberlein, G.; Bruice, T. C.; Lazarus, R. A.; Henrie, R.; Benkovic, S. J., The Interconversion of the 5,6,7,8-Tetrahydropterin, 7,8-Dihydropterin, and Radical Forms of 6,6,7,7-Tetramethyldihydropterin - a Model for the Biopterin Center of Aromatic Amino-Acid Mixed-Function Oxidases. *J Am Chem Soc* **1984**, *106* (25), 7916-7924.
28. Ellis, H. R.; McCusker, K. P.; Fitzpatrick, P. F., Use of a Tyrosine Hydroxylase Mutant Enzyme with Reduced Metal Affinity Allows Detection of Activity with Cobalt in Place of Iron. *Arch. Biochem. Biophys.* **2002**, *408* (2), 305-307.
29. Guroff, G.; Levitt, M.; Daly, J.; Udenfrie, S., Production of Meta-Tritiotyrosine from P-Tritiophenylalanine by Phenylalanine Hydroxylase. *Biochem. Biophys. Res. Commun.* **1966**, *25* (2), 253-&.
30. Renson, J.; Daly, J.; Weissbac, H.; Witkop, B.; Udenfrie, S., Enzymatic Conversion of 5-Tritiotryptophan to 4-Tritio-5-Hydroxytryptophan. *Biochem. Biophys. Res. Commun.* **1966**, *25* (5), 504-&.
31. Rich, P. R.; Salerno, J. C.; Leigh, J. S.; Bonner, W. D., Spin 3-2 Ferrous-Nitric Oxide Derivative of an Iron-Containing Moiety Associated with Neurospora-Crassa and Higher Plant-Mitochondria. *Febs Lett* **1978**, *93* (2), 323-326.
32. (a) Hishinuma, Y.; Kaji, R.; Akimoto, H.; Nakajima, F.; Mori, T.; Kamo, T.; Arikawa, Y.; Nozawa, S., Reversible Binding of No to Fe(Ii)Edta. *Bull. Chem. Soc. Jpn.* **1979**, *52* (10), 2863-2865; (b) Arciero, D. M.; Lipscomb, J. D.; Huynh, B. H.; Kent, T.

- A.; Munck, E., Electron-Paramagnetic-Res and Mossbauer Studies of Protocatechuate 4,5-Dioxygenase - Characterization of a New Fe-2+ Environment. *J Biol Chem* **1983**, *258* (24), 4981-4991.
33. Han, A. Y.; Lee, A. Q.; Abu-Omar, M. M., Epr and Uv-Vis Studies of the Nitric Oxide Adducts of Bacterial Phenylalanine Hydroxylase: Effects of Cofactor and Substrate on the Iron Environment. *Inorg Chem* **2006**, *45* (10), 4277-4283.
34. Fitzpatrick, P. F., The Ph-Dependence of Binding of Inhibitors to Bovine Adrenal Tyrosine-Hydroxylase. *J Biol Chem* **1988**, *263* (31), 16058-16062.
35. Frantom, P. A.; Seravalli, J.; Ragsdale, S. W.; Fitzpatrick, P. F., Reduction and Oxidation of the Active Site Iron in Tyrosine Hydroxylase: Kinetics and Specificity. *Biochemistry-Us* **2006**, *45* (7), 2372-2379.
36. Daubner, S. C.; Fitzpatrick, P. F., Site-Directed Mutants of Charged Residues in the Active Site of Tyrosine Hydroxylase. *Biochemistry-Us* **1999**, *38* (14), 4448-4454.
37. Ramsey, A. J.; Hillas, P. J.; Fitzpatrick, P. F., Characterization of the Active Site Iron in Tyrosine Hydroxylase - Redox States of the Iron. *J Biol Chem* **1996**, *271* (40), 24395-24400.
38. Keefer, L. K.; Nims, R. W.; Davies, K. M.; Wink, D. A., "Nonoates" (1-Substituted Diazen-1-ium-1,2-Diolates) as Nitric Oxide Donors: Convenient Nitric Oxide Dosage Forms. *Method Enzymol* **1996**, *268*, 281-293.
39. Shiman, R.; Gray, D. W.; Pater, A., Simple Purification of Phenylalanine-Hydroxylase by Substrate-Induced Hydrophobic Chromatography. *J Biol Chem* **1979**, *254* (22), 1300-1306.
40. Storm, C. B.; Shiman, R.; Kaufman, S., Preparation of 6-Substituted Pterins Via Isay Reaction. *J. Org. Chem.* **1971**, *36* (25), 3925-&.
41. Stark, E.; Breitmai.E, 5-Desazapteridines - Synthesis and Nmr-Spectroscopy. *Tetrahedron* **1973**, *29* (14), 2209-2217.
42. Shiman, R.; Akino, M.; Kaufman, S., Solubilization and Partial Purification of Tyrosine Hydroxylase from Bovine Adrenal Medulla. *J Biol Chem* **1971**, *246* (5), 1330-&.
43. Guroff, G.; Reifsnyd.Ca; Daly, J., Retention of Deuterium in P-Tyrosine Formed Enzymatically from P-Deuterophenylalanine. *Biochem. Biophys. Res. Commun.* **1966**, *24* (5), 720-&.
44. Kappock, T. J.; Harkins, P. C.; Friedenber, S.; Caradonna, J. P., Spectroscopic and Kinetic Properties of Unphosphorylated Rat Hepatic Phenylalanine Hydroxylase Expressed in Escherichia Coli - Comparison of Resting and Activated States. *J Biol*

*Chem* **1995**, 270 (51), 30532-30544.

45. Stetter, J. R.; Li, J., Amperometric Gas Sensors - a Review. *Chem Rev* **2008**, 108 (2), 352-366.

46. Feelisch, M.; Stamler, J. S., *Methods in Nitric Oxide Research*. J. Wiley: Chichester ; New York, 1996; p xix, 712 p., 1 leaf of plates.

47. (a) Daubner, S. C.; Hillas, P. J.; Fitzpatrick, P. F., Characterization of Chimeric Pterin-Dependent Hydroxylases: Contributions of the Regulatory Domains of Tyrosine and Phenylalanine Hydroxylase to Substrate Specificity. *Biochemistry-Us* **1997**, 36 (39), 11574-11582; (b) Hertzler. Comparative Studies of Select Mutants of Rat Phenylalanine and Tyrosine Hydroxylases: Mechanistic Investigations. Ph. D. Thesis, Boston University, 2006.

48. Pilbrow, J. R., Effective G-Values for  $S = 3/2$  and  $S = 5/2$ . *J Magn Reson* **1978**, 31 (3), 479-490.

49. Brown, C. A.; Pavlosky, M. A.; Westre, T. E.; Zhang, Y.; Hedman, B.; Hodgson, K. O.; Solomon, E. I., Spectroscopic and Theoretical Description of the Electronic-Structure of  $S=3/2$  Iron-Nitrosyl Complexes and Their Relation to O-2 Activation by Nonheme Iron Enzyme Active-Sites. *J Am Chem Soc* **1995**, 117 (2), 715-732.

50. Bloom, L. M.; Benkovic, S. J.; Gaffney, B. J., Characterization of Phenylalanine-Hydroxylase. *Biochemistry-Us* **1986**, 25 (15), 4204-4210.

51. Wallick, D. E.; Bloom, L. M.; Gaffney, B. J.; Benkovic, S. J., Reductive Activation of Phenylalanine-Hydroxylase and Its Effect on the Redox State of the Non-Heme Iron. *Biochemistry-Us* **1984**, 23 (6), 1295-1302.

52. Salerno, J. C.; Siedow, J. N., Nature of the Nitric-Oxide Complexes of Lipooxygenase. *Biochim Biophys Acta* **1979**, 579 (1), 246-251.

53. Ray, M.; Golombek, A. P.; Hendrich, M. P.; Yap, G. P. A.; Liable-Sands, L. M.; Rheingold, A. L.; Borovik, A. S., Structure and Magnetic Properties of Trigonal Bipyramidal Iron Nitrosyl Complexes. *Inorg Chem* **1999**, 38 (13), 3110-3115.

## CHAPTER II

### AN EPR INVESTIGATION OF A N,N,O FACIALLY COORDINATED NON-HEME IRON MODEL SYSTEM

#### 2.1 INTRODUCTION

In the previous chapter we presented the CW-EPR spectra of two aromatic amino acid non-heme iron hydroxylases that were treated with NO to produce a Fe-NO complex that was consistent with a  $S = 3/2$  spin state that had a large axial zero field interaction. It was also shown that these CW-EPR spectra change in rhombicity and line-width upon substrate and co-substrate addition. In order to more thoroughly understand the electronic structure of these non-heme Fe enzymes and relate the observed changes to structure, it would be useful to examine a magnetic model system. A Fe(II)-NO model system would allow us to more easily characterize the EPR spectrum without having to consider the complication presented by the protein framework or the substrates.

#### 2.2 Fe-NO ELECTRONIC STRUCTURE

In their review of metal nitrosyl complexes and their bonding, Enemark and Feltham coined a notation which is useful for describing metal nitrosyls. This notation is written as  $\{MNO\}^n$ , where M is a transition metal and n stands for the number of d-type electrons in the complex, which includes those from the metal and one from the NO.<sup>1</sup> For example, the Fe(II)-NO system we've examined in the previous chapter would be classified as  $\{FeNO\}^7$ , this includes the 6 valence electrons of the Fe(II) plus one from the NO. While this notation is useful as a basic description of these systems, it does not accurately describe the specific electronic structure of these complexes. Knowledge of

the the specific electronic structure is necessary for the structural characterization of metal nitrosyls using EPR methods.

Table 2.1 : {FeNO}<sup>7</sup> Formalisms

Reference	Fe d-electrons	Fe spin	NO spin	Coupling
Brown <sup>2</sup>	5	S=5/2	S=1	anti-ferromagnetic
Bill <sup>3</sup> Hoffman <sup>4</sup>	7	S=3/2	S=0	none
Pohl <sup>5</sup>	5	S=1/2	S=2	ferromagnetic
Salerno <sup>6</sup>	6	S=2	S=1/2	anti-ferromagnetic

The electronic structure of non-heme {FeNO}<sup>7</sup> has been examined in a variety of studies using different spectroscopic methods, magnetic measurements and calculations. These studies have proposed a number of formalisms to describe the {FeNO}<sup>7</sup> complexes, the formalisms which are consistent the CW-EPR results, namely the S = 3/2 spectrum, are shown in table 2.1.

One of the more recent and accepted interpretations was proposed by the Solomon group. It was suggested that {FeNO}<sup>7</sup> is best described as a high spin(S = 5/2), ferric(d<sup>5</sup>) iron which is anti-ferromagnetically coupled to a reduced nitric oxide(S = 1), this yields a total spin, S = 3/2.<sup>7</sup> This interpretation is strongly supported by a number of different experimental approaches including X-ray absorption spectroscopy, Raman spectroscopy and Magnetic Circular Dichroism.<sup>2</sup>

Fe K-edge X-ray absorption spectroscopy(XAS) performed on Fe(EDTA)(NO) and Fe(Me<sub>3</sub>TACN)(NO)(N<sub>3</sub>)<sub>2</sub> produced a pre-edge feature with a line shape and energy

consistent with an iron in a high spin ferric oxidation state.<sup>2</sup> In addition, the extended X-ray absorption fine structure (EXAFS) analysis of the first coordination shell provided distances which, when compared to  $\text{Fe(III)(EDTA)(H}_2\text{O)}$  and  $\text{Fe(II)(EDTA)(H}_2\text{O)}$ , are shorter than those of a ferrous complex, closer to that of a ferric species.<sup>8</sup> This description of the  $\{\text{FeNO}\}^7$  unit was further supported by resonance Raman spectroscopy. The NO and the NO-Fe vibrational frequencies were measured and gave values between the expected values for  $\text{NO}^0$  and  $\text{NO}^-$ , consistent with a partially reduced NO ligand.<sup>2</sup> Charge transfer transitions observed in absorption and MCD spectroscopy also agree with the description of  $\{\text{FeNO}\}^7$  composed of a  $S = 5/2$  ferric anti-ferromagnetically coupled to a  $S = 1$   $\text{NO}^-$  ligand.<sup>2</sup>

There are conflicting results for this interpretation from Mössbauer spectroscopy and EPR. Mössbauer spectra collected on the non-heme cofactor iron of putidamonooxin provided an isomer shift which, when compared to shifts of known electron configuration, was too large for a  $d^5$  configuration and was assigned as  $d^7$ .<sup>3</sup> These results combined with the observed  $S = 3/2$  EPR spectrum prompted the interpretation proposed by Bill et al, where the iron is  $d^7$  and contains all the unpaired spin density.<sup>3</sup> Similar results were obtained from a Mössbauer study of Deoxy Hemerythrin, again the isomer shift for the  $\{\text{Fe-NO}\}^7$  center was not consistent with the Solomon interpretation of a  $d^5$   $\text{Fe}(S = 5/2)$ .<sup>9</sup> In this work the authors suggested that rather than using an idealized electronic configuration of Fe or NO that it is more appropriate to consider the  $\{\text{FeNO}\}^7$  as a complete unit where some valence electrons are shared across the moiety.

Further evidence for the breakdown of the idealized electronic configuration

suggested by Solomon comes from EPR measurements made in the Hoffman lab. Deuterium Electron Nuclear Double Resonance (ENDOR) measurements were performed on the non-heme ferrous sites in naphthalene 1,2-dioxygenase<sup>4a</sup> and ACC oxidase<sup>4b</sup> treated with NO. The <sup>2</sup>H hyperfine couplings measured in these ENDOR studies provided dipole-dipole distances for the coupling between specifically deuterated substrates and the Fe center that compared well with X-ray crystallographic studies. In addition, a recent <sup>2</sup>H-electron spin echo envelope modulation (ESEEM) spectroscopy study of taurine dioxygenase in our lab provided deuterium dipolar couplings for specifically deuterated substrate taurine to the iron that also agreed well with predictions from crystal structures.<sup>10</sup>

The two formalisms presented here would interpret the structural EPR results, specifically the dipolar interaction, differently. An interaction between a nuclear dipole and the first formalism, a  $S = 5/2$  ferric anti-ferromagnetically coupled to a  $S = 1$  NO<sup>-</sup> ligand, cannot be explained by the point dipole approximation, since the individual spins of the Fe and NO and their coupling in the {FeNO}<sup>7</sup> unit need to be considered. This leads to the necessity to use spin projection factors to properly describe the dipole-dipole coupling.<sup>11</sup> This entails calculating multiple point dipole approximations and scaling these interactions by the degree of coupling between the two spin containing species.<sup>12</sup> The second formalism, in which the NO donates an electron to the Fe producing a  $d^7$   $S = 3/2$  center, can properly utilize the point dipole approximation. This formalism works in the context of the previously reported ENDOR and ESEEM results where the dipolar coupling was reported in terms of the distance between Fe and the deuterated substrate

using the point dipole approximation, results which agreed well with distances observed in crystallographic studies of the same systems.<sup>4a 4b 10</sup>

### 2.3 N,N,O MODEL SYSTEM

Our collaborators in the lab of John Caradonna at Boston University devised a series of three models in order to mimic the magnetic structure of the His-His-Glu facial triad observed in the non-heme iron hydroxylases. The series of ligands, shown in figure 2.1, contains a facially coordinating N,N,O group that is modified by one or two additional carboxyl groups, this allows for a comparison of the properties of iron complexes containing *fac*-N,N,O(N<sub>2</sub>O<sub>1</sub>) with three *fac* exchangeable sites, N,N,O,O(N<sub>2</sub>O<sub>2</sub>) with *cis* exchangeable sites, and N,N,O,O,O(N<sub>2</sub>O<sub>3</sub>) with one exchangeable site, in which the number of coordinated carboxylate ligands is varied from one to three. The CW-EPR spectra acquired on these three models should provide insights into the Hamiltonian parameters we've collected for TyrH and PheH.

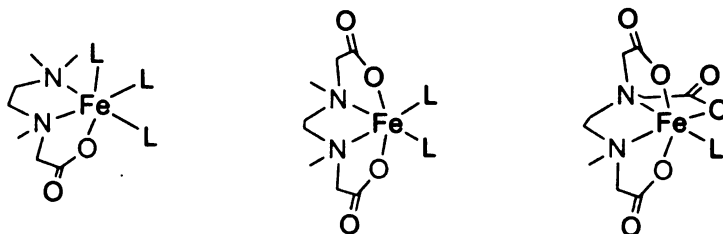


Figure 2.1: Structures of FeN<sub>2</sub>O<sub>1</sub> (left), FeN<sub>2</sub>O<sub>2</sub> (middle) and FeN<sub>2</sub>O<sub>3</sub> (right)

As suggested in the previous chapter, the CW-EPR spectra of {FeNO}<sup>7</sup> systems do not contain any easily measurable structural information. Much of the ligand hyperfine structure is obscured by inhomogeneous broadening in the CW-EPR spectrum. Pulsed EPR techniques such as electron spin echo envelope modulation(ESEEM)

spectroscopy or pulsed electron nuclear double resonance (ENDOR) have been developed to address this problem. Application of these techniques to the model system will provide more detailed information about the local magnetic environment of the  $\{\text{FeNO}\}^7$  and in combination with the known structural data we can characterize the contributions from the ligand and solvent. These assignments will be useful in helping to understand the more complicated magnetic environment of the enzymes.

## 2.4 WATER ANALYSIS

One important aspect of this model system is the variable number of exchangeable coordination sites which will allow for the development of a method to characterize the water coordination in non-heme iron. Some previous work for the determination of water coordination in non-heme iron enzymes includes  $^{17}\text{O}$  line broadening in a variety of different systems<sup>13 14</sup> and ENDOR studies of naphthalene 1,2-dioxygenase<sup>4a</sup> and ACC oxidase<sup>4b</sup>. Although the  $^{17}\text{O}$  line broadening studies provide an indication whether or not the  $\{\text{FeNO}\}^7$  has a coordinated water ligand, it does not provide any quantitative information regarding the water. The basis behind this technique is to compare the CW-EPR lineshape of  $\{\text{FeNO}\}^7$  in  $^{17}\text{O}$  enriched  $\text{H}_2\text{O}$  to the line shape in un-enriched  $\text{H}_2\text{O}$ , if a change in the linewidth is observed, the result of hyperfine broadening, it is concluded that the  $\{\text{FeNO}\}^7$  has a coordinated water.<sup>13</sup> The problem with this technique is that it is impossible to directly measure the hyperfine interaction and all information regarding the number of waters and the location with respect to the magnetic axes is lost.

These problems were overcome in the Hoffman lab with the application of more advanced EPR techniques such as ENDOR which can be used to directly probe the

hyperfine values. In ACC oxidase the presence of Fe bound water was established using ENDOR to detect the hyperfine coupling to H<sub>2</sub><sup>17</sup>O and D<sub>2</sub>O.<sup>4b</sup> These two methods did provide hyperfine coupling values for the interaction with a coordinated water however they both face complications. The <sup>17</sup>O resonance faced significant overlap with non-exchangeable nitrogen features, which was compounded with overlap from non-exchangeable hydrogen at fields lower than g~2.8. Additionally, due to the broad linewidth of the <sup>17</sup>O feature it was impossible to determine the orientation or the number of waters coordinated.<sup>4b</sup> The <sup>2</sup>H ENDOR also provided couplings that were consistent with a coordinated water however they were unable to perform a field dependent analysis due to the signal rapidly attenuating at g < 3.8.<sup>4b</sup>

The problems seen in the ENDOR experiments, namely the resonance overlap, could be avoided with a 2-dimensional experiment. One such method, hyperfine sublevel correlation(HYSCORE) spectroscopy largely avoids the problem of resonance overlap by correlating the hyperfine frequencies of the nuclei in 2 dimensions hopefully separating features that would otherwise overlap in 1 dimension.<sup>15</sup> Application of HYSCORE spectroscopy to the model system should allow for the systematic characterization of the interaction with coordinated water without the use of extensive isotopic labeling.

## 2.5 HYDROGEN HYPERFINE COUPLING

The following discussion of the hydrogen hyperfine interaction is based on the interpretation by Hutchinson and McKay.<sup>16 17</sup> The interaction of the {FeNO}<sup>7</sup> center with a distant hydrogen(I = 1/2) can be characterized with the following Hamiltonian:

$$\hat{H} = \hat{H}_e - g_n \beta_n \mathbf{H}_0 \cdot \hat{\mathbf{I}} + \hat{\mathbf{S}} \cdot \hat{\mathbf{A}} \cdot \hat{\mathbf{I}} \quad [2.1]$$

The first term, the electron Hamiltonian, is described in the previous chapter in equation 1.1. This term determines the energy differences between the sub-levels of the  $\pm 1/2$  Kramers doublet of the  $\{\text{FeNO}\}^7$  unit. As was shown in equations 1.2a-c, the zero field interaction can be rewritten in terms of three effective g-values. Using these three effective g-values and the projection of the magnetic field into the principle axis system of the zero field interaction:

$$\mathbf{H}_0 = H_0 \begin{pmatrix} l_x \\ l_y \\ l_z \end{pmatrix} \quad [2.2]$$

in which  $l_1 = \cos \varphi_e \sin \theta_e$ ,  $l_2 = \sin \varphi_e \sin \theta_e$ ,  $l_3 = \cos \theta_e$  are the direction cosines, the electron Hamiltonian can be rewritten as:

$$\hat{H}_e = \beta_e H_0 \begin{pmatrix} \hat{S}_x & \hat{S}_y & \hat{S}_z \end{pmatrix} \cdot \begin{pmatrix} g_{x,eff} & 0 & 0 \\ 0 & g_{y,eff} & 0 \\ 0 & 0 & g_{z,eff} \end{pmatrix} \cdot \begin{pmatrix} l_x \\ l_y \\ l_z \end{pmatrix} \quad [2.3]$$

an effective electron Zeeman interaction. Diagonalizing this portion of the Hamiltonian allows for the electron spin angular momentum operator to be rewritten in the eigenbasis of the effective g-tensor principle axis system as:

$$\hat{S}_e = \frac{\hat{S}_z}{g_{eff}} \cdot \begin{pmatrix} g_{x,eff} l_x \\ g_{y,eff} l_y \\ g_{z,eff} l_z \end{pmatrix} \quad [2.4]$$

where

$$g_{eff} = \sqrt{(g_{x,eff} l_x)^2 + (g_{y,eff} l_y)^2 + (g_{z,eff} l_z)^2} = \frac{h\nu}{\beta_e H_0} \quad [2.5]$$

This effective electron Zeeman interaction is the dominant term in equation 2.1 being several orders of magnitude greater than the remaining two terms which can be treated as

perturbations on the eigenstates. The first term, the nuclear Zeeman interaction, is independent of the g-frame and represents a field dependent splitting of the nuclear spin sub-levels. The second term is the hyperfine interaction, where  $\mathbf{A}$  represents the sum of the dipolar interaction and the isotropic Fermi contact interaction. In the case of a distant hydrogen, the Fermi contact term is near zero and this term can be neglected. The remaining term, the dipolar interaction, is the energy of the interaction between the field induced by the  $\{\text{FeNO}\}^7$  at the hydrogen and the nuclear magnetic moment. By assuming that the  $\{\text{FeNO}\}^7$  unit is a point dipole located at the Fe, this field is given as

$$H_d = \frac{\mu_e}{r^3} \cdot (3\hat{r}\hat{r} - \mathbf{E}) \quad [2.6]$$

where  $r$  is the distance between the Fe and the hydrogen,  $\hat{r}$  is the unit vector pointing in the direction of the vector connecting the Fe and hydrogen,  $\mathbf{E}$  is the unit dyadic and  $\mu_e$  is the electron magnetic moment given as

$$\mu_e = -\beta_e \mathbf{g} \cdot \hat{S}_e \quad [2.7]$$

where  $\mathbf{g}$  is a diagonal matrix composed of the effective g values of the dipole and  $\hat{S}_e$  is the electron spin operator given in equation 2.4. Substituting equation 2.7 into 2.6 and expressing  $\hat{r}$  in the g axis system the dipolar field is given as:

$$\hat{H}_d = \frac{-\beta_e \hat{S}_e}{r^3} \cdot \begin{pmatrix} g_{x,eff}(3r_1^2-1) & 3g_{x,eff}r_1 \cdot r_2 & 3g_{x,eff}r_1 \cdot r_3 \\ 3g_{y,eff}r_1 \cdot r_2 & g_{y,eff}(3r_2^2-1) & 3g_{y,eff}r_3 \cdot r_2 \\ 3g_{z,eff}r_1 \cdot r_3 & 3g_{z,eff}r_2 \cdot r_3 & g_{z,eff}(3r_3^2-1) \end{pmatrix} \quad [2.8]$$

where  $r_1 = \cos \varphi_N \sin \theta_N$ ,  $r_2 = \sin \varphi_N \sin \theta_N$ ,  $r_3 = \cos \theta_N$ , are the three direction cosines relating the vector that connects the Fe and the hydrogen to the principle axis of the g tensor. This field interacts with the nuclear dipole producing the hyperfine term seen in

equation 2.1:

$$\hat{H}_d \cdot \mu_H = \hat{S}_e \cdot A \cdot \hat{I} \quad [2.9]$$

where:

$$A = \frac{-\beta_e \beta_N g_H}{r^3} \begin{pmatrix} g_{x,eff}(3r_1^2-1) & 3g_{x,eff}r_1 \cdot r_2 & 3g_{x,eff}r_1 \cdot r_3 \\ 3g_{y,eff}r_1 \cdot r_2 & g_{y,eff}(3r_2^2-1) & 3g_{y,eff}r_3 \cdot r_2 \\ 3g_{z,eff}r_1 \cdot r_3 & 3g_{z,eff}r_2 \cdot r_3 & g_{z,eff}(3r_3^2-1) \end{pmatrix} \quad [2.10]$$

Often the dipole-dipole coupling is referenced to  $g_e = 2.0023$ , however as can be seen in equation 2.10 the dipolar coupling is scaled by the effective g-values, this means that there is an enhancement of the interaction depending on its orientation with respect to the g principle axis system.

Due to the anisotropy in the effective g tensor, when operating at a fixed field and frequency, the resonance condition seen in equation 2.5 is only satisfied with a limited set of  $\theta_e$ 's and  $\varphi_e$ 's resulting in single crystal like spectra. This also results in a field dependance in the effective spin operator,  $\hat{S}_e$ , which scales the hyperfine interaction by the effective g value. For example a hyperfine coupling recorded near  $g=4$  would provide a value double that of the same coupling at  $g = 2$ .

## 2.6 EXPERIMENTAL

All reagents used are commercially available and most were used as received. Prior to its use methanol was distilled over magnesium metal and freeze-pump-thawed (FPT) for four cycles. All manipulations involving ferrous complexes and nitrosyl adducts were carried out in an inert atmosphere ( $N_2$ ) glovebox, except where noted. Nitric oxide (NO) gas (99+%) was purchased from Air Gas (Maumee, OH) and used without further purification.

The ferrous complexes  $\text{Fe}^{\text{II}}(\text{N}_2\text{O}_3)(\text{L})$ ,  $\text{Fe}^{\text{II}}(\text{N}_2\text{O}_2)(\text{L}_2)$  and  $\text{Fe}^{\text{II}}(\text{N}_2\text{O}_1)(\text{L}_3)$  were prepared by literature procedures.  $^{18}\text{NO}$  adducts of  $\text{Fe}^{\text{II}}(\text{N}_2\text{O}_3)(\text{L})$ ,  $\text{Fe}^{\text{II}}(\text{N}_2\text{O}_2)(\text{L}_2)$  and  $\text{Fe}^{\text{II}}(\text{N}_2\text{O}_1)(\text{L}_3)$  were prepared as follows. Stock solutions of  $\text{Fe}^{\text{II}}(\text{N}_2\text{O}_3)(\text{L})$ ,  $\text{Fe}^{\text{II}}(\text{N}_2\text{O}_2)(\text{L}_2)$  and  $\text{Fe}^{\text{II}}(\text{N}_2\text{O}_1)(\text{L}_3)$  were prepared in degassed  $\text{H}_2\text{O}$  and  $\text{D}_2\text{O}$  pH 6.5 MOPS buffer and brought out of the glovebox in a schlenk flask. The flask was evacuated and the headspace above the stirring sample was subsequently charged with 3-5 PSI of NO gas at which point the colorless solution turned immediately orange with the formation of  $\{\text{FeNO}\}^7$ . The sample was allowed to stir for  $\sim 1$  min, the flask was evacuated and the sample was brought back into the inert atmosphere glovebox for further manipulation. Samples for EPR analyses were diluted to 5mM with degassed 50:50 glycerol/ $\text{H}(\text{D})_2\text{O}$  as glassing agent for  $\sim 40\%$  final glycerol content. The samples were loaded into EPR tubes, frozen in  $\text{N}_2$  (l), and shipped in a dewared vessel at  $\text{N}_2$  (l) temperatures.

CW-EPR spectra were recorded on a Bruker ESP300E X-band EPR spectrometer equipped with a  $\text{TE}_{102}$  cavity and an Oxford Instruments ESR-900 liquid helium cryostat with a model ITC-502 temperature controller. CW-EPR measurements were made with the following conditions: sample temperature, 4.0 K; microwave frequency, 9.46 GHz; microwave power, 1 mW; magnetic field modulation frequency, 100 kHz; field modulation amplitude, 5 G; conversion time, 163 ms. CW-EPR data were analyzed using the X-SOPHE program available from Bruker Biospin Corporation.

Pulsed EPR measurements were made on a Bruker E-680X spectrometer operating at X-band and equipped with a model ER 4118X-MD-X5-W1 probe that employs a 5mm dielectric resonator. The temperature was maintained at 4.0 K using an

Oxford Instruments liquid helium flow system equipped with a CF-935 cryostat and an ITC-503 temperature controller. HYSORE data were collected using a four-pulse sequence,  $90^\circ\text{-}\tau\text{-}90^\circ\text{-}t_1\text{-}180^\circ\text{-}t_2\text{-}90^\circ$ , with  $90^\circ$  microwave pulse widths of 16 ns (FWHM) and the  $180^\circ$  microwave pulse widths was adjusted between 24-36 ns for optimal turning angle. The tau value was chosen to suppress the hydrogen matrix contribution; due to short phase memory times, tau values were restricted to less than 200 ns. An integration window of 28 ns was used to acquire spin echo amplitude, and data set lengths were 128 points with a 24 ns time increment. The data were processed using tools provided by Bruker. The time domain data was corrected by subtracting a third order polynomial, optimized at each slice, from both time dimensions. The resulting data was tapered with a Hamming window function in both dimensions and the real part was 2-dimensional Fourier transformed. The HYSORE spectra were obtained by taking the absolute value of the transforms.

Simulations of the hyperfine couplings were accomplished using scripts written in MATLAB. The calculations were performed in the time domain using the density matrix formalism of Mims.<sup>19</sup> The  $^1\text{H}$  HYSORE scripts were based on the analytical formula given by Gemperle,<sup>20</sup> while the  $I = 1$  script is based on a simplified summation formula given by Dikanov<sup>21</sup>. The orientation-dependent Hamiltonian used was modeled after work by Hutchison and McKay and is described above.<sup>16</sup> Processing of the simulations, also performed in Matlab, was identical to that described above for the experimental spectra.

## 2.7 RESULTS

## 2.7.1 FERRIC CW-EPR

As an initial study of the ligand system, we examined CW-EPR spectra of the ferric complexes, this was to determine if in solution the ligand coordinates the iron in a mono-nuclear fashion as observed in the crystal structures obtained on the complexes.

Seen in figure 2.2 are the CW-EPR spectra of Fe(III)-N<sub>2</sub>O<sub>1</sub> (a), Fe(III)-N<sub>2</sub>O<sub>2</sub> (b) and

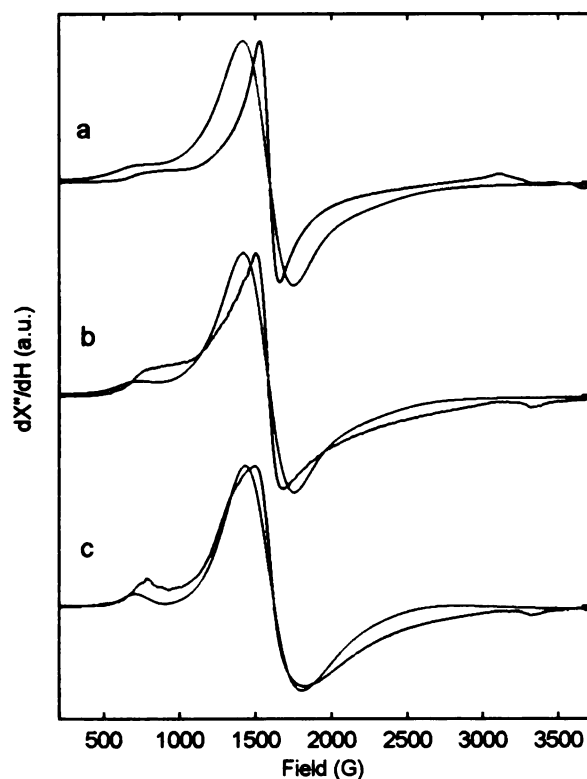


Figure 2.2: CW-EPR of ferric N<sub>2</sub>O<sub>1</sub> (a), N<sub>2</sub>O<sub>2</sub> (b), and N<sub>2</sub>O<sub>3</sub> (c) shown in black with corresponding simulations shown in red.

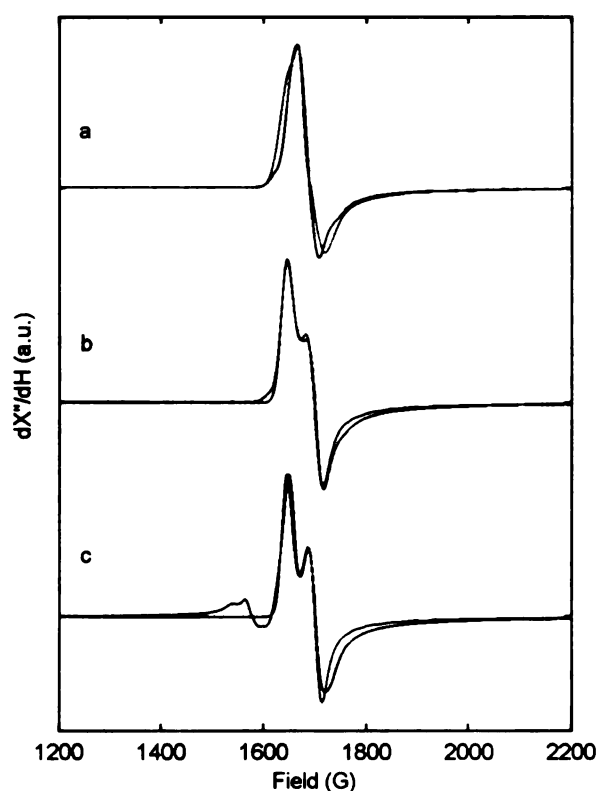
Fe(III)-N<sub>2</sub>O<sub>3</sub> (c). All three model complexes show spectra typical of a single high-spin Fe(III) in a ligand field of rhombic symmetry which is indicated by a low field feature at  $g \sim 9$  and a broad feature with an inflection at  $g = 4.3$ . Shown in red are the corresponding simulations for a  $S = 5/2$  system which utilized a Hamiltonian similar to the one described in Chapter 1. All three simulations utilized identical  $g$ -,  $D$ -,  $E/D$ -,  $D$ -strain and intrinsic linewidth values, in order to account for the

changes observed the  $E/D$  strain was adjusted. In the calculations the  $g$ -value was taken to be isotropic with  $g_0 = 2.00$ , the zero field interaction parameters were taken to be rhombic with  $D = 0.30 \text{ cm}^{-1}$  and  $E/D = 0.23$ . The spectra show broad features at  $g = 4.3$ , because of this the intrinsic EPR linewidth selected for all three simulations was chosen

to be large,  $0.030 \text{ cm}^{-1}$  with a strain in  $D$  of  $0.1 \text{ cm}^{-1}$ . The  $E/D$  strain was adjusted to account for the lineshape changes, a strain in  $E/D$  of  $0.20$  was used in fig. 2.2a, a strain in  $E/D$  of  $0.16$  was used in fig 2.2b, and a strain in  $E/D$  of  $0.06$  was used in fig 2.2c.

### 2.7.2 $\{\text{FeNO}\}^7$ CW-EPR

To properly compare the results from the model system to those from the enzyme it is necessary to examine the  $\{\text{FeNO}\}^7$  adduct. The model system was prepared using



ferrous iron in  $\text{H}_2\text{O}$  and was treated with  $\text{NO}$ . The CW-EPR spectra of the three models  $\{\text{FeNO}\}^7\text{-N}_2\text{O}_1$  (a),  $\{\text{FeNO}\}^7\text{-N}_2\text{O}_2$  (b) and  $\{\text{FeNO}\}^7\text{-N}_2\text{O}_3$  (c) are shown in figure 2.3. The three spectra show line-shapes indicative of the lower Kramers doublet of a  $S = 3/2$  spin system with  $|D| \gg g_e \beta_e H_0$ . Shown in red are the simulations generated using the procedure outlined in the previous chapter. Similar to the previous

results of the ferric model system all three

Figure 2.3: CW-EPR of  $\{\text{FeNO}\}^7 \text{N}_2\text{O}_1$  (a), simulations utilized identical  $g$ -,  $D$ -,  $E/D$ -,  $\text{N}_2\text{O}_2$  (b), and  $\text{N}_2\text{O}_3$  (c) shown in black with corresponding simulations shown in red.  $D$ -strain and intrinsic linewidth values. To

account for the changes in the observed lineshape, the  $E/D$  strain was adjusted. In the calculations the  $g$ -value was taken to be isotropic with  $g_0 = 2.00$ , the zero field interaction parameters were taken to be nearly

axial with  $D = 10.0 \text{ cm}^{-1}$  and  $E/D = 0.0115$ . The intrinsic EPR linewidth selected for all three simulations was taken to be  $0.0015 \text{ cm}^{-1}$  with no strain in  $D$ . The  $E/D$  strain was adjusted to account for the lineshape changes, a strain in  $E/D$  of  $0.0075$  was used in fig. 2.3a, a strain in  $E/D$  of  $0.0045$  was used in fig 2.3b, and a strain in  $E/D$  of  $0.0035$  was used in fig 2.3c

### 2.7.3 $\{\text{FeNO}\}^7$ HYSCORE

As suggested in the previous chapter, the CW-EPR results do not provide details of metal ligation. More advanced techniques are necessary to determine specific structural information. One specific technique which has proven useful for evaluating and interpreting complicated spectra is HYSCORE spectroscopy.<sup>22</sup> HYSCORE spectra of the  $\{\text{FeNO}\}^7$  model complexes were acquired at multiple positions in the field range from  $g = 4$  to  $g = 2$ . This was done in order to properly take into account the single crystal like selection of orientations imposed by the anisotropy in the EPR spectrum. The analysis of these spectra utilized multiple field positions; however, to give a brief overview, only representative spectra acquired at  $1980 \text{ G}(g_{\text{eff}} = 3.489)$  and  $3100 \text{ G}(g_{\text{eff}} = 2.229)$  will be shown in this section.

Seen in figures 2.4 and 2.5 are the HYSCORE spectra of  $\{\text{FeNO}\}^7\text{-N}_2\text{O}_1$  at  $1980 \text{ G}$  and  $3100 \text{ G}$ , respectively. Both spectra show features in the  $(++)$  quadrant in the frequency regime expected for hydrogen hyperfine couplings. The spectrum collected at  $1980 \text{ G}$  shows disperse clouds along the frequency diagonal with intensity at  $9.5 \text{ MHz}$  and  $11 \text{ MHz}$ . Weak crosspeaks were observed in the  $(++)$  quadrant in range from  $(5,13) \text{ MHz}$  to  $(7,9) \text{ MHz}$ , this feature at most had 30% of the maximum intensity of the feature

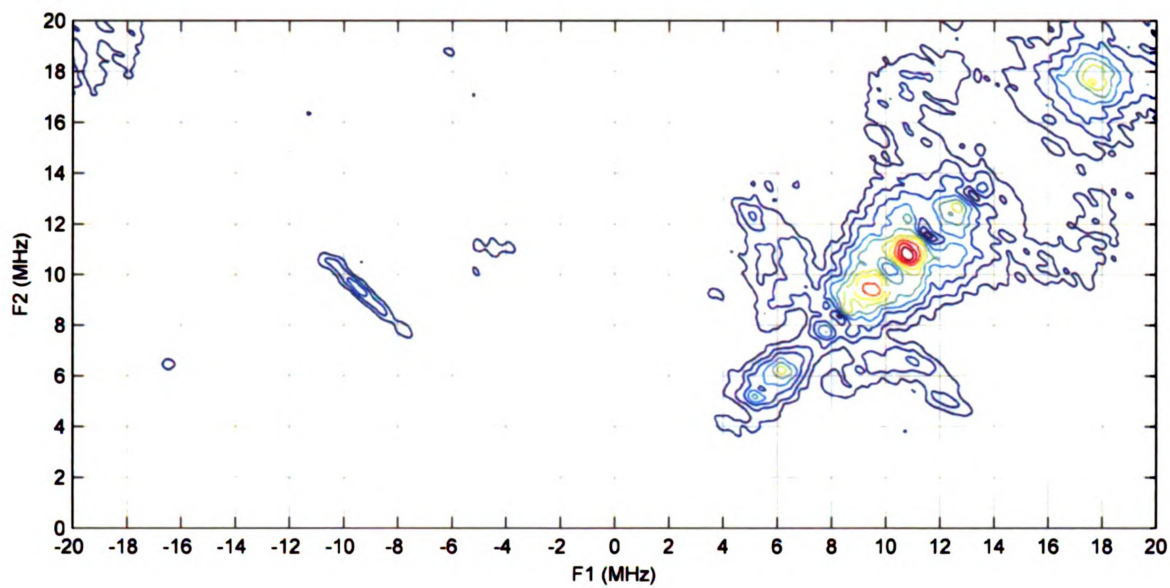


Figure 2.4: HYSCORE spectrum of  $\{\text{FeNO}\}^7\text{-N}_2\text{O}_1$  recorded at 1980 G

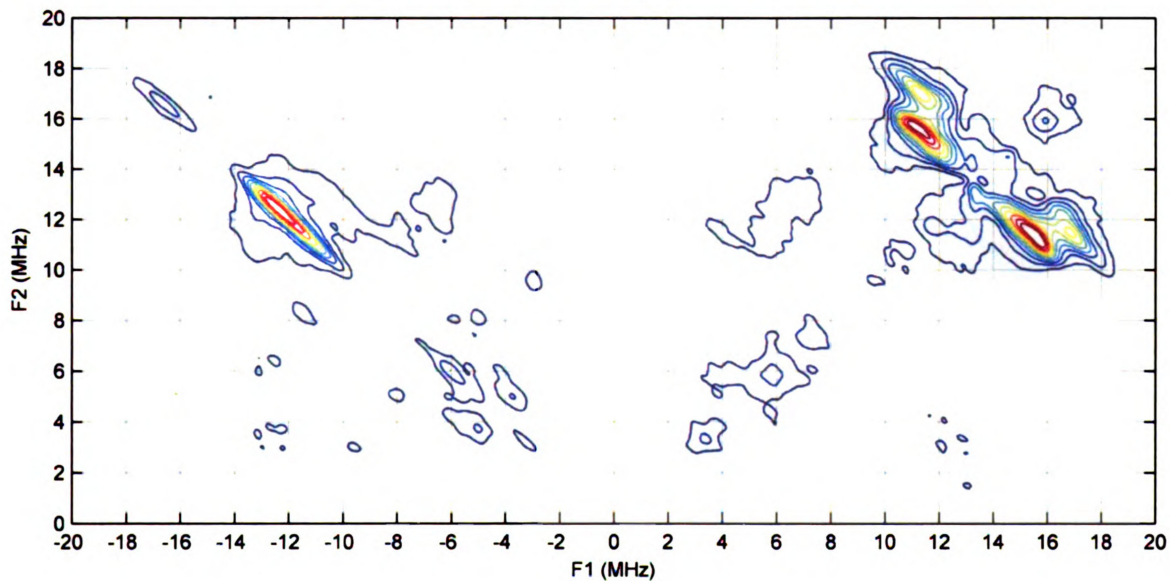


Figure 2.5: HYSCORE spectrum of  $\{\text{FeNO}\}^7\text{-N}_2\text{O}_1$  recorded at 3100 G

observed along the diagonal. At 3100 G a set of two distinct crosspeaks were observed in the (++) quadrant, the more intense feature has a maximum at (11.5,15.5) MHz, the other higher frequency feature is 30% less intense and has a maximum at (11.5,17) MHz.

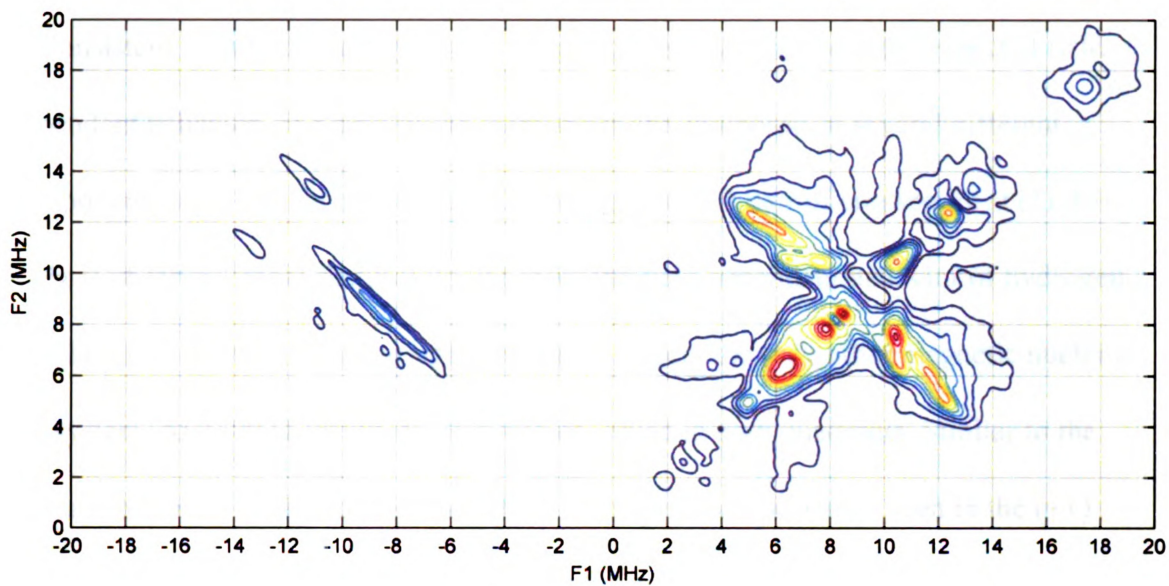


Figure 2.6: HYSCORE spectrum of  $\{\text{FeNO}\}^7\text{-N}_2\text{O}_2$  recorded at 1980 G

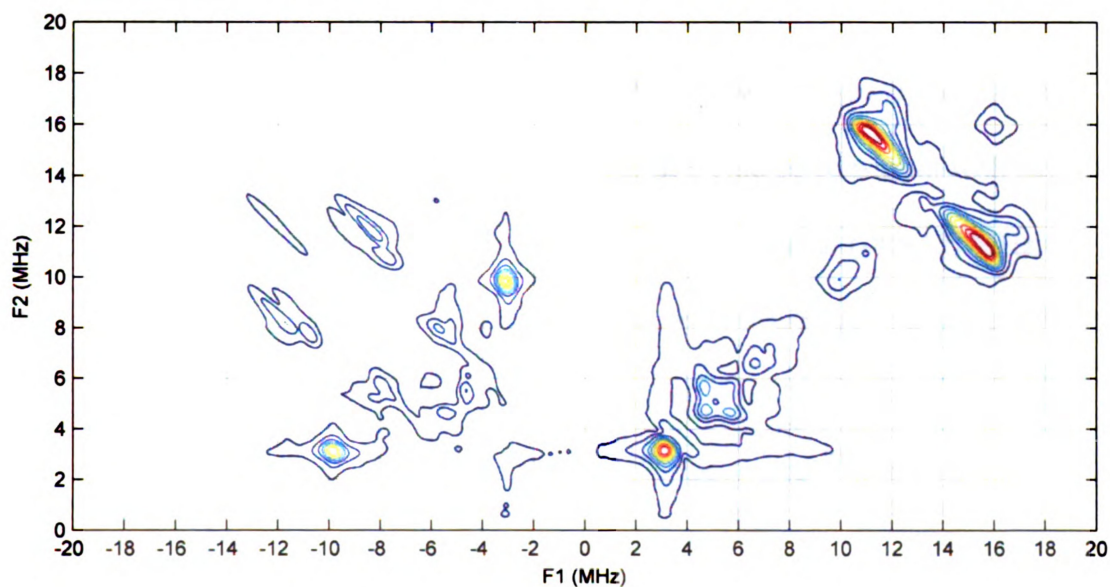


Figure 2.7: HYSCORE spectrum of  $\{\text{FeNO}\}_7\text{-N}_2\text{O}_2$  recorded at 3100 G

Seen in figures 2.6 and 2.7 are the HYSCORE spectra of  $\{\text{FeNO}\}^7\text{-N}_2\text{O}_2$  at 1980 G and 3100 G, respectively. In figure 2.7, non-diagonal features are observed in both the  $(++)$  and  $(-+)$  quadrants. The crosspeaks in the  $(++)$  quadrant fall in a region which would

be consistent with hydrogen hyperfine couplings and they do show the expected field dependent behavior. The crosspeaks themselves are composed of several different components with varying maxima. In the (-+) quadrant a pair of crosspeaks at (11,13) MHz is observed, these features do not show the field dependent behavior of hydrogen and therefore must be from strongly coupled nitrogen, the only other magnetic nuclei in the system. At 3100 G crosspeaks are also observed in both quadrants. Similar to the features observed in figure 2.5, two sets of hydrogen crosspeaks are seen in the (++) quadrant. The more intense feature has a maximum at (11.5,15.5) MHz and a line shape similar to the analogous peak in figure 2.5. This intense feature largely obscures a second component of higher frequency at (12,17) MHz, compared to the same component in figure 2.5 there is a decrease in amplitude relative to the lower frequency hydrogen feature. In the (-+) quadrant, two sharp features which would be consistent with strongly coupled nitrogen are observed, one at (-3,10) MHz and the other at (-8.5,12) MHz.

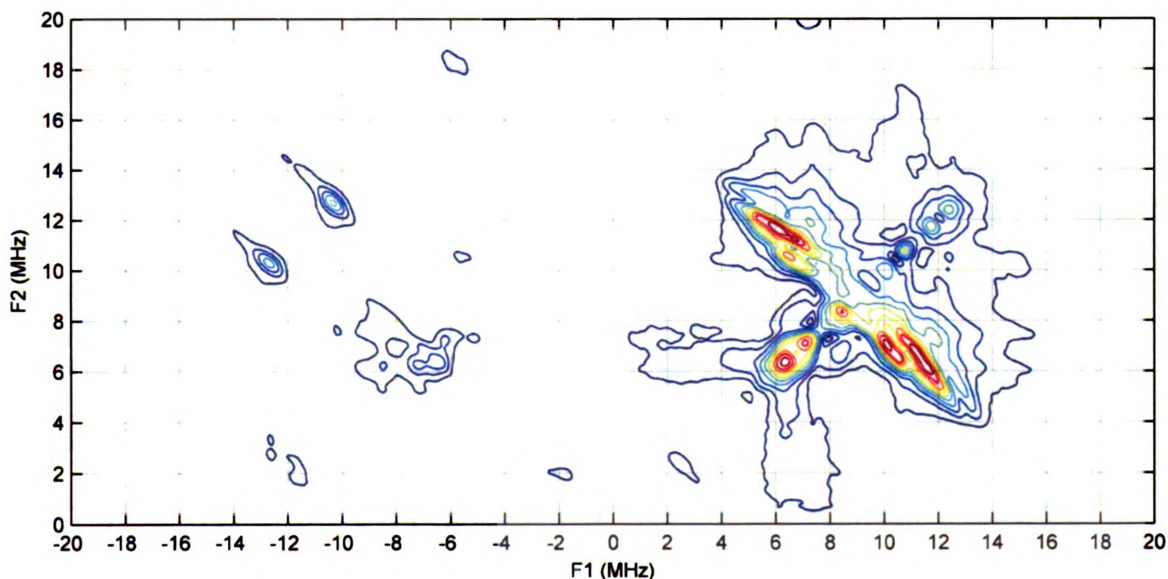


Figure 2.8: HYSCORE spectrum of  $\{\text{FeNO}\}^7\text{-N}_2\text{O}_3$  recorded at 1980 G

Seen in figures 2.8 and 2.9 are the HYSCORE spectra of  $\{\text{FeNO}\}^7\text{-N}_2\text{O}_3$  at 1980 G and 3100 G, respectively. These two spectra show similarities to the spectra acquired on  $\text{N}_2\text{O}_2$  at the same field positions. At 1980 G there are the hydrogen crosspeaks in the (++) quadrant and the strong nitrogen peaks in the (-+) quadrant at (-10.5,13) MHz. The spectrum acquired at 3100 G contains only a single hydrogen crosspeak in (++) quadrant

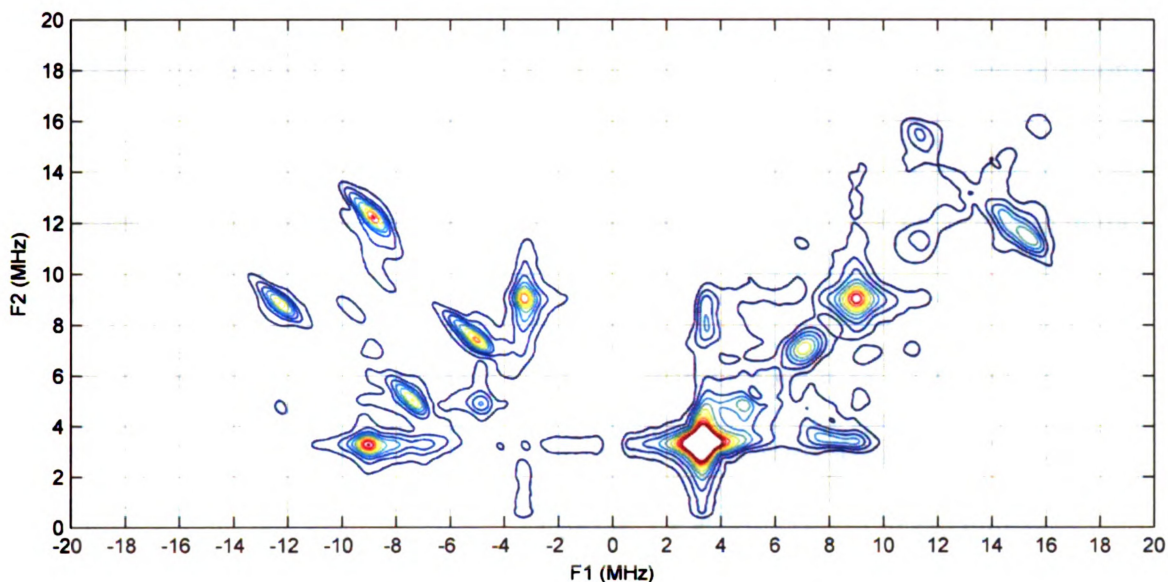


Figure 2.9: HYSCORE spectrum of  $\{\text{FeNO}\}^7\text{-N}_2\text{O}_3$  recorded at 3100 G

which has a local maxima at (11.5,15.5) MHz,  $\text{N}_2\text{O}_3$  lacks the higher frequency hydrogen feature seen in the other two models. The (-+) quadrant at 3100 G contains three sharp features which would be consistent with strongly coupled nitrogen, one at (-3,9), (-5,7.5) and at (-9,12) MHz.

These HYSCORE spectra provide hyperfine coupling information about the magnetic nuclei near the  $\{\text{FeNO}\}^7$  center. The ligand systems provide two nitrogens, a variable number of non-exchangeable hydrogens and in the open coordination sites water

molecules. In order to properly assign the features observed in the HYSORE it is necessary to perform simulations.

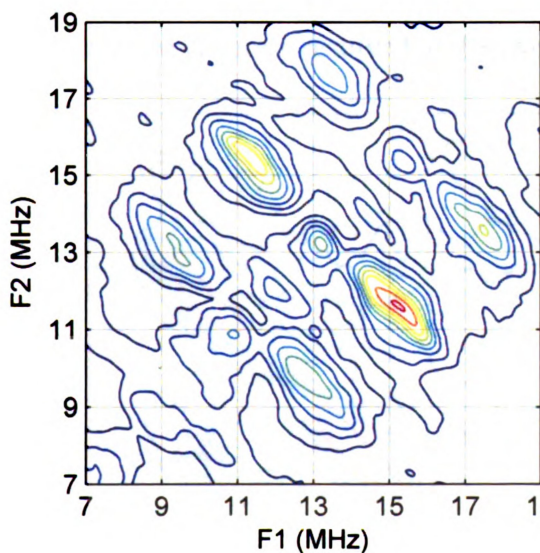
#### 2.7.4 WATER ANALYSIS

In the HYSORE spectra at both low field and high field features consistent with hydrogen were observed. In order to differentiate the non-exchangeable ligand hydrogens from those on the solvent, samples of the three models in D<sub>2</sub>O were prepared.

HYSORE spectra were acquired on the three model systems at multiple field positions to identify the exchangeable features. Upon examination of the spectra it was found that exchangeable features are only present in the spectra of N<sub>2</sub>O<sub>1</sub> and N<sub>2</sub>O<sub>2</sub> acquired in the range from  $g = 2.5$  to  $g = 2$ .

Shown in figure 2.10 is the HYSORE spectrum from N<sub>2</sub>O<sub>1</sub> in a D<sub>2</sub>O buffer at

3100 G. In comparison to figure 2.5 we



observe a disappearance of the higher frequency feature at (11.5,17) MHz. The D<sub>2</sub>O buffer also gives rise to two new crosspeak features at (9.5,13) and (13.5,17.5). Based on the observation that they lie on the same diagonal as the previously reported peak at

(11.5,15.5) its reasonable to assume that they are in fact combination lines. The presence of

the D<sub>2</sub>O buffer results in an extremely intense feature at the Larmour frequency of the

Figure 2.10: HYSORE spectrum of {FeNO}<sup>7</sup>-N<sub>2</sub>O<sub>1</sub> in D<sub>2</sub>O recorded at 3100 G

deuteron arising from dipolar coupling to the bulk solvent and generally referred to as a matrix line. Experimentally, it is possible to suppress the frequency associated with the  $\text{H}_2\text{O}$  matrix peak however the low frequency of the  $\text{D}_2\text{O}$  matrix line makes application of this trick difficult and at the expense of signal to noise ratio so it is not used. The matrix line at 2.1 MHz from the  $\text{D}_2\text{O}$  adds new frequency components at sums and differences of existing, real, features. The two new sets of crosspeaks are approximately at (+2,+2) MHz and (-2,-2) MHz from initial real crosspeaks. These results show that the higher frequency feature at (11.5,17) MHz seen in of the spectrum of  $\text{N}_2\text{O}_1$  in  $\text{H}_2\text{O}$  are from solvent molecules.

To properly simulate the feature identified as water we needed to examined its field dependent behavior. Shown in figures 2.11 – 2.15 is the (++) quadrant of the HYSORE of  $\text{N}_2\text{O}_1$  at 2800 G, 2900 G, 3000 G, 3100 G, and 3200 G, respectively. The water feature is barely resolved at the two extreme field positions shown and is not

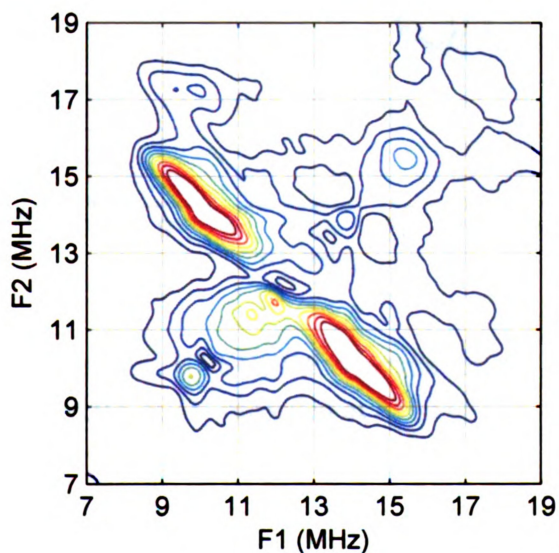


Figure 2.11: HYSORE spectrum of  $\{\text{FeNO}\}^7\text{-N}_2\text{O}_1$  recorded at 2800 G

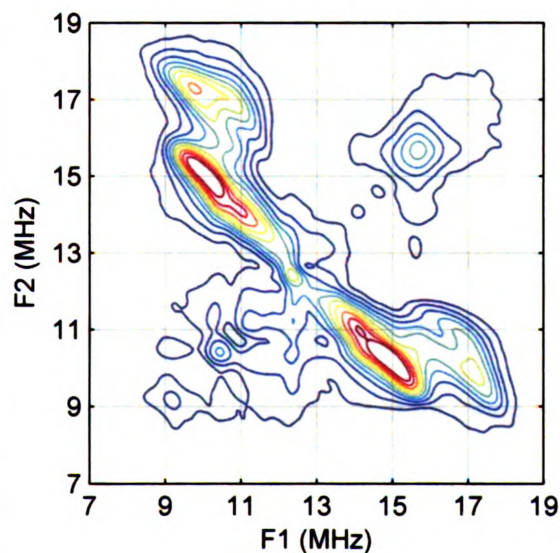


Figure 2.12: HYSORE spectrum of  $\{\text{FeNO}\}^7\text{-N}_2\text{O}_1$  recorded at 2900 G

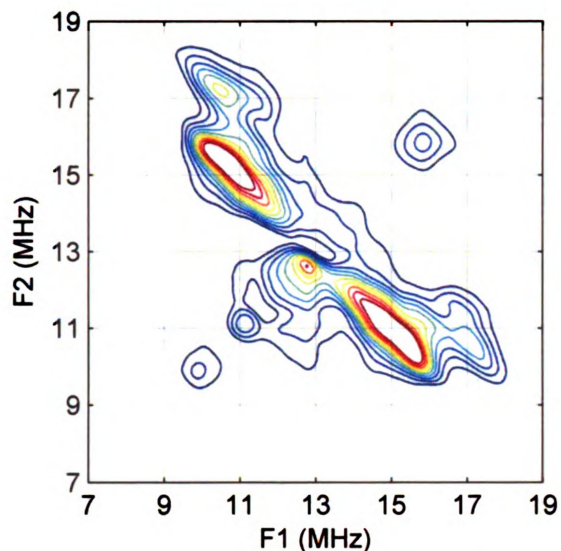


Figure 2.13: HYSCORE spectrum of  $\{\text{FeNO}\}^7\text{-N}_2\text{O}_1$  recorded at 3000 G

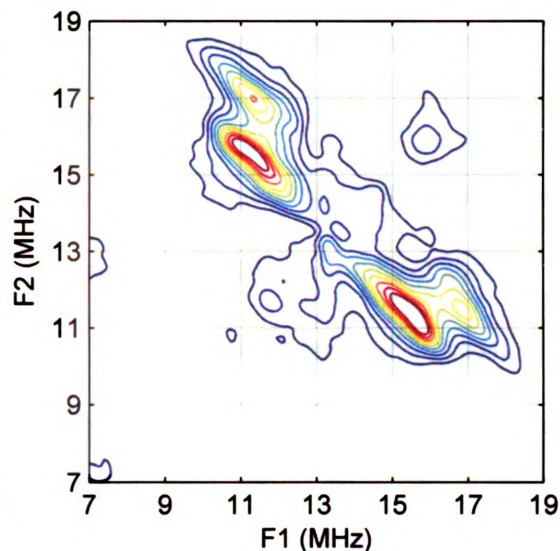


Figure 2.14: HYSCORE spectrum of  $\{\text{FeNO}\}^7\text{-N}_2\text{O}_1$  recorded at 3100 G

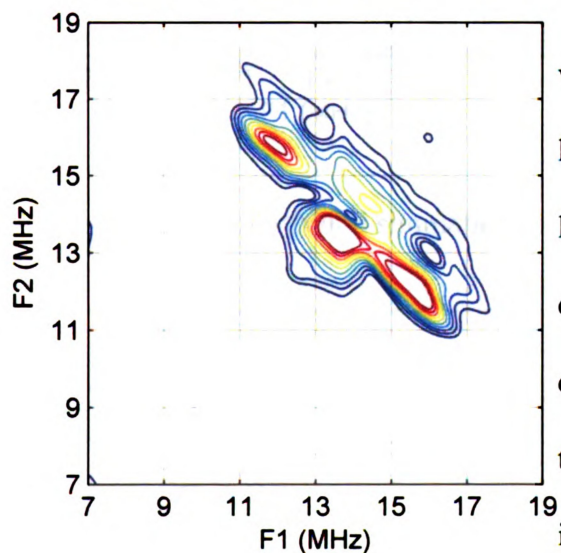


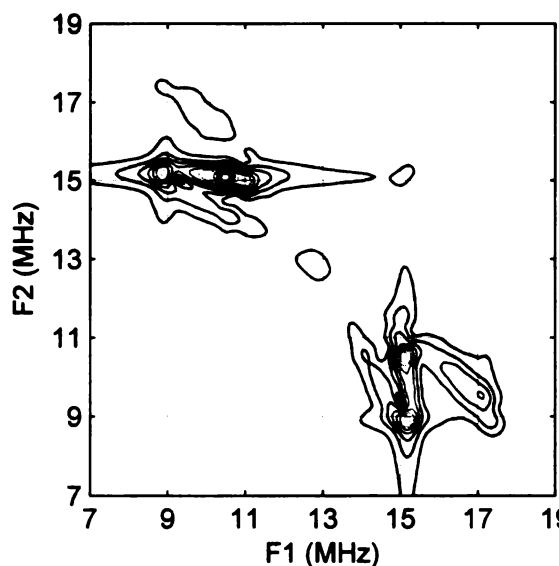
Figure 2.15: HYSCORE spectrum of  $\{\text{FeNO}\}^7\text{-N}_2\text{O}_1$  recorded at 3200 G

visible at field positions recorded higher or lower than those. At 2800 G and 2900 G the lineshape of the water feature appears to be composed of two slightly different components, at the higher field positions these two components overlap and are indistinguishable. It was observed that the water feature moves with field along a constant frequency, approximately along F2 above the diagonal or F1 below the diagonal.

This observation is key in identifying the proper orientation of the Fe hydrogen dipole-dipole vector with respect to the Fe-NO bond. The overall higher

frequency characteristic of the water feature indicates that it has a stronger hyperfine interaction than the other non-exchangeable hydrogen feature.

Shown in figures 2.16 – 2.20 are the simulations of the water feature at 2800 G, 2900 G, 3000 G, 3100 G, and 3200 G, respectively. The simulations utilized two



sets of hyperfine parameters to distinguish between the two features seen at 2800 G and 2900 G. One simulation used a dipolar distance of 2.58 Å and an angle between the dipole-dipole vector and Fe-NO bond of 1.2 radians, the second feature used a dipolar distance of 2.56 Å and an angle between the dipole-dipole vector and Fe-NO bond of 1.25

Figure 2.16: <sup>1</sup>H HYSCORE simulation at 2800 G

radians. To generate the spectra these two

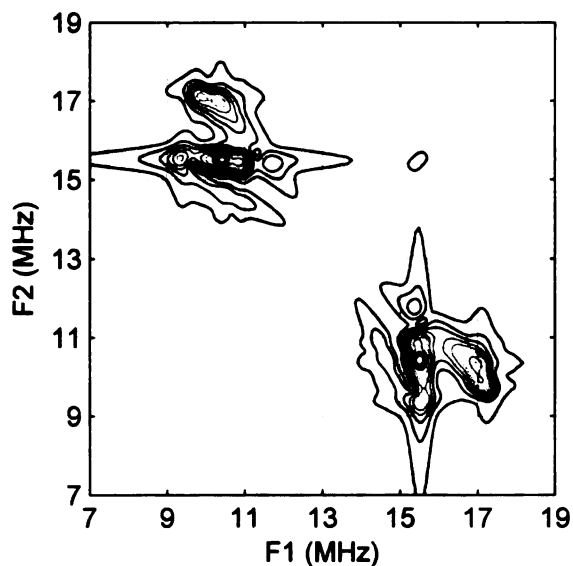


Figure 2.17: <sup>1</sup>H HYSCORE simulation at 2900 G

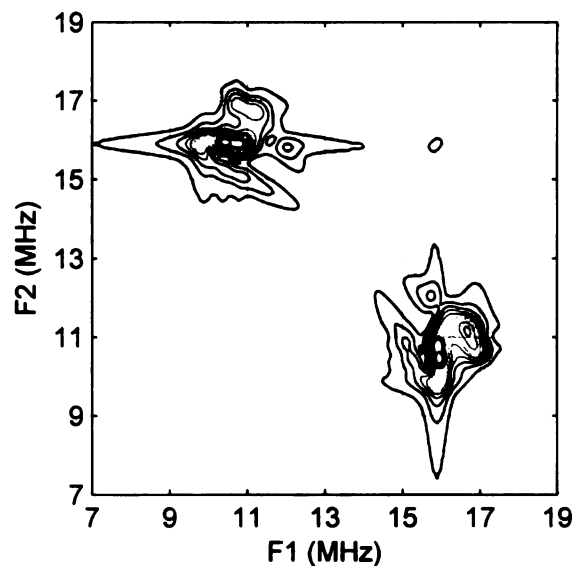


Figure 2.18: <sup>1</sup>H HYSCORE simulation at 3000 G

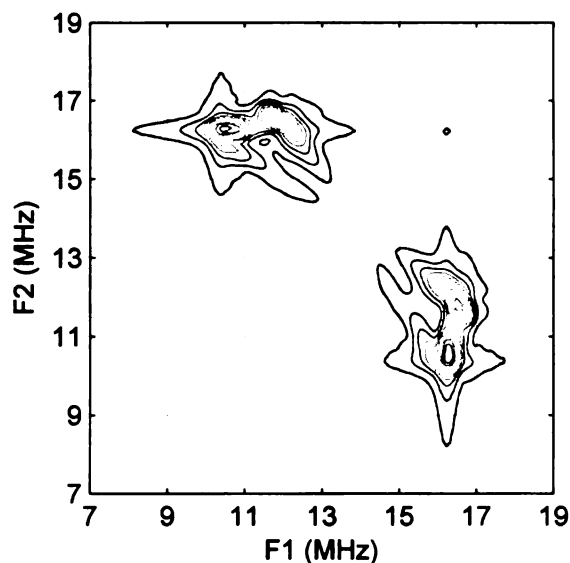


Figure 2.19:  $^1\text{H}$  HYSCORE simulation at 3100 G

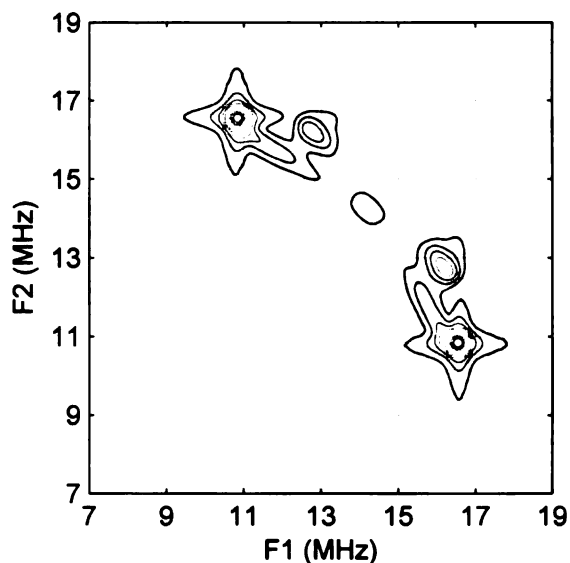


Figure 2.20:  $^1\text{H}$  HYSCORE simulation at 3200 G

simulations were assembled according to the product rule.<sup>19 23</sup>

Seen in figure 2.7, we observe that  $\text{N}_2\text{O}_2$  contains the higher frequency feature that we've attributed to water. This was further confirmed when the spectrum of  $\{\text{FeNO}\}^7\text{-N}_2\text{O}_2$  in  $\text{D}_2\text{O}$  buffer was examined and the water feature was no longer present. The simulation obtained for the second hydrogen feature accurately represented the water feature observed in  $\{\text{FeNO}\}^7\text{-N}_2\text{O}_2$ . The spectrum of  $\text{N}_2\text{O}_3$  seen in figure 2.9, as expected, does not contain the higher frequency feature that we've attributed to water hydrogen a result further confirmed when examining the spectrum in  $\text{D}_2\text{O}$ .

### 2.7.5 LIGAND HYPERFINE ANALYSIS

In addition to the exchangeable features attributed to water ligands several other non-exchangeable features are observed in the HYSCORE spectra. It can be assumed that these non-exchangeable features are either from interactions with the chelating ligand or

the NO. Preliminary analysis of these features was performed on the  $N_2O_3$  model system in order to ensure that the Fe-NO axis was fixed and the uncertainty in the orientation is minimized. Shown in figure 2.21 is a simulation performed at 3100 G using two different nitrogens, the first nitrogen utilized the following parameters:  $A=[6.5,6.5,8.5]$  MHz, an angle between the dipolar vector and the Fe-NO bond of 0.23 radians,  $e^2Qq=4.5$  MHz with an  $\eta=0.1$ ; the second nitrogen used the following parameters:  $A=[7.5,7.5,9.5]$  MHz, an angle between the dipolar vector and the Fe-NO bond of 1.3 radians,  $e^2Qq=4.5$  MHz with an  $\eta=0.1$ .

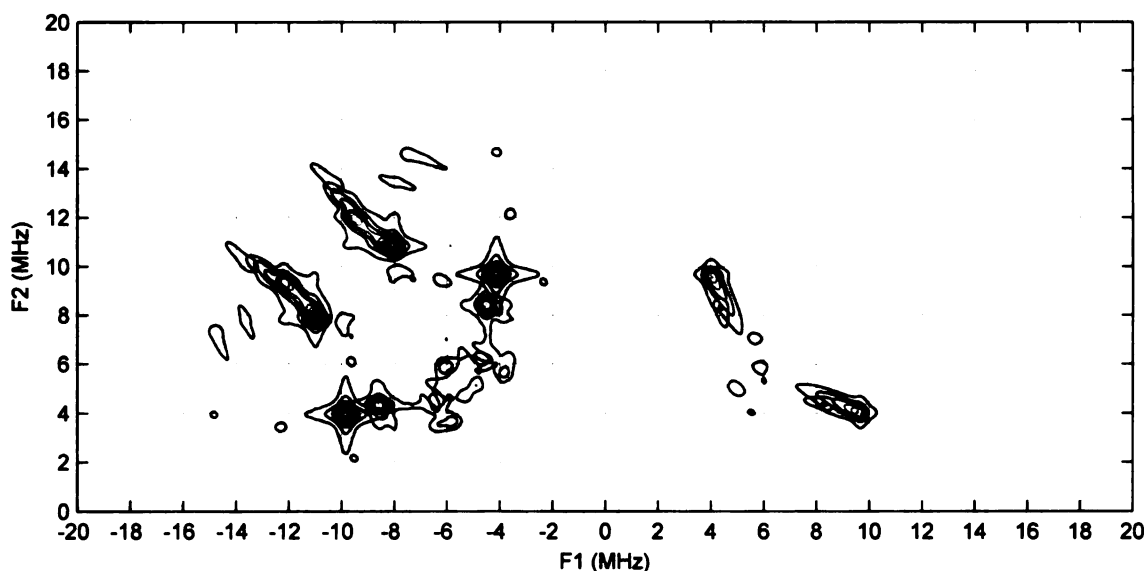


Figure 2.21:  $^{14}N$  HYSCORE simulation at 3100 G

The ligand system contains 13 different hydrogens at a variety of orientations found in the range between 3.2 – 4.0 Å. The resolution of our experiment does not allow us to distinguish between individual hydrogens making their assignment nearly impossible. Preliminary simulations suggest the observed features arise only from the closest hydrogens, those near 3.2 Å.

## 2.8 DISCUSSION

EPR spectroscopic methods were used to examine a series of mono-nuclear non-heme iron model complexes. These complexes were synthesized to mimic the facial N,N,O coordination motif common in mono-nuclear non-heme iron oxygenases and to provide a spectroscopic model to help in the analysis of more complicated enzyme systems. To more thoroughly characterize the coordination sphere, the base N,N,O frame was modified by one or two additional coordinating carboxylate arms.

The CW-EPR spectra recorded on the Fe(III) complexes were consistent with what is expected for high-spin( $d^5$ ) mono-nuclear complexes and the parameters used in the simulations are commensurate with previous work on Fe(III) model complexes<sup>24</sup> and non-heme Fe(III) sites in proteins.<sup>25 26</sup> The increase in E/D strain observed in the EPR measurements shows that the distribution of electronic structures represented in the samples is increasing with the number of open coordination sites on the metal ion. This result is not entirely unexpected as the increase in open coordination sites on the iron allows for more solvent which, unlike the ligand, can adopt a range of different conformers which adds to the distribution of structures. While these results are interesting they do not provide any tangible structural information about the model complexes. Pulsed EPR methods were also attempted on the ferric complexes with no success, a result likely due to the large structural dispersion observed in the CW-EPR spectra.

When the model system is reduced and treated with NO, the CW-EPR spectra show sharp resonances at  $g = 4$  and  $g = 2$ , characteristic of a  $S = 3/2$ ,  $\{\text{FeNO}\}^7$  unit. The parameters used in the simulations were largely held constant in order to reflect the

structural similarities between the three models and the E/D strain was adjusted to account for the lineshape differences. This leads to a trend for the  $\{\text{FeNO}\}^7$  complexes similar to the one observed in Fe(III) namely that there is an increase in E/D strain with increasing number of open coordination sites or with an increase in ligand chelation the E/D strain decreases. Again a similar justification can be used, the increase in the number of solvent molecules, which can adopt a range of different conformers, adds to the distribution of electronic structures observed. The observation of significant E/D strain in both the ferric and ferrous-NO systems provides evidence that this effect is in part independent of the NO coordination however the presence of the NO cannot be neglected.

The three models,  $\text{N}_2\text{O}_3$ ,  $\text{N}_2\text{O}_2$  and  $\text{N}_2\text{O}_1$  have 1, 2 and 3 open coordination sites respectively, clearly in  $\text{N}_2\text{O}_3$ , the NO binds at the lone, open coordination site. However, in the latter two models, the binding position of the NO is not defined by the ligand structure. The observed increase in E/D strain with number of open coordination sites could be a result of this ambiguity in the NO binding, instead of observing line broadening we could be observing a mixture of overlapping species. A recent study by Borovik et al showed a correlation between the value of E/D and the angle of the Fe-N-O bond, as the projection of the oxygen onto the plane perpendicular to the Fe-N bond increases so does the value of E/D.<sup>27</sup> Based on this result, the Fe-N-O angle would be expected to decrease as the ligand becomes less chelating, allowing the NO ligand to bind in a more bent fashion, the result of which would be an increase in E/D.<sup>27</sup> This contradicts the experimental results, the lineshape becomes more axial as the

carboxylates are replaced by solvent across the series. So while a mixture of discrete E/D species is a possible reason for the change in lineshape, we would expect  $N_2O_2$  and  $N_2O_1$  to have mixture of rhombic species rather than axial, lending to the further support that the E/D strain, the result of a broad distribution of electronic structures, is the cause for line broadening observed.

The near axial nature of the zero field interaction in the  $\{FeNO\}^7$  model complexes when the ligand backbone is clearly not axially symmetric is rather interesting. The shift away from being purely axial, designated by E/D, is only 0.0115 of a maximum of 1/3, so the model complexes only show 3.5% rhombicity. This near axial interaction remains even with the relatively major changes to the iron coordination moving through the ligand series. Lineshape changes aside, this suggests that the zero field interaction of  $\{FeNO\}^7$  unit is relatively insensitive to changes in the Fe coordination environment and, as shown by Borovik et al, is more sensitive to changes in the NO bonding.<sup>27</sup>

The HYSCORE spectra collected on the  $\{FeNO\}^7$  model complexes show two types of features, one from hydrogen and the other from strongly coupled nitrogen, both of these results are expected based on the structure of the ligand complex. The assignments of these features in the model complex will aid in the analysis of HYSCORE results acquired on non-heme iron enzymes, in addition these assignments should provide the details necessary to determine the orientation of NO bond and thus the gz axis with respect to the Fe ligands.

A set of preliminary simulations for the nitrogen features in  $N_2O_3$  at 3100 G were

obtained using similar parameters of two different orientations, one approximately perpendicular to the  $g_z$  axis and the other nearly co-linear. In order to shift the phase of the modulation function and produce features in the (-+) quadrant as seen in the HYSORE a large isotropic hyperfine coupling,  $A_{\text{iso}} > 2\nu_n$ , is necessary. The isotropic hyperfine component used in the simulations,  $A_{\text{iso}} = 7.5$  MHz or  $A_{\text{iso}} = 8.5$  MHz are sufficiently large to produce features in the (-+) quadrant; however, this interaction alone is not sufficient to produce the observed features. The two other components, the anisotropy in the hyperfine interaction and the nuclear quadrupole interaction both show an angular dependence that could be used to differentiate the nitrogen orientation with respect to the  $g_z$  axis. One approximation for the anisotropic component of the hyperfine interaction is a dipole-dipole interaction, the Fe-N distances given in the crystal structure of  $\text{N}_2\text{O}_3$  are 2.2 Å for the nitrogen trans to the open coordination site and 2.4 Å for the cis nitrogen. Utilizing the point dipole approximation, these Fe-N distance would translate to  $\sim 0.5$  MHz; however, in the simulations this amount of anisotropy only broadens the peaks and adds no significant angular dependence.

The nuclear quadrupole interaction is the interaction of the nitrogen nucleus with electric field gradient produced by the lone pair of electrons on the nitrogen. The principle axis of this interaction is defined by the lone pair on the nitrogen which, in the model system, is coincident with the Fe-N bond. The magnitude of the nuclear quadrupole interaction used in the simulations,  $e^2Qq = 4.5$  MHz, is consistent with values reported for tri-coordinate nitrogen and falls between the literature values for ammonia and trimethylamine.<sup>28</sup> Based on the similarity to tri-coordinate nitrogen, the Fe-N bond

can be interpreted as not very covalent and closer to an ionic bond. Changing the orientation of the nitrogen with respect to the  $g_z$  axis shifted the features seen in the HYSCORE, a nitrogen perpendicular to  $g_z$  produces the feature at (-9,12), while a co-linear nitrogen produces a peak (-3,9) and a weak feature near (-9,12). The changes seen in the nuclear quadrupole interaction provides a method to differentiate between the cis and trans nitrogen.

Based on the crystal structure of  $N_2O_3$  the assignment of the perpendicular nitrogen is straightforward; however, the co-linear nitrogen could either be from the chelating ligand or the NO. In the treatment used for the hydrogen hyperfine coupling calculations the Fe was treated as a point dipole which means that it contains all of the unpaired spin density of the  $\{FeNO\}^7$  unit; in this case the NO-nitrogen is just as likely to contribute to the HYSCORE as the ligand nitrogen. If there is any delocalization of the unpaired spin density onto the NO, as suggested by the various  $\{FeNO\}^7$  electronic structure formalisms<sup>2</sup>, the isotropic component of the hyperfine interaction would be expected to increase dramatically and the Fe-N bond would become increasingly covalent lowering the quadrupole energy. Based on the similarity of the hyperfine parameters and the quadrupole interaction for the two different nitrogen's it is reasonable to assume that the co-linear nitrogen is ligand based and that the coupling to the NO-nitrogen is too large to be detected in the experiment. Confirmation of these assumption could be made through  $^{15}N$  labeling of the ligand and NO.

The assignment of the non-exchangeable hydrogen features seen in the HYSCORE to the ligand hydrogen's has shown to be difficult. As a rough approximation,

a dipole distance of 3.2 Å to at most 3.5 Å could account for the observed hydrogen features. In the His-His-Glu active site of non-heme Fe oxygenases, this number of non-exchangeable hydrogen's is significantly reduced, down to 4 from the two histidine ligands and assignment should be simplified. In non-heme enzymes a combination of the orientation data for the histidine nitrogen and hydrogen should provide enough constraints to determine the  $g_z$  axis within the enzyme center and thus the NO bond axis.

The HYSCORE spectra of both  $N_2O_1$  and  $N_2O_2$ , in the range of 2800 G to 3200 G, had shown presence of exchangeable hydrogen. Simulations of these hydrogen features provided a dipole-dipole distance of  $\sim 2.6$  Å and an angle relating the dipole-dipole vector and the Fe-NO bond of  $\sim 70^\circ$ , both of these parameters are consistent with those expected for coordinated  $H_2O$ . The angle given more than likely represents a distribution of orientations which culminates with a maximum that can be described by the parameters used for the simulations. Support for a wide distribution of distances and angles is given if the ratio of amplitudes are considered. The observed at 3100 G that the ratio of the amplitude of non-exchangeable to exchangeable max was  $\sim 1.4:1$ , comparing the amplitudes of simulation for a hydrogen 3.2 Å from the iron to one of 2.6 Å gives a ratio of  $\sim 1:6$ . This difference in ratio's could be accounted for in two different ways: The coordinated water adopts a range of different of orientations and only a small percentage of those contribute to the observable features; second, clearly more than one hydrogen is contributing to the non-exchangeable features which would raise the amplitude in that region. Based on some trial simulations the first reason, a range of water orientations, is expected to have a greater influence on the HYSCORE amplitude. This result is not

entirely unexpected since there is nothing in the chelating ligand which restricts the water orientation.

## **2.9 CONCLUSIONS**

A set of three non-heme Fe models were characterized using EPR spectroscopy. In the CW-EPR spectra a correlation can be drawn between the number of labile sites on the iron and E/D strain, an increase in open coordination sites resulted in an increase in E/D strain. The HYSCORE spectra of the three models were recorded and the non-exchangeable features were assigned to chelating ligand hydrogen and nitrogen. The exchangeable hydrogen observed in the HYSCORE spectra of  $N_2O_1$  and  $N_2O_2$  were simulated and assigned to coordinated water.

## 2.10 REFERENCES

1. Enemark, J. H.; Feltham, R. D., Principles of Structure, Bonding, and Reactivity for Metal Nitrosyl Complexes. *Coordin Chem Rev* **1974**, *13* (4), 339-406.
2. Brown, C. A.; Pavlosky, M. A.; Westre, T. E.; Zhang, Y.; Hedman, B.; Hodgson, K. O.; Solomon, E. I., Spectroscopic and Theoretical Description of the Electronic-Structure of  $S=3/2$  Iron-Nitrosyl Complexes and Their Relation to O<sub>2</sub> Activation by Nonheme Iron Enzyme Active-Sites. *J Am Chem Soc* **1995**, *117* (2), 715-732.
3. Bill, E.; Bernhardt, F. H.; Trautwein, A. X.; Winkler, H., Mossbauer Investigation of the Cofactor Iron of Putidamonooxin. *European Journal of Biochemistry* **1985**, *147* (1), 177-182.
4. (a) Yang, T. C.; Wolfe, M. D.; Neibergall, M. B.; Mekmouche, Y.; Lipscomb, J. D.; Hoffman, B. M., Substrate Binding to No-Ferro-Naphthalene 1,2-Dioxygenase Studied by High-Resolution Q-Band Pulsed H<sub>2</sub>-Endor Spectroscopy. *J Am Chem Soc* **2003**, *125* (23), 7056-7066; (b) Tierney, D. L.; Rocklin, A. M.; Lipscomb, J. D.; Que, L.; Hoffman, B. M., Endor Studies of the Ligation and Structure of the Non-Heme Iron Site in Acc Oxidase. *J Am Chem Soc* **2005**, *127* (19), 7005-7013.
5. Pohl, K.; Wieghardt, K.; Nuber, B.; Weiss, J., Preparation and Magnetism of the Binuclear Iron(II) Complexes  $(\text{Fe}(\text{C}_9\text{H}_21\text{n}_3)\text{Ncs}_2)_2$ ,  $(\text{Fe}(\text{C}_9\text{H}_21\text{n}_3)\text{Nco}_2)_2$ ,  $(\text{Fe}(\text{C}_9\text{H}_21\text{n}_3)\text{N}_3)_2$  and Their Reaction with No - Crystal-Structures of  $(\text{Fe}(\text{C}_9\text{H}_21\text{n}_3)(\text{Ncs})_2)_2$  and  $\text{Fe}(\text{C}_9\text{H}_21\text{n}_3)(\text{No})(\text{N}_3)_2$ . *J. Chem. Soc.-Dalton Trans.* **1987**, (1), 187-192.
6. Salerno, J. C.; Siedow, J. N., Nature of the Nitric-Oxide Complexes of Lipoxygenase. *Biochim Biophys Acta* **1979**, *579* (1), 246-251.
7. Zhang, Y.; Pavlosky, M. A.; Brown, C. A.; Westre, T. E.; Hedman, B.; Hodgson, K. O.; Solomon, E. I., Spectroscopic and Theoretical Description of the Electronic-Structure of the  $S = 3/2$  Nitrosyl Complex of Nonheme Iron Enzymes. *J Am Chem Soc* **1992**, *114* (23), 9189-9191.
8. Westre, T. E.; Diccico, A.; Filipponi, A.; Natoli, C. R.; Hedman, B.; Solomon, E. I.; Hodgson, K. O., Determination of the Fe-N-O Angle in  $(\text{Feno})(7)$  Complexes Using Multiple-Scattering EXAFS Analysis by GNXAS. *J Am Chem Soc* **1994**, *116* (15), 6757-6768.
9. Rodriguez, J. H.; Xia, Y. M.; Debrunner, P. G., Mossbauer Spectroscopy of the Spin Coupled  $\text{Fe}^{2+}$ - $\{\text{Feno}\}(7)$  Centers of Nitrosyl Derivatives of Deoxy Hemerythrin and Density Functional Theory of the  $\{\text{Feno}\}(7)(S=3/2)$  Motif. *J Am Chem Soc* **1999**, *121* (34), 7846-7863.
10. Muthukumar, R. B.; Grzyska, P. K.; Hausinger, R. P.; McCracken, J., Probing the Iron-Substrate Orientation for Taurine/Alpha-Ketoglutarate Dioxygenase Using Deuterium Electron Spin Echo Envelope Modulation Spectroscopy. *Biochemistry-US*

2007, 46 (20), 5951-5959.

11. Bertrand, P.; More, C.; Guigliarelli, B.; Fournel, A.; Bennett, B.; Howes, B., Biological Polynuclear Clusters Coupled by Magnetic-Interactions - from the Point Dipole Approximation to a Local Spin Model. *J Am Chem Soc* **1994**, 116 (7), 3078-3086.
12. Elsasser, C.; Brecht, M.; Bittl, R., Pulsed Electron-Electron Double Resonance on Multinuclear Metal Clusters: Assignment of Spin Projection Factors Based on the Dipolar Interaction. *J Am Chem Soc* **2002**, 124 (42), 12606-12611.
13. Arciero, D. M.; Orville, A. M.; Lipscomb, J. D., O-17 Water and Nitric-Oxide Binding by Protocatechuate 4,5-Dioxygenase and Catechol 2,3-Dioxygenase - Evidence for Binding of Exogenous Ligands to the Active-Site Fe-2+ of Extradiol Dioxygenases. *J Biol Chem* **1985**, 260 (26), 4035-4044.
14. Han, A. Y.; Lee, A. Q.; Abu-Omar, M. M., Epr and Uv-Vis Studies of the Nitric Oxide Adducts of Bacterial Phenylalanine Hydroxylase: Effects of Cofactor and Substrate on the Iron Environment. *Inorg Chem* **2006**, 45 (10), 4277-4283.
15. Hofer, P.; Grupp, A.; Nebenfuhr, H.; Mehring, M., Hyperfine Sublevel Correlation (Hyscore) Spectroscopy - a 2d Electron-Spin-Resonance Investigation of the Squaric Acid Radical. *Chem. Phys. Lett.* **1986**, 132 (3), 279-282.
16. Hutchison, C. A.; Mckay, D. B., Determination of Hydrogen Coordinates in Lanthanum Nicotinate Dihydrate Crystals by Nd+3-Proton Double-Resonance. *J Chem Phys* **1977**, 66 (8), 3311-3330.
17. Hurst, G. C.; Henderson, T. A.; Kreilick, R. W., Angle-Selected Endor Spectroscopy .1. Theoretical Interpretation of Endor Shifts from Randomly Orientated Transition-Metal Complexes. *J Am Chem Soc* **1985**, 107 (25), 7294-7299.
18. Cappillino, P. J. M., J. R.; Tyler, L. A.; Lo, W.; Kasibhatla, B. S. T.; Krzyaniak, M. D.; McCracken, J.; Armstrong, W. H.; Caradonna, J. P., *Manuscript in submission* **2010**.
19. Mims, W. B., Envelope Modulation in Spin-Echo Experiments. *Phys Rev B* **1972**, 5 (7), 2409-&.
20. Gemperle, C.; Aebli, G.; Schweiger, A.; Ernst, R. R., Phase Cycling in Pulse Epr. *J Magn Reson* **1990**, 88 (2), 241-256.
21. Dikanov, S. A.; Xun, L. Y.; Karpel, A. B.; Tyryshkin, A. M.; Bowman, M. K., Orientationally-Selected Two-Dimensional Esem Spectroscopy of the Rieske-Type Iron-Sulfur Cluster in 2,4,5-Trichlorophenoxyacetate Monooxygenase from Burkholderia Cepacia Ac1100. *J Am Chem Soc* **1996**, 118 (35), 8408-8416.
22. Schweiger, A.; Jeschke, G., *Principles of Pulse Electron Paramagnetic Resonance*. Oxford University Press: Oxford, UK ; New York, 2001; p xxvi, 578 p.

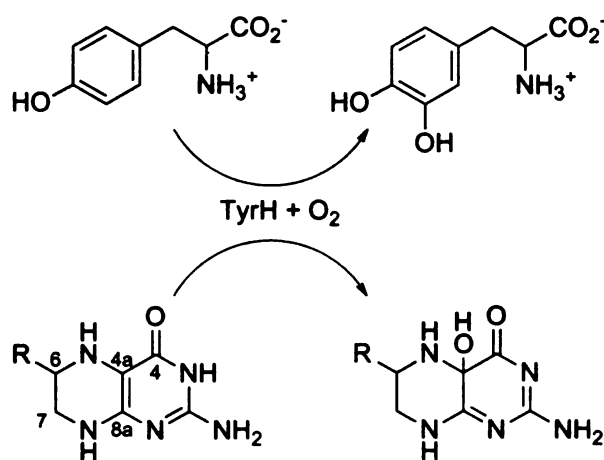
23. Mims, W. B.; Davis, J. L.; Peisach, J., The Accessibility of Type-I Cu(II) Centers in Laccase, Azurin, and Stellacyanin to Exchangeable Hydrogen and Ambient Water. *Biophys J* **1984**, *45* (4), 755-766.
24. Weisser, J. T.; Nilges, M. J.; Sever, M. J.; Wilker, J. J., Epr Investigation and Spectral Simulations of Iron-Catecholate Complexes and Iron-Peptide Models of Marine Adhesive Cross-Links. *Inorg Chem* **2006**, *45* (19), 7736-7747.
25. Doctor, K. S.; Gaffney, B. J.; Alvarez, G.; Silverstone, H. J., Epr Spectroscopy of Interdoublet Transitions in High-Spin Iron - Applications to Transferrin Oxalate. *J Phys Chem-Us* **1993**, *97* (12), 3028-3033.
26. Yang, A. S.; Gaffney, B. J., Determination of Relative Spin Concentration in Some High-Spin Ferric Proteins Using E/D-Distribution in Electron-Paramagnetic Resonance Simulations. *Biophys J* **1987**, *51* (1), 55-67.
27. Ray, M.; Golombek, A. P.; Hendrich, M. P.; Yap, G. P. A.; Liable-Sands, L. M.; Rheingold, A. L.; Borovik, A. S., Structure and Magnetic Properties of Trigonal Bipyramidal Iron Nitrosyl Complexes. *Inorg Chem* **1999**, *38* (13), 3110-3115.
28. Lucken, E. A. C., *Nuclear Quadrupole Coupling Constants*. Academic P.: London, New York., 1969; p x, 360 p.

## CHAPTER III

### STRUCTURAL CHARACTERIZATION OF NO ADDUCTS OF THE NON-HEME FE(II) ACTIVE SITE OF TYROSINE HYDROXYLASE

#### 3.1 INTRODUCTION

Tyrosine hydroxylase (TyrH) is a non-heme iron enzyme that requires tetrahydrobiopterin ( $BH_4$ ) and molecular oxygen to catalyze the hydroxylation of



aromatic ring of L-tyrosine (tyr) to produce L-dihydroxyphenylalanine (DOPA) (Figure 3.1).<sup>1</sup> The production of DOPA as described above is the rate limiting step in the biosynthesis of the catecholamine neurotransmitters.<sup>2</sup> TyrH is a member of the small family of

Figure 3.1: TyrH reaction

tetrahydrobiopterin-dependent aromatic

amino acid hydroxylases that also includes phenylalanine hydroxylase (PheH) and tryptophan hydroxylase (TrpH). This family of enzymes are structurally similar in that they all share similar catalytic sites which contain a non-heme iron coordinated facially by two histidines and a glutamate.<sup>3 4 5</sup> Based on their structural similarities and chemistry, these enzymes have been proposed to follow the same catalytic mechanism (Figure 3.2).<sup>2</sup> This mechanism involves two sequential steps, first, the activation of oxygen using electrons from a tetrahydropterin to yield a high valent, Fe(IV)-oxo hydroxylating intermediate and hydroxylated pterin<sup>6 7</sup> and second the hydroxylation of the side chain of

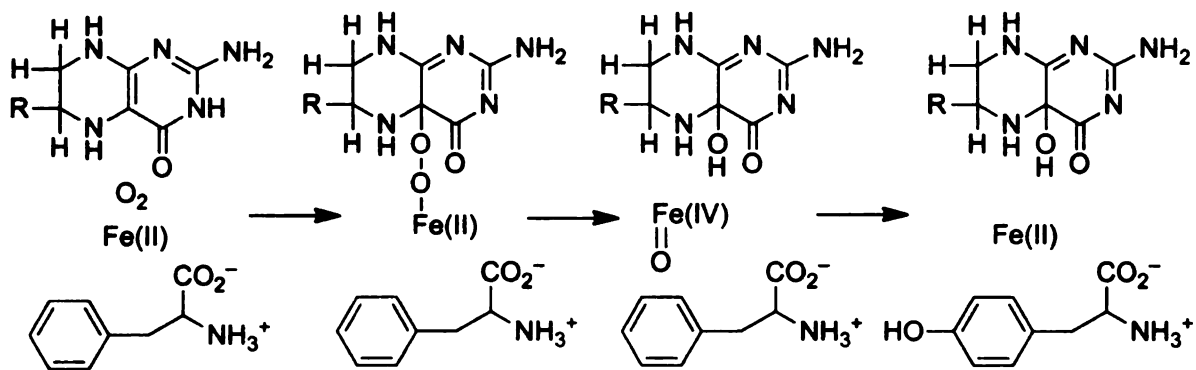


Figure 3.2: TyrH Catalytic Mechanism

amino acid substrate via electrophilic aromatic substitution.<sup>8</sup>

A steady-state kinetic mechanism has been described for rat TyrH that is consistent with an ordered sequential mechanism for substrate binding; the tetrahydropterin binds first followed by molecular oxygen and then finally, substrate tyrosine.<sup>9</sup> No reaction is observed until all three substrates are bound. Fluorescence anisotropy studies have shown that pterin binding to TyrH initiates the movement of an active site loop that packs against the amino acid binding site, providing a structural explanation for the ordered kinetic mechanism.<sup>10</sup> Further, recent single turnover studies have shown that binding of both a tetrahydropterin and tyrosine increase the reactivity of the iron site with oxygen by several orders of magnitude.<sup>11</sup> A combination of spectroscopic approaches have identified changes in the iron ligands when both substrates are bound, wherein the iron converts from hexacoordinate to pentacoordinate and opening up a potential site for oxygen.<sup>11</sup>

While several structures have been described of the aromatic amino acid hydroxylases, there is none with only the primary amino acid substrate bound. Most of

the available structures are of the catalytic domains containing ferric iron in the presence or absence of an oxidized pterin. For example, for TyrH, the only crystal structures reported are for ferric forms of the enzyme in the resting state (1TOH)<sup>3</sup> or with the oxidized cofactor, 7,8 dihydrobiopterin, bound (2TOH)<sup>12</sup>. Exceptions are provided by the structures of PheH. Specifically, X-ray crystallographic studies of ferrous PheH with BH<sub>4</sub> alone<sup>13</sup> and with BH<sub>4</sub> and isoleucine or the phenylalanine analog thienylalanine<sup>4 14</sup> have been reported. Comparison of these crystal structures reveals that the binding of the amino acid to PheH treated with BH<sub>4</sub> reduces the distance between the iron and the C<sub>4a</sub> position of BH<sub>4</sub> from 6 Å to 4.5 Å. Thus, the binding of the amino acid substrate analog initiates a conformational change in PheH that pushes the reduced pterin cofactor closer to the iron.<sup>4</sup> However, it is not known whether similar changes occur in TyrH or even whether the order of substrates binding to the two enzymes is the same.. Additionally, there is also nothing known about the structure of the reactive complex of oxygen, amino acid and pterin in any of these enzymes.

One of the most successful approaches for the EPR characterization of Fe(II) active sites in non-heme enzymes calls for the metal ion to be studied in complex with nitric oxide.<sup>15 16</sup> This technique is ideal for Fe(II) hydroxylases as NO acts as an oxygen surrogate, binding to the iron and preventing catalysis by inhibiting oxygen binding. In addition, NO antiferromagnetically couples with the iron generating an S = 3/2 spin system that is readily detected by EPR spectroscopy.<sup>15 16 17</sup> More recently, Hoffman and co-workers have used the {FeNO}<sup>7</sup>, S = 3/2 spin system together with deuterium Electron Nuclear Double Resonance (ENDOR) spectroscopy to study the non-heme

ferrous sites in naphthalene 1,2-dioxygenase<sup>18</sup> and ACC oxidase<sup>19</sup>. The <sup>2</sup>H hyperfine couplings measured in these ENDOR studies provided deuterium dipole-dipole distances for specifically deuterated substrates that compared well with X-ray crystallographic studies. In addition, a recent <sup>2</sup>H-electron spin echo envelope modulation (ESEEM) spectroscopy study of taurine dioxygenase provided deuterium dipolar couplings for specifically deuterated substrate taurine that agreed well with predictions from crystal structures.<sup>20</sup>

In this chapter, the results of <sup>2</sup>H-ESEEM studies carried out on ferrous TyrH treated with NO, and specifically deuterated cofactor, 6-methyl tetrahydropterin (6-MPH<sub>4</sub>) and substrate L-tyrosine are reported. The EPR studies provide new data on how TyrH controls catalytic activity as the {FeNO}<sup>7</sup> metal center mimics the Fe-O<sub>2</sub> interaction, structural information can be gained from tertiary, TyrH-{FeNO}<sup>7</sup>-6MPH<sub>4</sub>, and quaternary, TyrH-{FeNO}<sup>7</sup>-6MPH<sub>4</sub>-tyr complexes. In addition to wild type enzyme the TyrH mutant E332A, in which oxygen activation is only poorly coupled to amino acid hydroxylation, was examined.

### **3.2 EXPERIMENTAL**

6-Methyltetrahydropterin (6MPH<sub>4</sub>) and 6-methylpterin were purchased from Schircks Laboratories (Jona, Switzerland). 6-(2-Hydroxy-1-methyl-2-nitrosohydrazino)-N-methyl-hexanamine (MAHMA NONOate), ethylenediamine tetraacetic acid (EDTA), 3-(N-morpholino)propanesulfonic acid (Mops), L-tyrosine and glycerol were purchased from Sigma-Aldrich (St. Louis, MO). L-3,5-<sup>2</sup>H-Tyrosine and deuterium gas were from Cambridge Isotopes (Andover, MA). Potassium chloride and ferrous ammonium sulfate

were from Fisher (Pittsburg, PA). 6-CH<sub>3</sub>-6,7-<sup>2</sup>H-tetrahydropterin (Figure 3.1) (d-6MPH<sub>4</sub>) was synthesized by reduction of the commercially available 6-methylpterin to the level of tetrahydropterin using deuterium gas, as previously described.<sup>21</sup> All other chemicals were of the highest purity commercially available.

Wild-type TyrH was expressed in *E. coli* and purified as previously described.<sup>22 23</sup> In order to remove the ferric iron from the protein, the ammonium sulfate pellet at the end of the purification was resuspended in 5 mM EDTA, 200 mM Hepes, (pH 7.5), 10% glycerol and 0.1 M KCl, and incubated on ice for one hour. The enzyme solution was then dialyzed against the same buffer without EDTA and concentrated using Amicon Ultra-15 and Ultra-4 centrifugal filters (Millipore Corp., MA). The enzyme samples for ESEEM were brought to a final glycerol concentration of 30% (v/v) during the concentration stage. The iron content of the apo-enzyme was measured using a Perkin-Elmer Analyst 600 atomic absorption instrument.<sup>24</sup> The typical iron content of an apo enzyme preparation was  $\leq 0.1$  equivalent.

NO Samples for EPR were prepared using MAHMA NONOate as the nitric oxide donor. Stock solutions of MAHMA NONOate were prepared in 0.01 M NaOH just before the experiment and were always kept on ice. Exact concentrations of the MAHMA NONOate solutions were determined from the UV absorbance at 250 nm in 0.01 M KOH, using an extinction coefficient of 7.3 mM<sup>-1</sup>cm<sup>-1</sup>.<sup>25</sup> Highly concentrated stock solutions of tyrosine and 3,5-<sup>2</sup>H-tyrosine (~50 mM) were prepared by bringing the solution to a final pH of ~10. The exact concentrations of the tyrosine stock solutions were determined using an extinction coefficient of 1.34 mM<sup>-1</sup>cm<sup>-1</sup> at 275 nm in 0.1 M HCl. Stock

solutions of the protiated and deuterated  $6\text{MPH}_4$  were prepared in 2 mM HCl, and an extinction coefficient of  $17.8 \text{ mM}^{-1}\text{cm}^{-1}$  in 2 M perchloric acid was used to determine the concentrations. Ferrous ammonium sulfate solutions were prepared fresh by dissolving the appropriate amount of powder in 2 mM HCl. ESEEM samples were prepared inside an anaerobic cuvette at 25 °C. Apo-TyrH (0.9-1.2 mM) and tyrosine (if the complex contained tyrosine) were placed at the bottom of the cuvette. Ferrous ammonium sulfate solution (0.9 equivalent in  $\sim 10 \mu\text{l}$ ) was placed on the lower neck of the cuvette.  $6\text{MPH}_4$  and MAHMA NONOate solutions were either placed in the side arms or on the upper neck of the cuvette, for large and small volumes, respectively. Buffer conditions were 100 mM Mops (pH 7.0), 0.3 M KCl and 30% glycerol. Each MAHMA NONOate molecule releases two molecules of NO,<sup>25</sup> and the half-life of MAHMA NONOate is  $\sim 35$  s under these buffer and temperature conditions (data not shown). The contents of the cuvette (a total volume of  $\sim 250 \mu\text{l}$ ) were made anaerobic by the application of argon-vacuum exchange for at least 20 minutes. The anaerobic enzyme solution was then mixed with ferrous ammonium sulfate and incubated for 10 minutes. This was followed by mixing with  $6\text{MPH}_4$  (if the complex contained  $6\text{MPH}_4$ ). After a few minutes of incubation, MAHMA NONOate ( $\sim 0.6$  equivalent of the enzyme) at the upper neck of the cuvette was introduced to the enzyme-substrate mixture. After  $\sim 3$  minutes,  $\sim 200 \mu\text{l}$  of the reaction mixture was quickly transferred to the quartz EPR tubes (4 mm OD, 707-SQ-250M, Wilmad, Buena, NJ) using a glass pipette and immediately frozen in liquid nitrogen. (UV-Visible experiments performed under similar conditions indicated that the maximum absorbance at 450 nm, which is indicative of NO binding, was reached at about 3 minutes

and stayed constant for at least a few minutes). UV-Visible spectra collected at increasing concentrations of MAHMA NONOate showed that NO was saturating under the concentrations used.

Pulsed EPR measurements were made on a Bruker E-680X spectrometer operating at X band and equipped with a model ER 4118X-MD-X5-W1 probe that employs a 5mm dielectric resonator. The temperature was maintained at 4.0 K using an Oxford Instruments liquid helium flow system equipped with a CF-935 cryostat and an ITC-503 temperature controller. ESEEM data were collected using a three-pulse (stimulated echo) sequence,  $90^\circ$ - $\tau$ - $90^\circ$ -T- $90^\circ$ , with  $90^\circ$  microwave pulse widths of 16 ns (FWHM). The tau value was chosen to suppress the hydrogen matrix contribution; due to short phase memory times, tau values were restricted to less than 200ns. An integration window of 24 ns was used to acquire spin echo amplitude, and data set lengths were 512 points. The deuterium contributions to ESEEM spectra were elucidated using the ratio method introduced by Mims<sup>26</sup> together with processing tools provided by Bruker. Three-pulse ESEEM data were normalized by dividing each data set by its maximum amplitude.  $^2\text{H}$ -ESEEM data were then divided by the corresponding, normalized  $^1\text{H}$  ESEEM data, resulting in ESEEM data dominated by  $^2\text{H}$ . The time domain data that resulted from these ratios were tapered with a Hamming window function and Fourier transformed. ESEEM spectra were obtained by taking the absolute value of the transforms.

Simulations of the  $^2\text{H}$  hyperfine couplings were accomplished using scripts written in MATLAB. The calculations were performed in the time domain using the density matrix formalism of Mims.<sup>27</sup> The orientation-dependent Hamiltonian used was

modeled after work by Hutchison and McKay.<sup>28</sup> Processing of the simulations, also performed in Matlab, was identical to that described above for the experimental spectra.

### 3.3 RESULTS

In the previous chapter, to study the effects of substrate and cosubstrate binding on the structure of the TyrH Fe site, x-band CW-EPR spectra were examined of four derivatives of  $\{\text{FeNO}\}^7$  TyrH: TyrH treated with 6-methyltetrahydropterin, TyrH[6MPH<sub>4</sub>], TyrH treated with L-tyrosine, TyrH[tyr], TyrH treated with L-tyrosine and 6-methyltetrahydropterin, TyrH[tyr,6MPH<sub>4</sub>] and the TyrH mutant E332A treated with L-tyrosine and 6-methyltetrahydropterin, E332A[tyr,6MPH<sub>4</sub>]. Changes in the spectra were observed; however, no specific structural information, in regards to the substrates, could be obtained from the CW-EPR spectra.

To measure the structural relationship between substrate L-tyrosine, cosubstrate tetrahydrobiopterin and Fe(II) at the catalytic site ESEEM experiments were undertaken. ESEEM data from  $\{\text{FeNO}\}^7$  TyrH include hyperfine interactions from all nearby magnetic nuclei, including the nitrogens from the ligand histidines and hydrogens from nearby solvent and ligands. To isolate interactions due to L-tyr or 6MPH<sub>4</sub>, these cosubstrates were selectively deuterated, and the ESEEM data from the deuterated samples were divided by that for the corresponding protonated samples. For this procedure the time domain ESEEM data were normalized to the amplitude at the earliest time point and then divided, leaving predominately the deuterium ESEEM contribution.

To define the geometry of these deuterium hyperfine interactions, ESEEM experiments were performed at multiple field positions across the EPR spectrum. When

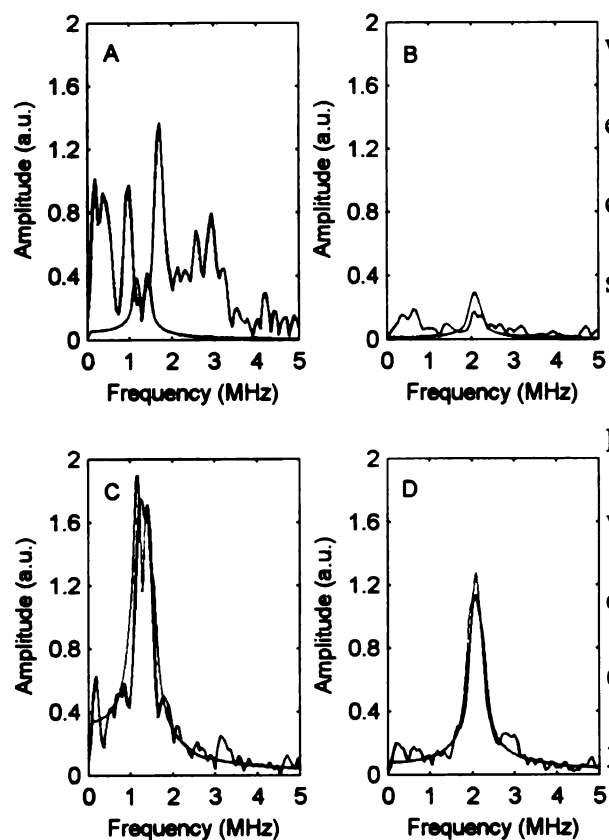


Figure 3.3: Representative  $^2\text{H}$  ESEEM of  $\{\text{FeNO}\}^7$  TyrH: treated with  $\text{d-6MPH}_4$  (A) at 1980G and (B) at 3200G; and treated with  $\text{d-6MPH}_4$  and tyr (C) at 1980G and (D) at 3200G. Experiment shown in black with the corresponding simulation shown in red. The Hamiltonian parameters used in the simulation of TyrH[ $\text{d-6MPH}_4$ ] were as follows: principle  $g$  values, 4.0, 4.0 and 2.0; principle deuterium hyperfine values, -0.06, -0.06, and 0.12 MHz; Euler angles for the hyperfine tensor 0, 1, and 0 radians;  $e^2qQ$ , 0.20 MHz;  $\eta$ , 0; Euler angles relating  $nq_i$  to  $hfi$ , 0, 1, and 0 radians. The Hamiltonian parameters used in the simulation of TyrH[ $\text{d-6MPH}_4$ , tyr] were as follows: principle  $g$  values, 4.0, 4.0 and 2.0; principle deuterium hyperfine values, -0.16, -0.16, and 0.32 Mhz; Euler angles for the hyperfine tensor 0, 1.15, and 0 radians;  $e^2qQ$ , 0.20 MHz;  $\eta$ , 0; Euler angles relating  $nq_i$  to  $hfi$ , 0, 0.75, and 0 radians.

working at discrete field positions, this effective  $g$ -anisotropy provides a single crystal-like selection of orientations that satisfy the resonance condition. {Hutchison, 1977 #25} <sup>18 19 29</sup> For the most part, the  $^2\text{H}$ -ESEEM peaks observed in the samples were weak and consisted of only single peaks centered at the  $^2\text{H}$ -Larmor frequency. Consequently, only spectra taken near  $g = 2$ , 3200 G, and near  $g = 4$ , 1980 G, will be presented.

Figures 3.3a and 3.3b show the  $^2\text{H}$ -ESEEM spectra of  $\{\text{Fe-NO}\}^7$  TyrH prepared with deuterated 6- $\text{CH}_3$ -6,7- $^2\text{H}$ -tetrahydropterin, TyrH[ $\text{d-6MPH}_4$ ], at 1980 G and 3200 G, respectively. The deuterium Larmor frequencies at these two magnetic field strengths are 1.3 and 2.1 MHz. The quotient spectrum at 1980 G (Figure 3.3a) is characterized by a signal-to-noise ratio of about 2, but shows peaks at 1.0 and 1.8 MHz. These peaks are observed in the

corresponding ESEEM spectrum of the protiated sample prior to division and are assigned to  $^{14}\text{N}$  contributions that have not been eliminated by the division procedure. No ESEEM intensity is resolved at 1.3 MHz. At 3200 G (Figure 3.3b) the overall modulation intensity is lower and the division process does a more complete job of eliminating ESEEM components that are common to both the TyrH[d-6MPH<sub>4</sub>] and TyrH[6MPH<sub>4</sub>] samples. Little or no ESEEM was detected at 2.1 MHz. The  $^2\text{H}$  ESEEM spectra of  $\{\text{Fe-NO}\}^7$  TyrH treated with both d-6MPH<sub>4</sub> and L-tyrosine, TyrH[d-6MPH<sub>4</sub>,tyr], are shown in Figures 3.3c and 3.3d. Unlike the TyrH[d-6MPH<sub>4</sub>]/TyrH[6MPH<sub>4</sub>] quotient spectra, the TyrH[d-6MPH<sub>4</sub>,tyr]/TyrH[6MPH<sub>4</sub>,tyr] quotients show resolved peaks centered at the deuterium Larmor frequency of 1.3 (1980 G) and 2.1 MHz (3200 G), respectively.

The red traces of Figure 3.3 show the results of  $^2\text{H}$ -ESEEM simulations for our studies of d-6MPH<sub>4</sub> coupling to the  $\{\text{FeNO}\}^7$  paramagnetic center. When L-tyr is bound to the enzyme, figures 3.3c and 3.3d, our simulations were done assuming a single  $^2\text{H}$  was coupled to the  $\{\text{FeNO}\}^7$  center with a dipole-dipole distance of  $4.2 \pm 0.2$  Å and an angle between the principal axis of the hyperfine interaction and the  $g_z$  axis of  $66 \pm 5^\circ$ . We also used simulations to gauge the change in dipolar distance that must occur to reduce the  $^2\text{H}$ -ESEEM to the levels observed for Figures 3.3a and 3.3b when d-6MPH<sub>4</sub> was present without L-tyr. The red traces in these figures were obtained by increasing the dipolar distance to 5.9 Å. The other parameters used in our calculations are given in the figure caption.

Figures 3.4a and 3.4b show the  $^2\text{H}$ -ESEEM of  $\{\text{Fe-NO}\}^7$  TyrH treated with 3,5-

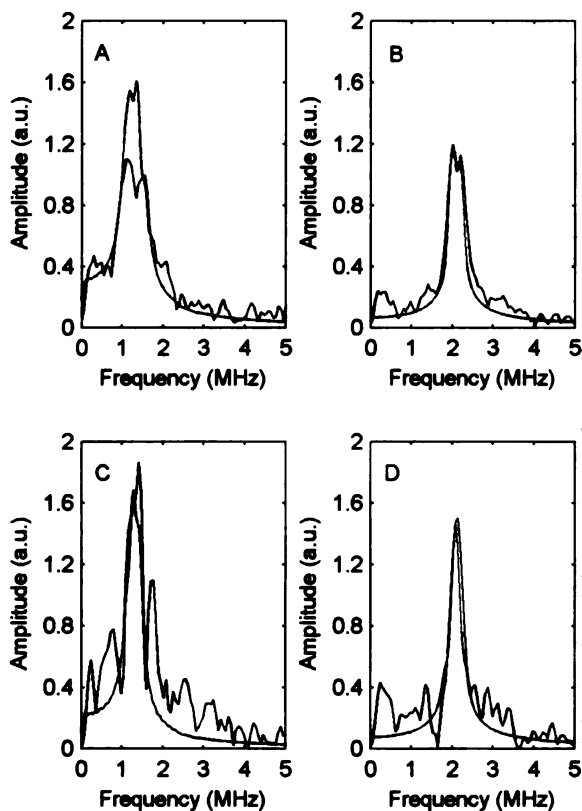


Figure 3.4: Representative  $^2\text{H}$  ESEEM of  $\{\text{FeNO}\}^7$  TyrH: treated with d-tyr (A) at 1980G and (B) at 3200G; and treated with 6MPH<sub>4</sub> and d-tyr (C) at 1980G and (D) at 3200G. Experiment shown in black with the corresponding simulation shown in red. The hamiltonian parameters used in the simulation of TyrH[d-tyr] were as follows: principle g values, 4.0, 4.0 and 2.0; principle deuterium hyperfine values, -0.15, -0.15, and 0.30 MHz; Euler angles for the hyperfine tensor 0, 1.25, and 0 radians;  $e^2qQ$ , 0.20 MHz;  $\eta$ , 0; Euler angles relating  $nq_i$  to  $hfi$ , 0, 0.7, and 0 radians. The hamiltonian parameters used in the simulation of TyrH[6MPH<sub>4</sub>,d-tyr] were as follows: principle g values, 4.0, 4.0 and 2.0; principle deuterium hyperfine values, -0.17, -0.17, and 0.34 MHz; Euler angles for the hyperfine tensor 0, 0.45, and 0 radians;  $e^2qQ$ , 0.20 MHz;  $\eta$ , 0; Euler angles relating  $nq_i$  to  $hfi$ , 0, 1.35, and 0 radians.

$^2\text{H}$ -L-tyrosine, TyrH[d-tyr]. ESEEM peaks attributed to  $^2\text{H}$  are clearly resolved at 1.3 and 2.1 MHz at 1980 and 3200 G, respectively. Simulations of these spectra

(red traces) assuming a single, coupled deuteron yielded a dipolar distance of  $4.3 \pm$

$0.2 \text{ \AA}$  and an orientation of the hyperfine principal axis with respect to  $g_z$  of  $72 \pm 5^\circ$ .

When  $\{\text{Fe-NO}\}^7$  TyrH is treated with 6-MPH<sub>4</sub> and 3,5- $^2\text{H}$  tyrosine, TyrH[6MPH<sub>4</sub>,d-tyr], the  $^2\text{H}$ - ESEEM spectra, Figures 3.4c

and 3.4d, show a modest change in

amplitude as compared to the

corresponding TyrH[d-tyr] spectra shown

in Figures 3.4a and 3.4b. A more

significant change is observed in the line

shape of TyrH[6MPH<sub>4</sub>,d-tyr], which

narrows and shows a single peak compared

to the spectra of TyrH[d-tyr] at both 1980

and 3200 G. The red traces in Figures 3.4c

and 3.4d show the corresponding

simulations for TyrH[6MPH<sub>4</sub>,d-tyr] that

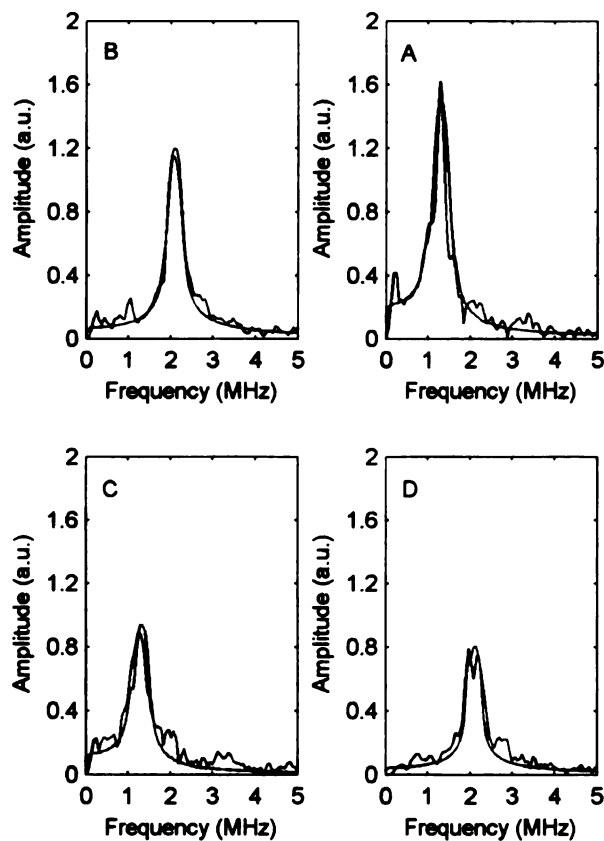


Figure 3.5: Representative  $^2\text{H}$  ESEEM of the  $\{\text{FeNO}\}^7$  TyrH mutant E332A: treated with d-6MPH<sub>4</sub> and tyr (A) at 1980G and (B) at 3200G; and treated with 6MPH<sub>4</sub> and d-tyr (C) at 1980G and (D) at 3200G. Experiment shown in black with the corresponding simulation shown in red. The Hamiltonian parameters used in the simulation of E332A[d-6MPH<sub>4</sub>,tyr] were as follows: principle g values, 4.0, 4.0 and 2.0; principle deuterium hyperfine values, -0.16, -0.16, and 0.32 MHz; Euler angles for the hyperfine tensor 0, 0.60, and 0 radians;  $e^2qQ$ , 0.20 MHz;  $\eta$ , 0; Euler angles relating  $nq_i$  to  $hfi$ , 0, 0.35, and 0 radians. The Hamiltonian parameters used in the simulation of E332A[6MPH<sub>4</sub>,d-tyr] were as follows: principle g values, 4.0, 4.0 and 2.0; principle deuterium hyperfine values, -0.13, -0.13, and 0.26 MHz; Euler angles for the hyperfine tensor 0, 0.45, and 0 radians;  $e^2qQ$ , 0.20 MHz;  $\eta$ , 0; Euler angles relating  $nq_i$  to  $hfi$ , 0, 0.65, and 0 radians.

result from changing the orientation between the PAS of the hyperfine tensor and  $g_z$  to  $25 \pm 5^\circ$  and decreasing the  $^2\text{H}$ -dipolar distance to  $4.1 \pm 0.2 \text{ \AA}$ .

Figures 3.5a and 3.5b show the  $^2\text{H}$ -ESEEM of the  $\{\text{Fe-NO}\}^7$  TyrH mutant E332A treated with deuterated 6-MPH<sub>4</sub> and tyrosine, E332A[d-6MPH<sub>4</sub>, tyr]. ESEEM peaks attributed to  $^2\text{H}$  are clearly resolved at 1.3 and 2.1 MHz at 1980 and 3200 G, respectively. Simulations of these spectra

(red traces) assuming a single, coupled deuteron yielded a dipolar distance of  $4.2 \pm 0.2 \text{ \AA}$  and an orientation of the hyperfine PAS with respect to  $g_z$  of  $34 \pm 5^\circ$ . The  $^2\text{H}$  ESEEM of the E332A mutant of  $\{\text{Fe-NO}\}^7$  TyrH treated with 6-MPH<sub>4</sub> and 3,5- $^2\text{H}$ -L-tyrosine, E332A[6MPH<sub>4</sub>,d-tyr], is shown in Figures 3.5c and 3.5d with clearly resolved  $^2\text{H}$  peaks. The red traces in Figures 3.5c and 3.5d show the corresponding simulations for TyrH[6MPH<sub>4</sub>,d-tyr] that

result from a single deuteron with an orientation between the PAS of the hyperfine tensor and  $g_z$  of  $25 \pm 5^\circ$  and a  $^2\text{H}$ -dipolar distance of  $4.5 \pm 0.2 \text{ \AA}$ .

### 3.4 $^2\text{H}$ ESEEM SIMULATION NOTES

$^2\text{H}$ -ESEEM simulations were undertaken to reveal the structural changes that occur upon substrate addition that underlie the experimental observations in Figures 3.3-3.5. The deuterium hyperfine couplings were modeled using the following spin

Hamiltonian:

$$\hat{H} = S_e \cdot A \cdot \hat{I} - g_n \beta_n H_0 \cdot \hat{I} + \hat{I} \cdot Q \cdot \hat{I} \quad [3.1]$$

which consists of the electron-nuclear hyperfine, nuclear Zeeman, and nuclear quadrupole interactions (nqi). Using the methodology of Hutchison and McKay<sup>28</sup> the spin Hamiltonian was set up in the principal axes system of the effective g-matrix with the effective g-values being used to account for the orientation selection as described previously, in chapter 2. Following previous  $^2\text{H}$ -ESEEM work on taurine dioxygenase<sup>20</sup>, the calculations assumed that the  $^2\text{H}$ -ligand hyperfine interaction could be modeled by a through-space, dipole-dipole interaction and that the nqi could be modeled with values of the nqi coupling constant,  $e^2qQ/h = 0.2 \text{ MHz}$ , and asymmetry parameter,  $\eta = 0$ .<sup>30</sup> The relative axial symmetry of the zerofield interaction, together with the axial symmetry assumed for the  $^2\text{H}$ -hyperfine interaction and  $^2\text{H}$ -nqi, resulted in the simulations being sensitive to just four parameters, the effective g-value of the measurement, the  $^2\text{H}$  dipolar distance, the Euler angle describing the relative orientation of the principal axis of the hyperfine interaction with the  $g_z = 2.00$  axis, and the Euler angle describing the relative orientation of the  $^2\text{H}$ -hyperfine and nqi principal axes.

In this scheme, the electron nuclear hyperfine couplings are weighted according to their orientation with respect to the g-tensor and the electron spin operator is weighted by the effective g-value of the measurement as can be seen in equations 2.10 and 2.4, respectively. In addition, when working at a fixed magnetic field position only a restricted set of orientations will satisfy the resonance condition of equation 2.5. The resulting single crystal-like spectra makes it necessary to examine multiple field positions to establish the orientation of the hyperfine tensor with respect to  $g_z$  axis.

In general, the  $^2\text{H}$  ESEEM examined in this work consisted of a single featureless peak at the  $^2\text{H}$  Larmour frequency, a result consistent with a weak hyperfine interaction. The relatively featureless lineshape of the ESEEM makes it necessary to consider the amplitude of the  $^2\text{H}$  peaks which are proportional to the magnitude of the hyperfine

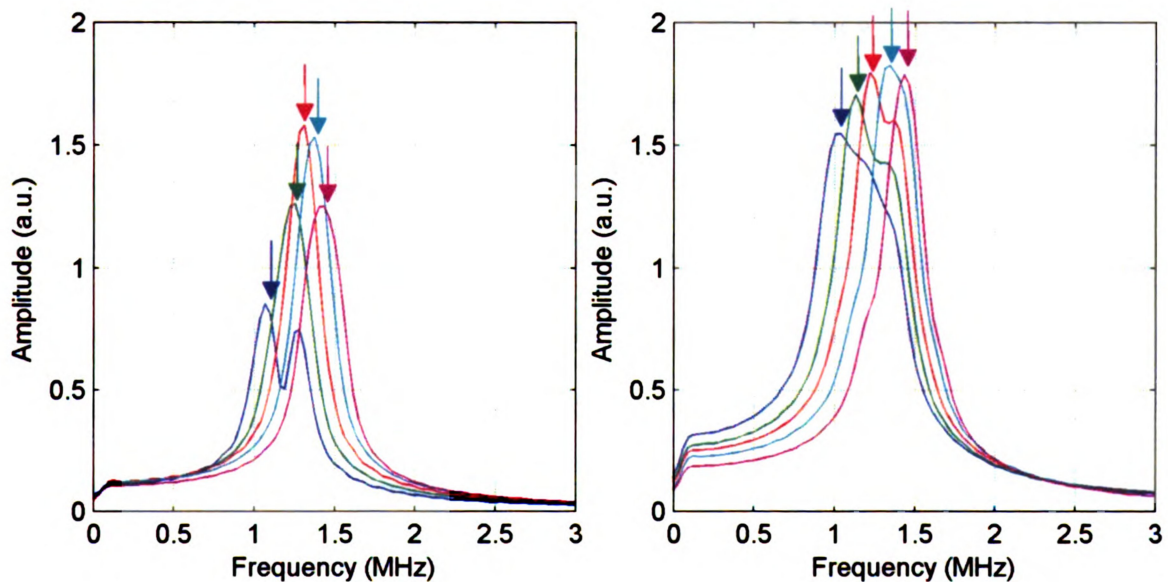


Figure 3.6:  $^2\text{H}$  simulations at 1780 G(blue), 1880 G(green), 1980 G(red), 2080 G(teal), 2180 G(purple) using a dipole distance of 4.5Å and an angle between the dipole vector and  $g_z$  of 0.3 rad. Figure 3.7:  $^2\text{H}$  simulations at 1780 G(blue), 1880 G(green), 1980 G(red), 2080 G(teal), 2180 G(purple) using a dipole distance of 4.5Å and an angle between the dipole vector and  $g_z$  of 1.3 rad.

interaction. With an increase in the dipolar coupling the amplitude also increases, this is related to a greater mixing of the nuclear spin sub-levels which increase the transition probabilities. Due to the weighting of the hyperfine interaction by the g-matrix the amplitudes are also a function of the orientation between the PAS of the hyperfine tensor and  $g_z$ . Based on the single crystal-like character of the spectra they also show a field dependent change in amplitude, this effect can be used to “fingerprint” the experimental data because the field dependent amplitude changes are dependent on the angle between the PAS of the hyperfine tensor and  $g_z$ . These amplitude changes as a function of orientation and field are only observed in the low field end of the spectrum  $g_{\text{eff}} < \sim 3$ . An example of this field dependence is shown in figures 3.6 and 3.7 where two sets of simulations, which differ by orientation (simulation parameters in the caption), are shown at multiple field positions between  $g = 4$  and  $g = 3$ . Figure 3.6 shows an angle 0.3 rad between the principle axis of the hyperfine tensor and  $g_z$  axis, it can be seen that the amplitude has a minimum at the low field end (1780 G –  $g = 3.881$ ) shows a maximum at 1980 G ( $g = 3.489$ ) and then begins to dip again. Figure 3.7, with an angle of 1.3 rad between the principle axis of the hyperfine tensor and  $g_z$  axis, shows different field dependent behavior, in addition to an overall greater amplitude, the relative amplitude difference between field positions is smaller than seen in figure 3.6.

The quadrupole interaction which represents the interaction of the  $^2\text{H}$  nucleus with the electric field gradient produced by the electron in its  $\sigma$ -bond to the C and is characterized by a principle axis which lies along the  $^2\text{H-C}$  bond. This interaction is axial and therefore the orientation between the principle axis of the quadrupole and the

principle axis of the hyperfine is described using a single Euler angle. In practice it was found that this angle largely influences the lineshape and was generally adjusted until satisfying spectra at multiple field positions were obtained. The relative certainty and confidence in these values were low, an unavoidable problem which can be attributed to the frequency resolution. A more accurate determination of the nuclear quadrupole interaction might be realized by working at higher fields, where the nuclear Zeeman interaction is of sufficient magnitude to separate the spin manifolds so that the individual components could be measured.

### **3.5 DISCUSSION**

While the present understanding of the mechanisms of the aromatic amino acid hydroxylases is based mainly on studies of TyrH, direct evidence for structural changes accompanying substrate binding to an aromatic amino acid hydroxylase comes from a limited number of structures of truncated PheH. These show significant differences between the ferrous PheH-tetrahydrobiopterin complex and the ferrous PheH-tetrahydrobiopterin-amino acid complex, including movement of loops over the active site and a change in the metal ligands.<sup>4</sup> There is evidence that the effect of substrate binding differs between TyrH and PheH. The structures of PheH show that the active site loop containing Tyr138 closing down on the active site only in the ternary complex. In contrast, solution studies of TyrH show that the comparable loop in that enzyme responds to pterin binding and is unaffected by binding of the amino acid substrate.<sup>10</sup> Moreover, even the structures of the ferrous PheH ternary complexes do not establish the orientation of the substrates in the reactive complex containing amino acid, pterin, and oxygen. The

data reported in the present work establish the relative orientations of the pterin and the amino acid in the active site of TyrH and the changes accompanying binding of each substrate. In addition, the use of NO as an O<sub>2</sub> mimic allows us to model the active quaternary complex.

The results of the ESEEM studies on TyrH are summarized in Tables 1, these results are given in terms of their dipolar distance, an imaginary vector which connects the Fe to the deuteron; an angle,  $\theta_{\text{HFI}}$ , which represents the angle between the dipolar vector and the axis defined by the Fe-NO bond; and an angle,  $\theta_{\text{NQI}}$ , which is the angle that relates the principle axis system of the nuclear quadrupole interaction to that of the hyperfine interaction. In this work the nqi was held at a constant value of 0.2 MHz with

axial symmetry, where the principle axis of the nqi is along the C-<sup>2</sup>H bond. This approximation for the nqi allowed successful simulation of the data and falls in line with other studies in similar systems.<sup>18 19 20</sup> In the ESEEM simulations, the principal g values were held constant at [4,4,2] despite the experimental determination of the effective g

Table 3.1: Deuterium Hyperfine Coupling Parameters

	Distance(Å) <sup>a</sup> ± 0.2 Å	$\theta_{\text{HFI}}$ ± 5°	$\theta_{\text{NQI}}$ <sup>b</sup> ± 5°
TyrH[d-6MPH <sub>4</sub> ]	> 5.9	57°	57°
TyrH[tyr,d-6MPH <sub>4</sub> ]	4.2	65°	42°
TyrH[d-tyr]	4.3	71°	40°
TyrH[d-tyr,6MPH <sub>4</sub> ]	4.1	25°	77°
E332A[tyr,d-6MPH <sub>4</sub> ]	4.2	34°	20°
E332A[d-tyr,6MPH <sub>4</sub> ]	4.5	25°	37°

<sup>a</sup> Distance measured between the Fe and the <sup>2</sup>H using the point dipole approximation

<sup>b</sup> Quadrupole parameters held constant,  $e^2Qq = 0.2$ ,  $\eta=0$

values (chapter 1). Simulations were run using both the experimentally determined  $g$  values and the axial set [4,4,2]. This approximation has a negligible effect near  $g = 2$  and gives rise to less than a 10% increase in the amplitude (for  $E/D = 0.05$ ) near the  $g = 4$  extreme. Although the CW-EPR spectra of TyrH[tyr], TyrH[6MPH<sub>4</sub>,tyr] and E332A[6MPH<sub>4</sub>,tyr] are mixtures of two species, the  $E/D$  values for all species are  $< 0.05$  with the majority species having  $E/D < 0.02$ . Given the uncertainty in the ESEEM amplitude that arises at  $g = 4$  from the data processing, the assumption of an axial  $g$ -matrix is justified.

Multi-component CW-EPR spectra have been observed in both the ferric and ferrous nitrosyl forms of PheH and soybean lipoxygenase.<sup>31 32 33 34 35</sup> In chapter 1 we observed that the CW-EPR spectra of TyrH[tyr], TyrH[6MPH<sub>4</sub>,tyr] and E332A[6MPH<sub>4</sub>,tyr] is composed of a mixture of two slightly rhombic species. Based on the observation of a mixture in both ferrous and ferric PheH, it is reasonable to assume that the mixture we observe is independent of the orientation of the NO bond but instead reflects differences in the coordination environment of the {FeNO}<sup>7</sup>. The Fe center in TyrH is known to be coordinated by 2 histidines and a glutamate; the other coordinate sites are occupied by solvent and NO. It is possible that the two species observed in the CW-EPR are the result of freezing in different conformers of bound water or of capturing a mixture, either mono or bidentate, in the ligation of the glutamate side chain.

The results from the study with 6,7-<sup>2</sup>H-6MPH<sub>4</sub> show that in TyrH there is a decrease in the <sup>2</sup>H-Fe distance upon the addition of tyr. In TyrH[d-6MPH<sub>4</sub>] the <sup>2</sup>H ESEEM signal is not clearly resolved in our quotient spectra. Simulations indicate that

the closest  $^2\text{H}$ -Fe distance that can account for this “failed observation” is 5.9 Å. Our simulations assumed that only a single  $^2\text{H}$  of the two on d-6MPH<sub>4</sub> is interacting strongly enough with the Fe to produce ESEEM. This assumption is backed by crystal structures of TyrH and PheH that show the pterin oriented with C<sub>4a</sub> closest to the iron. This orientation of the pterin places the C<sub>6</sub>  $^2\text{H}$  at least 1 Å closer to the iron than the C<sub>7</sub>  $^2\text{H}$ . This difference in  $^2\text{H}$  distance would result in an ESEEM spectrum that is composed almost entirely of the coupling to the closer of the two deuterons. The distance between the Fe and the C<sub>6</sub>  $^2\text{H}$  determined by ESEEM agrees fairly well with the TyrH and PheH crystal structures that give Fe-C<sub>6</sub> distances of 6.5 Å and 7.3 Å, respectively.<sup>12 13</sup> This range of distances precludes direct binding of the pterin to the Fe and is consistent with the CW-EPR result (Figure 1.4a) that shows that pterin binding to TyrH by itself has little or no effect on the symmetry of the zero field interaction of the {FeNO}<sup>7</sup> center.

Upon tyr addition to TyrH[6MPH<sub>4</sub>], the  $^2\text{H}$ -Fe distance decreases to 4.2 Å, a change of at least 1.7 Å. This result agrees with changes observed in x-ray crystal structures of PheH, where the distance between the Fe and the C<sub>4</sub> position of pterin is reduced by approximately 1.5 Å when a substrate analog is bound (1kw0), as compared to the structure when just pterin is bound to the enzyme (1dmw).<sup>4, 13</sup> The orientation of the  $^2\text{H}$ -hyperfine principle axis suggests that the NO does not bind between the pterin and the Fe, but rather in a more axial position with respect to the plane formed by the Fe and pterin. These results fit with current ideas on how TyrH controls chemical reactivity to ensure efficient preparation of DOPA and minimize side reactions that could occur if the Fe(IV)=O species were generated in the absence of tyr. Specifically, the binding of tyr to

the TyrH{FeNO}<sup>7</sup> 6MPH<sub>4</sub> complex moves the pterin cosubstrate closer to the {FeNO}<sup>7</sup> and presumably into a position where the initial O<sub>2</sub>-pterin chemistry can occur.

The interaction of tyr with TyrH is considerably different than that of the pterin. The dipolar distance between 3,5-<sup>2</sup>H-tyr and the Fe center only changes a small amount with the addition of the other substrate, 6MPH<sub>4</sub>. The ESEEM simulation for d-tyr in TyrH assumed only one of the two deuterons contributes significantly to the ESEEM amplitude. This assumption is not backed by existing structural evidence as it was with the pterin. The assumption is made based on two experimental observations, the ESEEM amplitude and the CW-EPR spectrum, that when taken in concert suggest that tyr is rotated to bring one of the meta positions closer to the Fe with the other rotated away from the iron. The observed ESEEM amplitude is inversely related to the dipolar distance and directly related to the number of interacting nuclei. With two equivalent <sup>2</sup>H's, such as would be the case if the hydroxyl group of the tyr were symmetrically positioned toward the iron, the minimal dipolar distance required to reproduce the ESEEM amplitude would be ~5 Å. If the tyr is rotated, with one of the positions brought closer while the other is pushed away, the further of the two deuterons contributes an insignificant amount to the ESEEM once it reaches ~5.5 Å from the Fe. The ESEEM simulations were performed assuming a single deuteron and therefore represent the closest approach of tyr to the Fe. The CW EPR spectrum of TyrH[tyr](figure 1.4b) shows a shift away from the purely axial spectrum observed for TyrH[6MPH<sub>4</sub>]. This shows that tyr binding to TyrH has an effect on the symmetry of the {FeNO}<sup>7</sup> zero field interaction and is most consistent with the closer positioning of the C<sub>3</sub>-<sup>2</sup>H to the Fe. The range of <sup>2</sup>H-Fe distances for tyr in TyrH

corroborate what has been suggested by x-ray crystallographic studies of PheH and other data that indicate Fe does not directly coordinate the primary substrates.<sup>4, 11</sup>

The addition of 6MPH<sub>4</sub> to TyrH[d-tyr] only has a minor effect on the intensity of the <sup>2</sup>H modulations. Specifically the ESEEM amplitude increases by 18% at g = 2.2 which corresponds to a slight decrease in the <sup>2</sup>H-Fe distance from 4.3 Å in TyrH[d-tyr] to 4.1 Å in TyrH[6MPH<sub>4</sub>,d-tyr]. The more significant change to the ESEEM spectrum appears in the line shape. The splitting observed in TyrH[d-tyr] is no longer present when 6MPH<sub>4</sub> is added, consistent with a change in the orientation of the <sup>2</sup>H-Fe vector with respect to the Fe-NO bond. Based on the small change observed in the <sup>2</sup>H-Fe distance, it is reasonable to suggest that the position of substrate tyr with respect to the Fe and the relative orientation of the <sup>2</sup>H HFI and NQI principle axes remain the same with and without the pterin. The change in orientation observed would then correspond to a reorientation of the Fe-NO bond when the pterin is bound to TyrH. Our results are consistent with the NO moving from a roughly equatorial position to one that is more axial with respect to tyr. This change in relative orientation would facilitate the hydroxylation of tyr upon the formation of the Fe(IV)=O species.

Glu332 in TyrH is part of the pterin binding site in TyrH,<sup>22 23</sup> and the structure of PheH shows that the corresponding residue Glu286 forms hydrogen bonds with the pterin in that enzyme.<sup>4</sup> The E332A mutant shows several changes compared to the wild type enzyme with respect to the binding of 6MPH<sub>4</sub> and tyr. For E332A TyrH [d-6MPH<sub>4</sub>,tyr] the proximity of 6MPH<sub>4</sub> to the Fe compared to the wild-type protein is conserved at 4.2 Å. However, the orientation of the dipole-dipole vector with respect to the NO bond is

changed considerably, shifting from 65° to 34°, or from equatorial to more axial. On the other hand, studies of E332A[6MPH<sub>4</sub>,d-tyr] show that tyr maintains the same orientation seen in WT-TyrH[6MPH<sub>4</sub>,d-tyr], but with a longer Fe-<sup>2</sup>H distance of 4.5 Å. The CW EPR spectrum of E332A[6MPH<sub>4</sub>,tyr] is nearly identical to TyrH[6MPH<sub>4</sub>,tyr] suggesting that the first coordination sphere of the Fe changes very little as a result of the mutation.

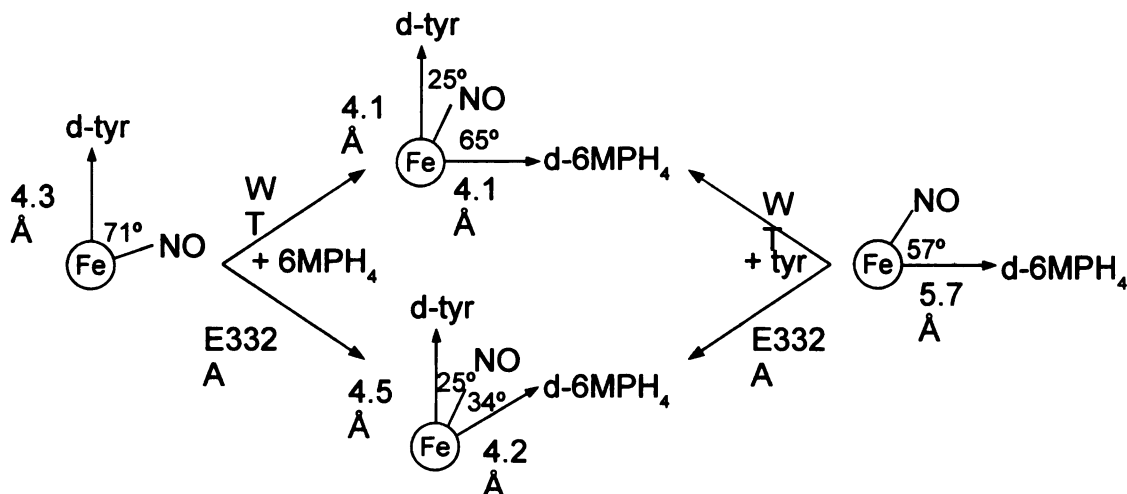


Figure 3.8: Summary of ESEEM Results

The structural relationships between the dipole-dipole vectors and the Fe-NO bond for the four cases we examined with <sup>2</sup>H ESEEM are summarized in figure 3.8. These dipole-dipole vectors in theory represent cones about the Fe-NO bond on which the substrate deuterons can be found. We cannot with certainty define the orientation of the NO in the enzyme; however, using the crystal structure of PheH with pterin and substrate analog as a model, it is very probable that the substrates lie opposite one another with respect to the Fe-NO bond. If NO is indeed mimicking O<sub>2</sub> binding, we can then use its structural relationship with the substrate deuterons to draw some conclusions about the mechanism of hydroxylation in TyrH. The formation of the initial Fe-OO-pterin has been

suggested to involve a concerted reaction of oxygen, the tetrahydropterin, and the iron.<sup>11</sup> The positioning of NO in TyrH[6MPH<sub>4</sub>,tyr] is appropriate for such a reaction. The Fe-O<sub>2</sub>-pterin intermediate then heterolytically cleaves when the oxygen atom distal to the Fe(II) is protonated, forming the Fe(IV)=O species.<sup>11</sup> The structural model in Scheme 3 would place the Fe(IV)O oxygen in close proximity to the tyrosine carbon that is hydroxylated.

For productive hydroxylation of their substrates, enzymes such as TyrH that utilize highly electrophilic Fe(IV)O intermediates must not only catalyze the formation of such an intermediate, but also suppress all unproductive reactions both before and after its formation. The TyrH mutant E332A, does not hydroxylate tyr but does produce an oxidized pterin species, possibly 4a-hydroperoxypterin.<sup>22 11</sup> The structural evidence obtained from the ESEEM measurements suggest that this uncoupled reaction is a consequence of the different pterin orientation in the mutant enzyme, resulting in a geometrically altered Fe-O<sub>2</sub>-pterin activated complex. This altered orientation results in cleavage of the oxygen-iron bond instead of the oxygen-oxygen bond, preventing formation of the Fe(IV)O intermediate. The previous suggestion that this is due to protonation of the distal rather than the proximal oxygen<sup>11</sup> is fully consistent with the present results. In addition, the altered position of the pterin may weaken the oxygen-iron bond, facilitating its cleavage.

### **3.5 CONCLUSIONS**

The present results for the first time establish the relative positions of the three substrates, tetrahydropterin, tyrosine, and oxygen, in the active site of an aromatic amino acid hydroxylase. The resulting structural details extend the understanding of the

mechanisms of these enzymes.

### 3.6 REFERENCES

1. Haavik, J.; Flatmark, T., Isolation and Characterization of Tetrahydropterin Oxidation Products Generated in the Tyrosine 3-Monooxygenase (Tyrosine Hydroxylase) Reaction. *European Journal of Biochemistry* **1987**, *168* (1), 21-6.
2. Fitzpatrick, P. F., Mechanism of Aromatic Amino Acid Hydroxylation. *Biochemistry-U.S.* **2003**, *42* (48), 14083-14091.
3. Goodwill, K. E.; Sabatier, C.; Marks, C.; Raag, R.; Fitzpatrick, P. F.; Stevens, R. C., Crystal Structure of Tyrosine Hydroxylase at 2.3 Angstrom and Its Implications for Inherited Neurodegenerative Diseases. *Nat Struct Biol* **1997**, *4* (7), 578-585.
4. Andersen, O. A.; Flatmark, T.; Hough, E., Crystal Structure of the Ternary Complex of the Catalytic Domain of Human Phenylalanine Hydroxylase with Tetrahydrobiopterin and 3-(2-Thienyl)-L-Alanine, and Its Implications for the Mechanism of Catalysis and Substrate Activation. *J Mol Biol* **2002**, *320* (5), 1095-1108.
5. Windahl, M. S.; Petersen, C. R.; Christensen, H. E. M.; Harris, P., Crystal Structure of Tryptophan Hydroxylase with Bound Amino Acid Substrate. *Biochemistry-U.S.* **2008**, *47* (46), 12087-12094.
6. Eser, B. E.; Barr, E. W.; Frantorn, P. A.; Saleh, L.; Bollinger, J. M.; Krebs, C.; Fitzpatrick, P. F., Direct Spectroscopic Evidence for a High-Spin Fe(IV) Intermediate in Tyrosine Hydroxylase. *J Am Chem Soc* **2007**, *129* (37), 11334-+.
7. Eser, B. E.; Fitzpatrick, P. F., Measurement of Intrinsic Rate Constants in the Tyrosine Hydroxylase Reaction. *Biochemistry-U.S.* **2010**, *49* (3), 645-652.
8. Hillas, P. J.; Fitzpatrick, P. F., A Mechanism for Hydroxylation by Tyrosine Hydroxylase Based on Partitioning of Substituted Phenylalanines. *Biochemistry-U.S.* **1996**, *35* (22), 6969-6975.
9. Fitzpatrick, P. F., Steady-State Kinetic Mechanism of Rat Tyrosine-Hydroxylase. *Biochemistry-U.S.* **1991**, *30* (15), 3658-3662.
10. Sura, G. R.; Lasagna, M.; Gawandi, V.; Reinhart, G. D.; Fitzpatrick, P. F., Effects of Ligands on the Mobility of an Active-Site Loop in Tyrosine Hydroxylase as Monitored by Fluorescence Anisotropy. *Biochemistry-U.S.* **2006**, *45* (31), 9632-9638.
11. Chow, M. S.; Eser, B. E.; Wilson, S. A.; Hodgson, K. O.; Hedman, B.; Fitzpatrick, P. F.; Solomon, E. I., Spectroscopy and Kinetics of Wild-Type and Mutant Tyrosine Hydroxylase: Mechanistic Insight into O<sub>2</sub> Activation. *J Am Chem Soc* **2009**, *131* (22), 7685-7698.
12. Goodwill, K. E.; Sabatier, C.; Stevens, R. C., Crystal Structure of Tyrosine Hydroxylase with Bound Cofactor Analogue and Iron at 2.3 Angstrom Resolution: Self-

Hydroxylation of Phe300 and the Pterin-Binding Site. *Biochemistry-U*s **1998**, *37* (39), 13437-13445.

13. Erlandsen, H.; Bjorgo, E.; Flatmark, T.; Stevens, R. C., Crystal Structure and Site-Specific Mutagenesis of Pterin-Bound Human Phenylalanine Hydroxylase. *Biochemistry-U*s **2000**, *39* (9), 2208-2217.

14. Andersen, O. A.; Stokka, A. J.; Flatmark, T.; Hough, E., 2.0 Angstrom Resolution Crystal Structures of the Ternary Complexes of Human Phenylalanine Hydroxylase Catalytic Domain with Tetrahydrobiopterin and 3-(2-Thienyl)-L-Alanine or L-Norleucine: Substrate Specificity and Molecular Motions Related to Substrate Binding. *J Mol Biol* **2003**, *333* (4), 747-757.

15. Rich, P. R.; Salerno, J. C.; Leigh, J. S.; Bonner, W. D., Spin 3-2 Ferrous-Nitric Oxide Derivative of an Iron-Containing Moiety Associated with Neurospora-Crassa and Higher Plant-Mitochondria. *Febs Lett* **1978**, *93* (2), 323-326.

16. Arciero, D. M.; Lipscomb, J. D.; Huynh, B. H.; Kent, T. A.; Munck, E., Electron-Paramagnetic-Res and Mossbauer Studies of Protocatechuate 4,5-Dioxygenase - Characterization of a New Fe-2+ Environment. *J Biol Chem* **1983**, *258* (24), 4981-4991.

17. Brown, C. A.; Pavlosky, M. A.; Westre, T. E.; Zhang, Y.; Hedman, B.; Hodgson, K. O.; Solomon, E. I., Spectroscopic and Theoretical Description of the Electronic-Structure of S=3/2 Iron-Nitrosyl Complexes and Their Relation to O-2 Activation by Nonheme Iron Enzyme Active-Sites. *J Am Chem Soc* **1995**, *117* (2), 715-732.

18. Yang, T. C.; Wolfe, M. D.; Neibergall, M. B.; Mekmouche, Y.; Lipscomb, J. D.; Hoffman, B. M., Substrate Binding to Non-Ferrous-Naphthalene 1,2-Dioxygenase Studied by High-Resolution Q-Band Pulsed H-2-Endor Spectroscopy. *J Am Chem Soc* **2003**, *125* (23), 7056-7066.

19. Tierney, D. L.; Rocklin, A. M.; Lipscomb, J. D.; Que, L.; Hoffman, B. M., Endor Studies of the Ligation and Structure of the Non-Heme Iron Site in Acc Oxidase. *J Am Chem Soc* **2005**, *127* (19), 7005-7013.

20. Muthukumar, R. B.; Grzyska, P. K.; Hausinger, R. P.; McCracken, J., Probing the Iron-Substrate Orientation for Taurine/Alpha-Ketoglutarate Dioxygenase Using Deuterium Electron Spin Echo Envelope Modulation Spectroscopy. *Biochemistry-U*s **2007**, *46* (20), 5951-5959.

21. Fitzpatrick, P. F., The Ph-Dependence of Binding of Inhibitors to Bovine Adrenal Tyrosine-Hydroxylase. *J Biol Chem* **1988**, *263* (31), 16058-16062.

22. Frantom, P. A.; Seravalli, J.; Ragsdale, S. W.; Fitzpatrick, P. F., Reduction and Oxidation of the Active Site Iron in Tyrosine Hydroxylase: Kinetics and Specificity. *Biochemistry-U*s **2006**, *45* (7), 2372-2379.

23. Daubner, S. C.; Fitzpatrick, P. F., Site-Directed Mutants of Charged Residues in the Active Site of Tyrosine Hydroxylase. *Biochemistry-Us* **1999**, *38* (14), 4448-4454.
24. Ramsey, A. J.; Hillas, P. J.; Fitzpatrick, P. F., Characterization of the Active Site Iron in Tyrosine Hydroxylase - Redox States of the Iron. *J Biol Chem* **1996**, *271* (40), 24395-24400.
25. Keefer, L. K.; Nims, R. W.; Davies, K. M.; Wink, D. A., "Nonoates" (1-Substituted Diazen-1-ium-1,2-Diolates) as Nitric Oxide Donors: Convenient Nitric Oxide Dosage Forms. *Method Enzymol* **1996**, *268*, 281-293.
26. Mims, W. B.; Davis, J. L.; Peisach, J., The Accessibility of Type-I Cu(II) Centers in Laccase, Azurin, and Stellacyanin to Exchangeable Hydrogen and Ambient Water. *Biophys J* **1984**, *45* (4), 755-766.
27. Mims, W. B., Envelope Modulation in Spin-Echo Experiments. *Phys Rev B* **1972**, *5* (7), 2409-&.
28. Hutchison, C. A.; McKay, D. B., Determination of Hydrogen Coordinates in Lanthanum Nicotinate Dihydrate Crystals by Nd<sup>3+</sup>-Proton Double-Resonance. *J Chem Phys* **1977**, *66* (8), 3311-3330.
29. Hurst, G. C.; Henderson, T. A.; Kreilick, R. W., Angle-Selected EPR Spectroscopy .1. Theoretical Interpretation of EPR Shifts from Randomly Orientated Transition-Metal Complexes. *J Am Chem Soc* **1985**, *107* (25), 7294-7299.
30. Edmonds, D. T., Nuclear-Quadrupole Double-Resonance. *Phys Rep* **1977**, *29* (4), 234-290.
31. Bloom, L. M.; Benkovic, S. J.; Gaffney, B. J., Characterization of Phenylalanine-Hydroxylase. *Biochemistry-Us* **1986**, *25* (15), 4204-4210.
32. Kappock, T. J.; Harkins, P. C.; Friedenber, S.; Caradonna, J. P., Spectroscopic and Kinetic Properties of Unphosphorylated Rat Hepatic Phenylalanine Hydroxylase Expressed in Escherichia Coli - Comparison of Resting and Activated States. *J Biol Chem* **1995**, *270* (51), 30532-30544.
33. Han, A. Y.; Lee, A. Q.; Abu-Omar, M. M., EPR and UV-Vis Studies of the Nitric Oxide Adducts of Bacterial Phenylalanine Hydroxylase: Effects of Cofactor and Substrate on the Iron Environment. *Inorg Chem* **2006**, *45* (10), 4277-4283.
34. Wallick, D. E.; Bloom, L. M.; Gaffney, B. J.; Benkovic, S. J., Reductive Activation of Phenylalanine-Hydroxylase and Its Effect on the Redox State of the Non-Heme Iron. *Biochemistry-Us* **1984**, *23* (6), 1295-1302.
35. Salerno, J. C.; Siedow, J. N., Nature of the Nitric-Oxide Complexes of Lipoxigenase. *Biochim Biophys Acta* **1979**, *579* (1), 246-251.

## CHAPTER IV

### HYSCORE CHARACTERIZATION OF TYROSINE HYDROXYLASE AND PHENYLALANINE HYDROXYLASE

#### 4.1 INTRODUCTION

This chapter is a collection of results and discussions from TyrH and PheH. These are interesting results that are worth noting but they don't stand on their own like the results presented in the previous chapters. Attempts were made to collect HYSCORE spectra on the binary, ternary and quaternary complexes of both enzymes; however, only the quaternary complexes provided suitable crosspeaks that allowed for analysis. These HYSCORE results of the quaternary complex of PheH and TyrH will be presented accompanied by analysis of the exchangeable hydrogen and non-exchangeable hydrogen. In addition, the preliminary analysis of  $^2\text{H}$  ESEEM collected on PheH treated with selectively deuterated substrates will be presented.

#### 4.2 HYSCORE RESULTS

In chapter 2, we characterized the HYSCORE spectrum of a non-heme  $\{\text{FeNO}\}^7$  model system. We provided the identification of the features we could expect to observe in the HYSCORE spectra of non-heme iron enzymes which included directly coordinated nitrogen, solvent molecules and non-exchangeable hydrogen. These results will provide a guide to help understand HYSCORE spectra collected on TyrH and PheH. Similar to the model system, HYSCORE spectra were acquired at multiple field positions from  $g = 4$  to  $g = 2$  and utilized in the analysis; however, only representative spectra at 1980 G ( $g = 3.489$ ) and 3100 G ( $g = 2.229$ ) will be shown.

Shown in figures 4.1 and 4.2 are the HYSORE spectra of the TyrH quaternary complex acquired at 1980 G and 3100 G, respectively. In the (++) quadrant of both spectra, we observe features in the region expected for hydrogen. At 1980 G, two sets of hydrogen features are observed, one set with a maximum at (5.9,12.2) MHz and a second

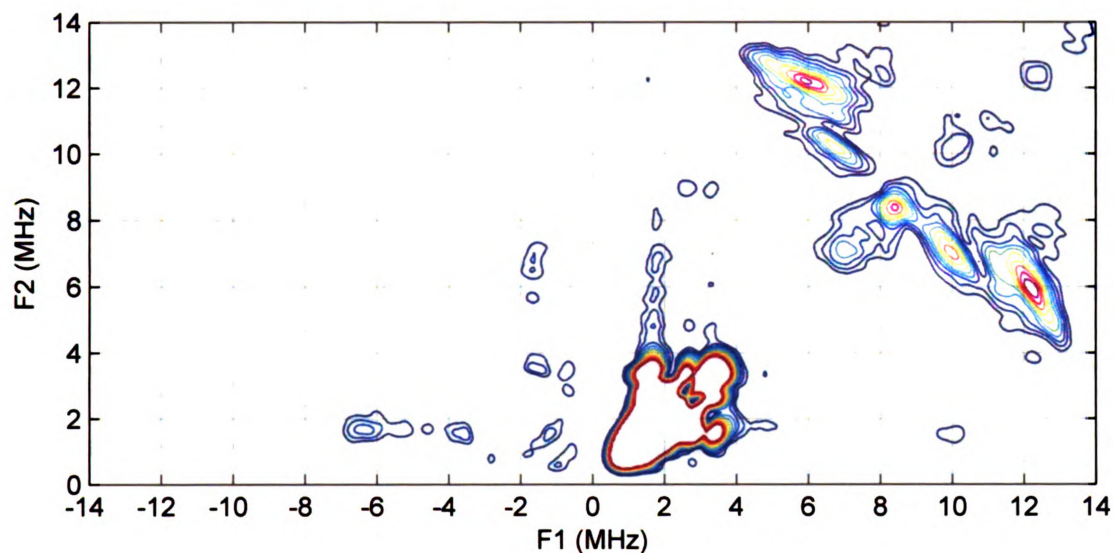


Figure 4.1: HYSORE spectrum of TyrH[6MPH<sub>4</sub>,tyr] at 1980 G

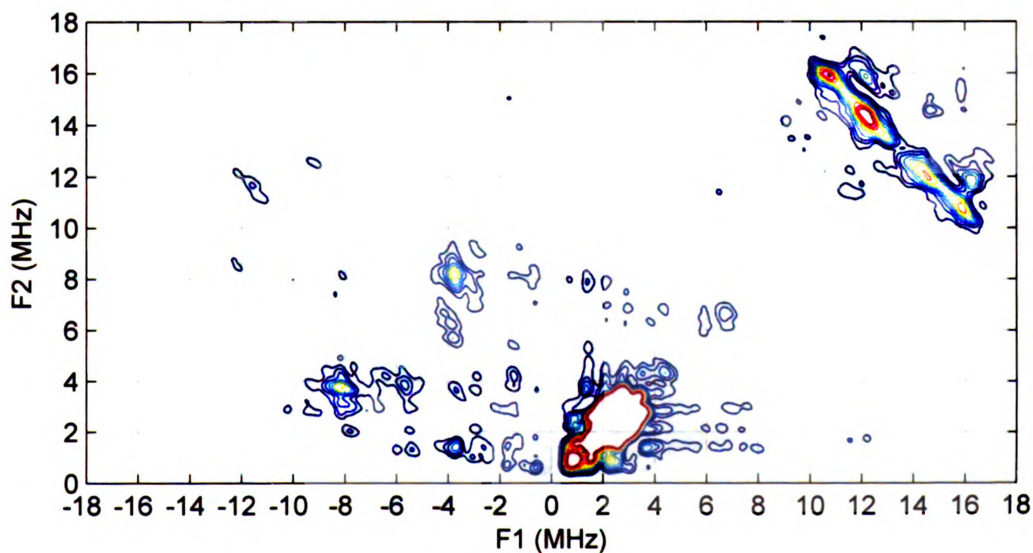


Figure 4.2: HYSORE spectrum of TyrH[6MPH<sub>4</sub>,tyr] at 3100G

set with a maximum at (6.8,10.2) MHz. With an increase of the magnetic field to 3100 G, the two sets of hydrogen features are observed to now have maxima at (12.1,14.4) MHz and (10.7,15.95) MHz, in addition, there is a new higher frequency peak at (12,16) MHz. At 3100 G in the (-+) quadrant the directly coordinated nitrogen is observed with a peak at (-3.8,8.1) MHz. In addition to the expected HYSORE features, a new group of features, not observed in the model, can be seen in the range from 0 – 4 MHz at both field positions. The resolution of these features is largely obscured by broad intense features along the diagonal.

Shown in figure 4.3 and 4.4 are the HYSORE spectra acquired on the quaternary complex of PheH at 1980 G and 3100 G, respectively. These two spectra show features similar to those observed in the HYSORE spectra of TyrH. At 1980 G, the (++) quadrant has two sets of hydrogen features, one set with a maximum at (6.2,12) MHz and the second set with a maximum at (6.8,10.1) MHz. At 3100 G, the two sets of hydrogen

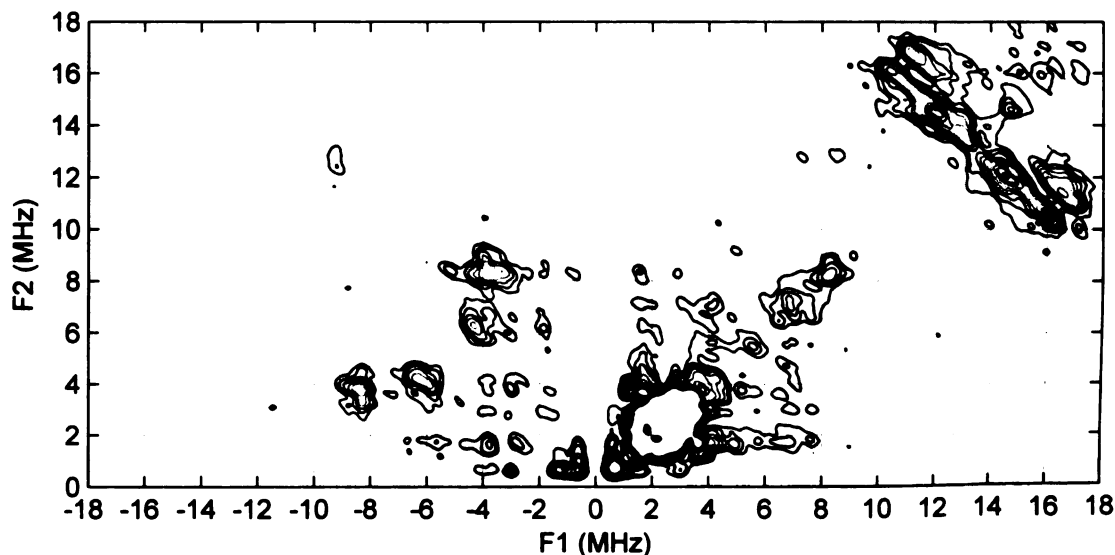


Figure 4.3: HYSORE spectrum of PheH[Phe, 5d] at 1980 G

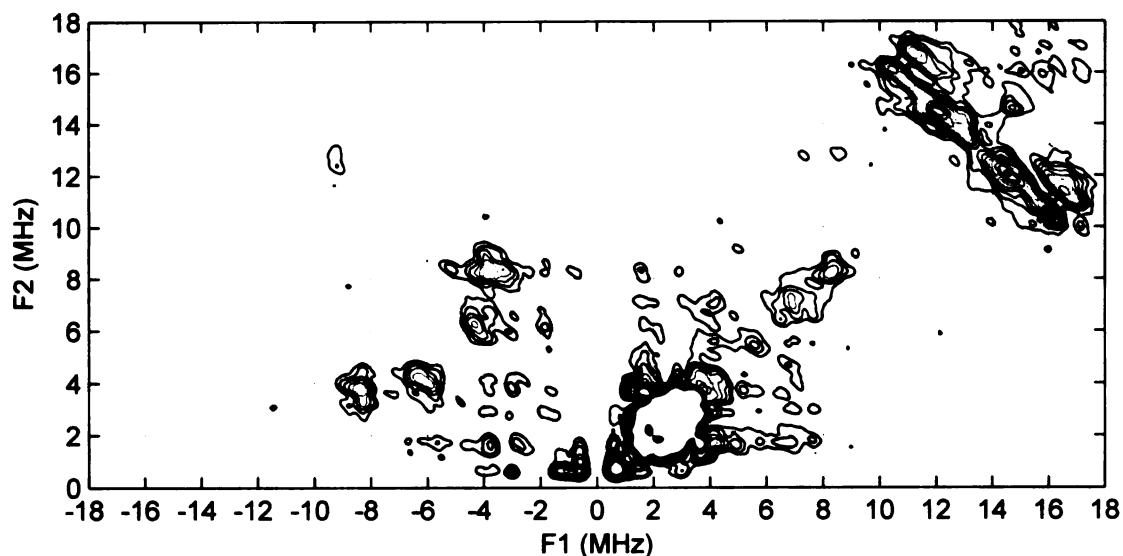


Figure 4.4: HYSORE spectrum of PheH[Phe, 5d] at 3100G

features are observed to now have maxima at (12,14.6) MHz and (10.5,16.1) MHz, in addition, there is a new higher frequency peak at (11.2,16.8) MHz. A strongly coupled nitrogen feature is also observed in the (-+) quadrant with a maximum at (-3.8,8.3) and a second maximum at (-4.3,6.2). Again, features consistent with weakly coupled nitrogen can be seen from 0-4 MHz and the resolution of these features is largely obscured by an intense feature along the diagonal.

### 4.3 HISTIDINE HYPERFINE COUPLING ANALYSIS

As noted previously, the Fe center in TyrH and PheH is facially coordinated by two histidine ligands and a glutamate. Further examination of the crystal structure<sup>1</sup> suggests that the histidine ligands provide the only enzyme based magnetic nuclei within  $\sim 4.5$  Å. Each histidine provides a directly coordinated nitrogen, a remote nitrogen  $\sim 4.4$  Å from the iron and two non-exchangeable hydrogens on the 2 and 5 positions which are  $\sim 3.2$  Å from the iron. Based on the work in chapter 2, it is possible to immediately assign

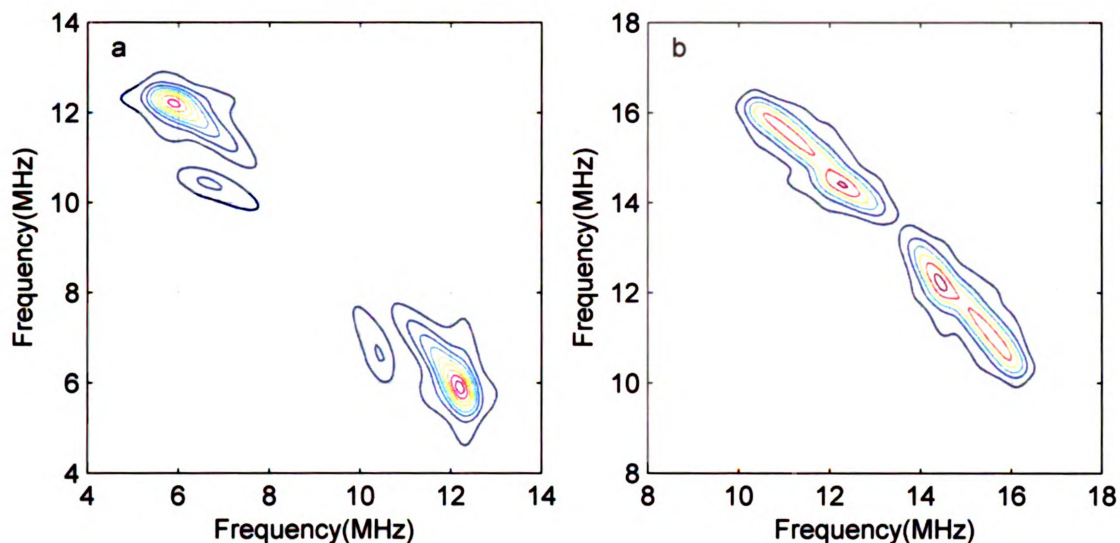


Figure 4.5:  $^1\text{H}$  HYSCORE simulations for TyrH at 1980 G (a) and 3100 G (b).

the features attributed to the directly coordinated nitrogen and the hydrogen. Through a process of elimination, it is reasonable to assume that the hyperfine frequencies observed in the 0 – 4 MHz range represent the remote nitrogen; however, due to the poor resolution it cannot be characterized.

Shown in figures 4.5a and 4.5b are the  $^1\text{H}$  HYSCORE simulations at 1980 G and 3100 G, respectively, for the hydrogen features seen in the quaternary complexes of TyrH. The simulations for TyrH, seen in figure 4.5, are composed of two different hydrogen interactions which represent different orientations for the PAS of the hydrogen hyperfine tensor with respect to the  $g_z$  axis. At 1980 G, the hydrogen that can be characterized with the maximum at (5.9,12.2) used a dipole-dipole coupled hydrogen with a distance of  $3.2 \pm 0.2 \text{ \AA}$  and an orientation of the hyperfine principal axis with respect to  $g_z$  of  $1.55 \pm 0.1$  rad. This hydrogen with an orientation nearly perpendicular to the  $g_z$  axis generated the cross peaks with maximum near (12.1,14.4) MHz at 3100 G. The second hydrogen,

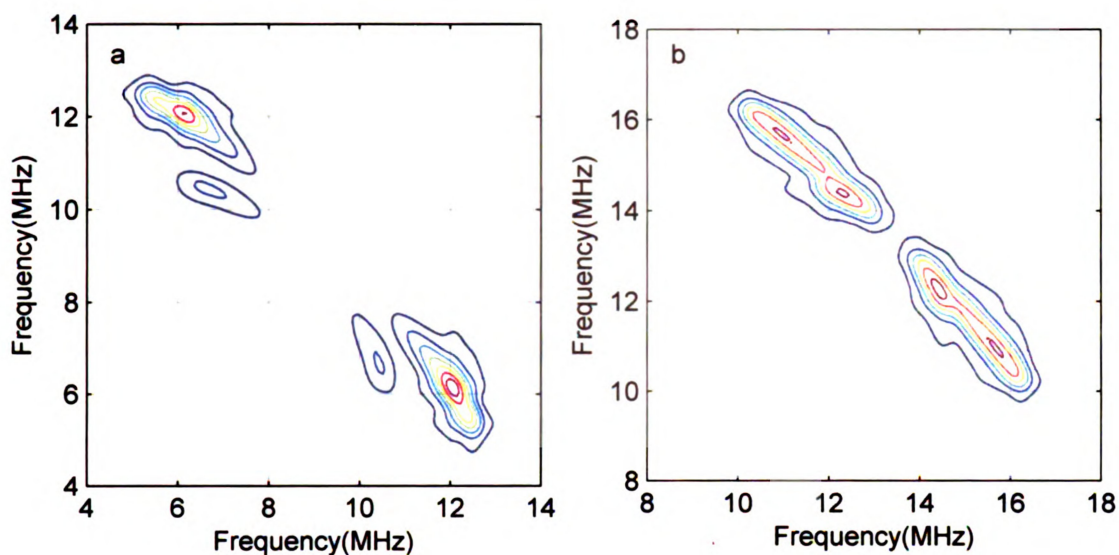
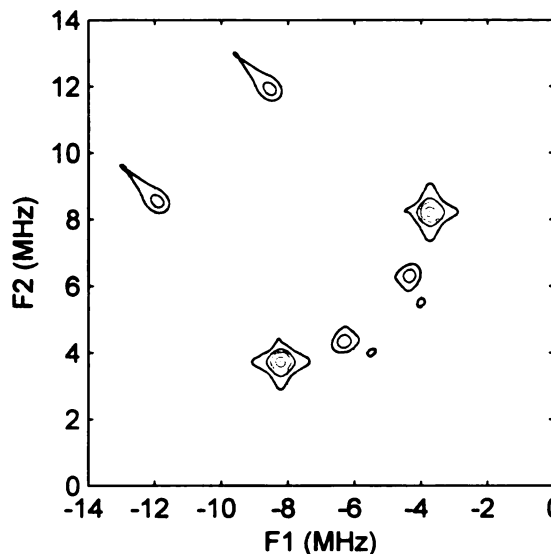


Figure 4.6:  $^1\text{H}$  HYSCORE simulations for PheH at 1980 G (a) and 3100 G (b).

characterized the maximum near (6.8,10.2) MHz at 1980G and (10.7,15.95) MHz at 3100G, used a dipole-dipole distance of  $3.16 \pm 0.2 \text{ \AA}$  and an orientation of the hyperfine principal axis with respect to  $g_z$  of  $0.34 \pm 0.1 \text{ rad}$ .

The  $^1\text{H}$  HYSCORE simulation for PheH at 1980 G and 3100 G, shown in figures 4.6a and 4.6b, respectively, used parameters similar to those utilized in the TyrH simulations. The hydrogen that can be characterized by the maximum at (6.2,12) at 1980 G and (12,14.6) MHz at 3100 G, assumed a dipole-dipole coupled hydrogen with a distance of  $3.2 \pm 0.2 \text{ \AA}$  and an orientation of the hyperfine principal axis with respect to  $g_z$  of  $1.52 \pm 0.1 \text{ rad}$ . The second hydrogen with maxima at (6.8,10.1) MHz and (10.5,16.1) MHz used a dipole-dipole distance of  $3.12 \pm 0.2 \text{ \AA}$  and an orientation of the hyperfine principal axis with respect to  $g_z$  of  $0.34 \pm 0.1 \text{ rad}$ .

The Fe-H dipolar couplings obtained from these simulations correspond well with the distances expected for the two hydrogens on the 2 and 5 position of the histidine. An



estimation, based on the ternary crystal structure of PheH<sup>11</sup> for the distance between the iron and the hydrogen's on the 2 and 5 position of the histidines is 3.1 Å – 3.8 Å. Our HYSCORE results only provide distances for two distinct hydrogen populations, this can be interpreted in one of two ways: the hydrogen's on the 2 and 5 positions share nearly the same

Figure 4.7: <sup>14</sup>N HYSCORE simulations at Fe-H distances and we only have two types of 3100 G

hydrogen which differs by orientation or only two of the four hydrogen's significantly contribute to the HYSCORE, obscuring the other two more distant and weaker components. Depending on the method that these distances are interpreted will determine how the orientation information is utilized to provide restrictions on the position of the NO bond within the active site of these enzymes.

Proper simulation of the directly coordinated nitrogen should provide more clarity to the above results and allow for a more restricted position for the NO bonding. A sample simulation for the directly coordinated nitrogen in TyrH at 3100G is shown in figure 4.7. The simulation utilized the following parameters:  $a_{iso} = 7.5$  MHz,  $T = 1$  MHz, an angle between the dipolar vector and the Fe-NO bond of 0.2 radians, and  $e^2Qq = 3.0$  MHz with an  $\eta = 0.1$ . These parameters are consistent with those observed for the directly coordinated nitrogen in the model system.

The problem with a complete analysis of the Fe-NO bond orientation within the

active site is the lack of a second nitrogen coupling unless both nitrogen's share a similar orientation with respect to  $g_z$ . In PheH we did observe a second strongly coupled nitrogen feature; however, it is likely only a small change in orientation,  $\sim 0.2$  radians. Determining the orientation of the Fe-NO within the active site will require more work on model systems, such as TauD, in which we know the NO orientation with respect to the histidine ligands

#### 4.4 EXCHANGEABLE HYDROGEN

In the field range of 2800 G – 3200 G we were able to identify the frequency components in the HYSORE spectra of the model system which represent coordinated water. In figures 4.2 and 4.4 we see a higher frequency component, one that we've previously attributed to  $H_2O$ , represented by the peaks at (12,16) MHz and (11.2,16.8) MHz, respectively. To verify that these higher frequency features were solvent, samples in  $D_2O$  were examined. It was observed that the quaternary complex of TyrH in  $D_2O$  buffer did not contain the higher frequency feature at (12,16) MHz; on the other hand, the

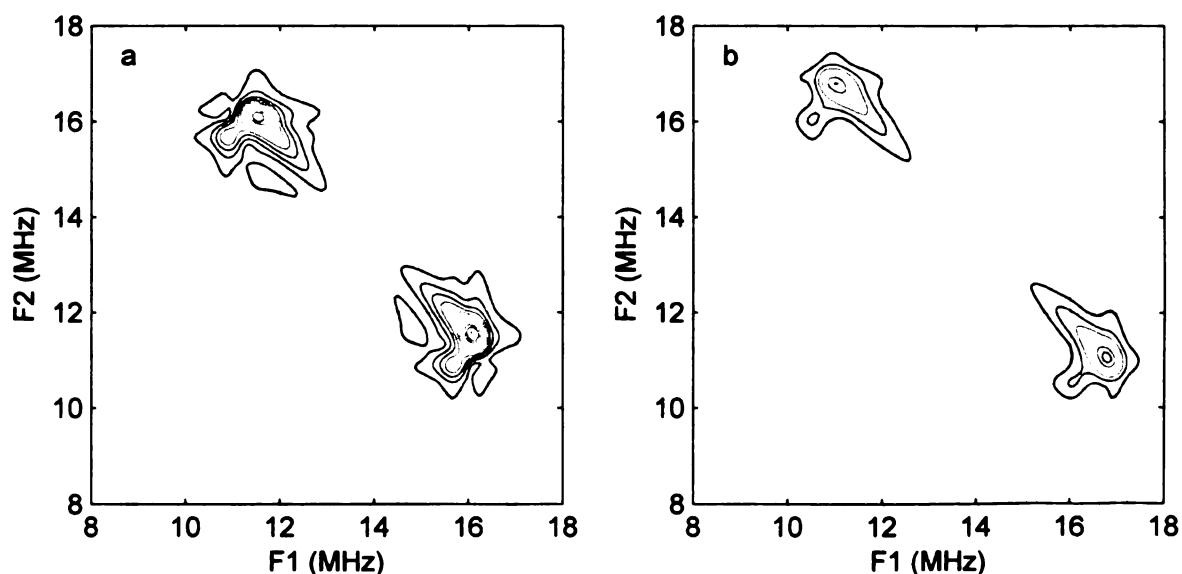


Figure 4.6:  $^1H$  HYSORE simulations at 3100 G for TyrH(a) and PheH(b).

quaternary complex of PheH in D<sub>2</sub>O buffer still contained this high frequency feature. This result was unexpected and it initially led us to conclude that TyrH had a coordinated water in the quaternary complex while PheH did not. The question to the identity of this high frequency component in PheH led us to reexamine the crystal structure of the ternary complex of PheH. It was seen that the only hydrogen, aside from water, that could be closer than 3 Å would be from the pterin, specifically if the N<sub>5</sub> position were protonated.<sup>1</sup> Our observations make sense when the specific sample preparations were considered, the PheH samples were prepared using 5-deazapterin in which the 5 position is occupied by a carbon which would contain a non-exchangeable hydrogen while the TyrH samples utilized 6-Methyltetrahydropterin with a nitrogen in the 5 position which could contain an exchangeable hydrogen.

Shown in figures 4.8a and 4.8b are the <sup>1</sup>H HYSCORE simulations, at 3100 G, for the features assumed to be the hydrogen on the 5 position of the pterin in the quaternary complex of TyrH and PheH, respectively. The TyrH simulation(fig. 4.8a) assumed a single dipole-dipole coupled hydrogen with a distance of  $2.8 \pm 0.2$  Å and an orientation of the hyperfine principal axis with respect to  $g_z$  of  $1.15 \pm 0.1$  radians. The PheH simulation(fig. 4.8b) assumed a single dipole-dipole coupled hydrogen with a distance of  $2.7 \pm 0.2$  Å and an orientation of the hyperfine principal axis with respect to  $g_z$  of  $1.10 \pm 0.1$  radians.

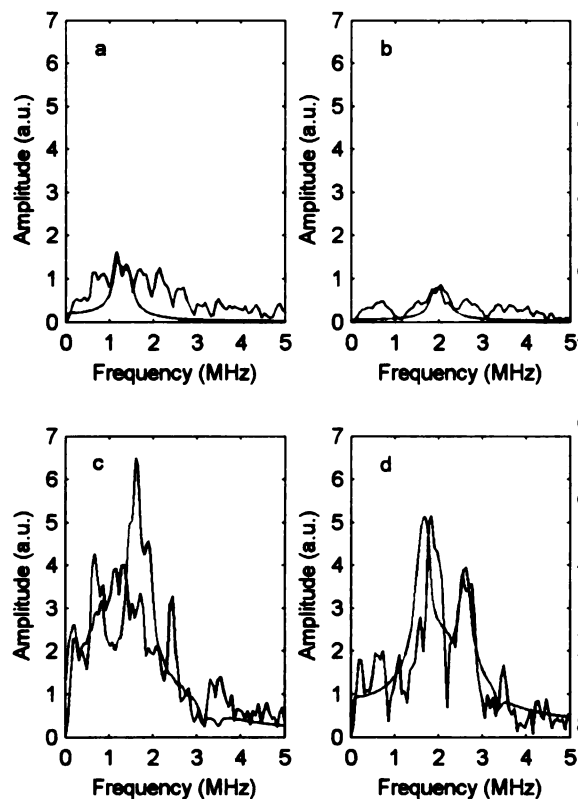
The distances provided by these results are consistent with the observation made previously(chapter 3) and those distances suggested by the crystal structure of the ternary complex of PheH. In the crystal structure of PheH, the distance measured between the Fe and the N<sub>5</sub> position on the pterin is 3.7 Å.<sup>1</sup> With a N-H bond length of approximately 1

Å, our HYSORE result for PheH of  $2.7 \pm 0.2$  Å represents the minimum Fe-H distance one could expect based on the known crystallographic data. Further confirmation of this assignment was obtained with the disappearance of this feature when the HYSORE of quaternary PheH prepared with 5,6,7- $^2\text{H}$ -5-deazapterin was examined.

#### 4.5 $^2\text{H}$ ESEEM ON PHEH

A study similar to the one described in chapter 3 on TyrH was undertaken to examine the position of the substrate and co-substrate binding in PheH. In chapter 1 we examined the CW-EPR spectra of three derivatives of  $\{\text{FeNO}\}^7$ -PheH: PheH treated with 5-deazapterin, PheH[5d], PheH treated with L-phenylalanine, PheH[Phe], and PheH treated with L-phenylalanine and 5-deazapterin, PheH[Phe, 5d]; and three derivatives of truncated  $\{\text{FeNO}\}^7$ - $\Delta$ 1-117PheH were examined:  $\Delta$ 1-117PheH treated with 5-deazapterin,  $\Delta$ PheH[5d],  $\Delta$ 1-117PheH treated with L-phenylalanine,  $\Delta$ PheH[Phe], and  $\Delta$ 1-117PheH treated with L-phenylalanine and 5-deazapterin,  $\Delta$ PheH[Phe, 5d]. The CW-EPR spectra showed changes with substrate additions; however, these changes did not provide structural information. In order to extract the substrate hyperfine information ESEEM experiments were undertaken. To isolate the interactions between the substrates and the Fe center ESEEM experiments were run in parallel with protonated substrate and selectively deuterated substrate. The time domain ESEEM results were normalized to the amplitude at the earliest time point and then divided, leaving predominately the deuterium ESEEM contribution.

Shown in figures 4.9a and 4.9b are the  $^2\text{H}$ -ESEEM spectra of  $\{\text{FeNO}\}^7$ -PheH treated with 5,6,7- $^2\text{H}$ -5-deazapterin, PheH[d-5d], at 1980 G and 3100 G, respectively.



Simulations of these spectra (red traces) assuming a single, coupled deuteron yielded a dipolar distance of  $4.5 \pm 0.2 \text{ \AA}$ , an orientation of the hyperfine principal axis with respect to  $g_z$  of  $1.1 \pm 0.1 \text{ rad}$  and an orientation between the PAS of the nuclear quadrupole and the PAS of the hyperfine tensor of  $0.6 \pm 0.1 \text{ rad}$ . When  $\{\text{FeNO}\}^7\text{-PheH}$  is treated with  $5,6,7\text{-}^2\text{H-5-deazapterin}$  and L-phenylalanine,  $\text{PheH}[\text{d-5d, phe}]$ , the  $^2\text{H-ESEEM}$  spectra acquired at 1980 G and

Figure 4.9:  $^2\text{H}$  ESEEM collected on  $\text{PheH}[\text{d-5d}]$  at (a) 1980 G and (b) 3100 G; and  $\text{PheH}[\text{d-5d, phe}]$  at (c) 1980 G and (d) 3100 G. Experimental results shown in black with corresponding simulations in red

3100 G, Figures 4.9c and 4.9d, show a significant change in amplitude as compared to the corresponding  $\text{PheH}[\text{d-5d}]$

spectra shown in Figures 4.9a and 4.9b. The red traces in figures 4.9c and 4.9d show the corresponding simulations for  $\text{PheH}[\text{d-5d, phe}]$  that result from a single deuteron with an angle between the PAS of the hyperfine tensor and  $g_z$  of  $1.10 \pm 0.1 \text{ radians}$ , a  $^2\text{H}$ -dipolar distance of  $2.7 \pm 0.2 \text{ \AA}$ , and an angle between the PAS of the nuclear quadrupole and the PAS of the hyperfine tensor of  $0.1 \pm 0.1 \text{ rad}$ .

Shown in figures 4.10a and 4.10b are the  $^2\text{H-ESEEM}$  spectra of  $\{\text{FeNO}\}^7\text{-}\Delta 1\text{-117PheH}$  treated with  $5,6,7\text{-}^2\text{H-5-deazapterin}$ ,  $\Delta\text{PheH}[\text{d-5d}]$ , at 1980 G and 3100 G, respectively. Simulations of these spectra (red traces) assuming a single, coupled deuteron

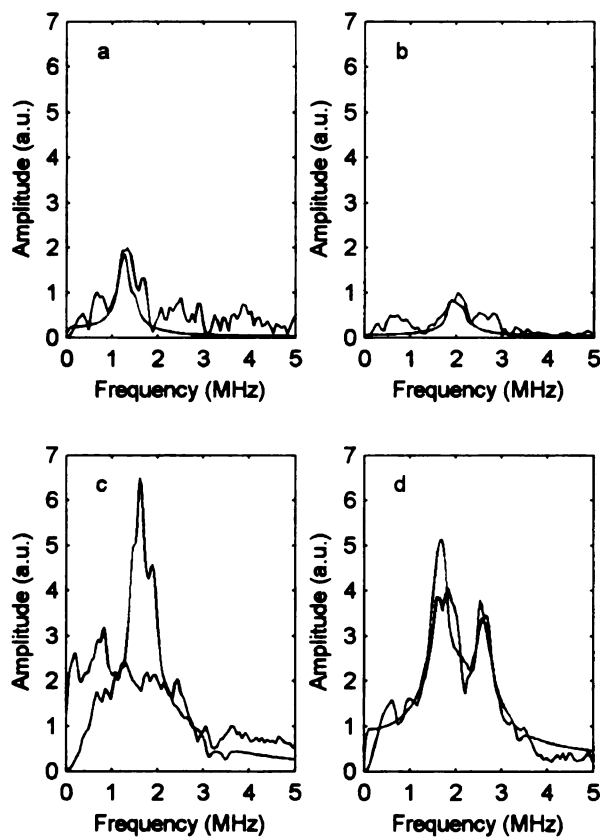


Figure 4.10:  $^2\text{H}$  ESEEM collected on  $\Delta\text{PheH}[\text{d-5d}]$  at (a)1980 G and (b) 3100 G; and  $\Delta\text{PheH}[\text{d-5d, phe}]$  at (c)1980 G and (d) 3100 G. Experimental results shown in black with corresponding simulations in red

the corresponding  $\Delta\text{PheH}[\text{d-5d}]$  spectra shown in Figures 4.9a and 4.9b. The red traces in figures 4.10c and 4.10d show the corresponding simulations for  $\Delta\text{PheH}[\text{d-5d, phe}]$  that result from a single deuteron with an orientation between the PAS of the hyperfine tensor and  $g_z$  of  $1.10 \pm 0.1$  radians, a  $^2\text{H}$ -dipolar distance of  $2.7 \pm 0.2 \text{ \AA}$ , and an angle between the PAS of the nuclear quadrupole and the PAS of the hyperfine tensor of  $0.1 \pm 0.1$  rad.

These simulations are an initial approximation for the pterin distances. Based on the deuterium labeling scheme of the pterin, up to 3 deuterons could be interacting with the Fe; however, our simulation only assumed a single deuteron. Previously (chapter 3), we discussed disregarding the interaction with the  $\text{C}_7$  deuteron based on its distance and

yielded a dipolar distance of  $4.5 \pm 0.2 \text{ \AA}$ , an orientation of the hyperfine principal axis with respect to  $g_z$  of  $1.2 \pm 0.1$  rad, and an orientation between the PAS of the nuclear quadrupole and the PAS of the hyperfine tensor of  $0.4 \pm 0.1$  rad. When  $\{\text{FeNO}\}^{7-}$  PheH is treated with 5,6,7- $^2\text{H}$ -5-deazapterin and L-phenylalanine,  $\Delta\text{PheH}[\text{d-5d, phe}]$ , the  $^2\text{H}$ -ESEEM spectra acquired at 1980 G and 3100G, Figures 4.10c and 4.10d, show a modest change in amplitude as compared to

likely ESEEM contribution. If this deuteron is disregarded, there still remains potentially two interacting deuterons. The HYSORE results described above provided a distance and orientation for what was assumed the C<sub>5</sub> hydrogen on the pterin, using these parameters <sup>2</sup>H ESEEM simulations were performed and compared to the experimental results. The simulations performed with only a single deuteron provided a reasonable fit at multiple field positions. It was also recognized that the pterin most likely binds in a similar fashion to both TyrH and PheH, this is based on the similarity of the parameters used to simulate the HYSORE feature we assigned to the C<sub>5</sub>-pterin hydrogen. Inclusion of C<sub>6</sub> deuteron, using the parameters obtained in TyrH, resulted in at most a 5% change in amplitude and a minimal line shape effect. It was therefore concluded that the ESEEM contributions from the C<sub>6</sub> deuteron is negligible and the spectrum is dominated by the more intense C<sub>5</sub> deuteron.

These results show that, much like our results in TyrH, the presence of the primary substrate effects a change in the active site which allows for closer pterin binding to the iron. It also shows that the truncated enzyme has behavior similar to that of the full length enzyme, a result which is supported by the CW-EPR spectra.

An attempt was made to examine the <sup>2</sup>H ESEEM spectra of PheH treated with para-<sup>2</sup>H-phe(d-phe). With the exception of PheH[d-phe], the ESEEM results could be characterized by a signal to noise ratio <1 and in many cases did not even have a weak line at the deuterium Larmor frequency. This led us to examine samples prepared with per-<sup>2</sup>H-phe(5d-phe), these samples did provide ESEEM, however the analysis is difficult and they were only treated qualitatively.

Shown in figures 4.11a and 4.11b are the  $^2\text{H}$  ESEEM of PheH[d-phe] at 1980 G and 3100 G, respectively. The red overlay represents a simulation which utilized a single deuteron with a dipole-dipole distance to the Fe of  $4.2 \pm 0.2 \text{ \AA}$ , an orientation of the hyperfine principal axis with respect to  $g_z$  of  $1.2 \pm 0.1 \text{ rad}$ , and an orientation between the PAS of the nuclear quadrupole and the PAS of the hyperfine tensor of  $1.4 \pm 0.1 \text{ rad}$ .

Assuming that PheH behaves in a similar fashion as TyrH with respect to primary substrate binding, PheH[d-phe] binds in a location within the active site that remains largely unchanged on co-substrate binding. If this is the case, then the above results in combination with the results from the samples treated with 5d-phe can be used to show

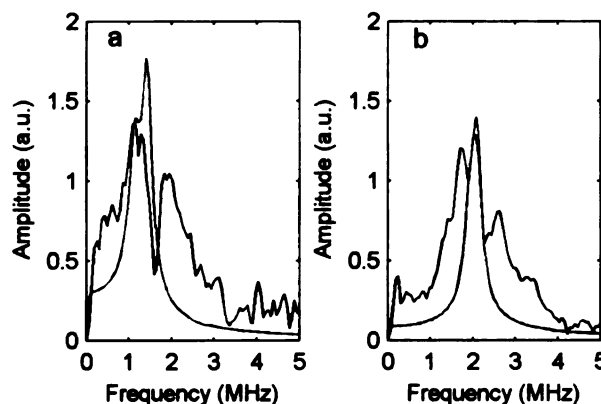


Figure 4.11:  $^2\text{H}$  ESEEM collected on PheH[d-phe] at (a) 1980 G and (b) 3100 G. Experimental results shown in black with corresponding simulations in red

the relative changes that occur on substrate binding. Using the field dependent amplitude changes described in chapter 3, we were able to observe that 5d-phe underwent a change in orientation with

respect to the  $g_z$  axis upon co-substrate addition. It was seen that the orientation of the net dipole-dipole vector went from one more perpendicular to the  $g_z$  axis to one which was one more co-linear. This result agrees with our failed observation of PheH[d-phe, 5d], if the dipole-dipole vector and the  $g_z$  axis were colinear the number of crystal orientations which contribute to the ESEEM would be greatly limited and any distribution of structures would result in a loss of ESEEM amplitude.

## 4.6 CONCLUSIONS

Using a combination of  $^1\text{H}$  HYSCORE and  $^2\text{H}$  ESEEM a portion of the control mechanism within PheH was revealed. It was shown that PheH controls pterin binding much like we've seen in TyrH. The pterin is initially positioned at a non-reactive distance from the iron with the addition of primary substrate a structural rearrangement occurs and the pterin is brought closer to the iron. These results agree very well with observations made on the crystal structures obtained on PheH.

#### **4.7 REFERENCES**

1. Andersen, O. A.; Flatmark, T.; Hough, E., Crystal Structure of the Ternary Complex of the Catalytic Domain of Human Phenylalanine Hydroxylase with Tetrahydrobiopterin and 3-(2-Thienyl)-L-Alanine, and Its Implications for the Mechanism of Catalysis and Substrate Activation. *J Mol Biol* **2002**, *320* (5), 1095-1108.

## APPENDIX I

### MATLAB SIMULATION SCRIPTS

The simulation programs were written in matlab based off the original structure written by John McCracken in Fortran. The programs include a number of improvements and fixes over the original code.

The simulation scripts are written to accept the input parameters in terms of 3 sets, the experimental parameters, the hyperfine parameters and the electron parameters. These sets of input parameters are arranged for ease of storage and usage into three matrices.

**mfile.m** – *command line syntax* – description

**parameters.m** – *[expp,hfip,gp]=parameters* – This mfile contains the three matrices and their structure used in the simulation routines. The default values in these matrices can be edited or the matrices themselves could be edited once in the workspace. expp contains the experimental parameters, hfip contains the coupling parameters, gp contains the parameters used when there is anisotropy in EPR spectrum requiring angle selection.

**sims.m** – *sims* – Program to interface the ESEEM and HYSCORE simulations into a user friendly gui. Overall the input parameters should be self explanatory.

**simplot.m** – Utility script for **sims.m**, used to plot within the gui, helps to simplify the main code.

**simprint.m** – Utility script for **sims.m**, used to "print" a simulation to a figure for printing.

**esehh.m** –  $[rawA, rawB]=esehh(expp, hfip)$  – I=1/2 3P ESEEM simulation. With an axial hyperfine interaction this will use an analytical formula for speed. When the hyperfine interaction is rhombic this will use a full density matrix calculation.

**esehhang.m** –  $[rawA, rawB]=esehhang(expp, hfip, gp)$  – I=1/2 Angular selection 3P ESEEM using a density matrix calculation

**eseho.m** –  $[rawA, rawB]=eseho(expp, hfip)$  – I=1 3P ESEEM using a density matrix calculation

**esehoang.m** –  $[rawA, rawB]=esehoang(expp, hfip, gp)$  – I=1 Angular selection 3P ESEEM using a density matrix calculation

The output from the ESEEM simulations comes into two parts pieces, rawA the alpha spin manifold and rawB the beta spin manifold. If S=3/2 is used only the S=1/2 manifold will be evaluated, specific for Fe-NO. For an S=5/2, such as Mn<sup>2+</sup>, the simulations will evaluate the five spin transitions allowed, outputting both the upper and lower manifolds into rawA and rawB respectively.

**eseassemble.m** –  $[spectra, spectraft]=eseassemble(expp, rawA, rawB, weights)$  – Used to process the raw simulation data. This will apply the product rule for multiple nuclei. Each column in rawA and rawB corresponds to a new nuclei. For example to assemble the

modulation function for two identical nuclei, rawA and rawB would each be two columns wide where each column contains the same simulation output. Alternatively with two different nuclei, column one would contain the output for nuclei 1 the second column for nuclei 2.

After the modulation functions have been assembled, the DC component is removed and the spectrum is hammed. This is followed by a fast Fourier transform which will at minimum zero-fill the spectra to maintain the number of points, further zero-filling can be added in *expp*. The output includes both the time domain spectrum and the frequency domain spectrum.

***hyschh.m*** –  $[raw]=hyschh(expp,hfip)$  – I=1/2 HYSCORE using an analytical solution

***hyschhang.m*** –  $[raw]=hyschhang(expp,hfip,gp)$  – I=1/2 angle selected HYSCORE using an analytical solution

***hyscho.m*** –  $[raw]=hyscho(expp,hfip)$  – I = 1 HYSCORE using a summation form of a density matrix calculation

***hyschoang.m*** –  $[raw]=hyschoang(expp,hfip,gp)$  – I=1 angle selected HYSCORE using a summation form of a density matrix calculation

Output from the simulation programs comes in a single matrix of two columns, the first column is the alpha manifold, second is the beta manifold. This probably won't properly handle S=5/2 since the specific weightings for the manifolds won't be taken into account.

The I=1 simulation programs are horrendously slow and do not calculate the DC

terms, this is to help with the speed. This means that the I=1 simulations will not work properly with the product rule.

**hyscprocess.m** –  $[timedom, freqdom]=hyscprocess(expp, raw)$  – Used to process the raw HYSORE spectrum. Will apply the product rule in a fashion similar to that of **eseassemble.m**, the only difference being the raw input comes in terms of two columns per nuclei, so each two columns in raw correspond to a new nuclei.

The residual DC component is removed and the spectrum is hammed in two dimensions. This is followed by a 2D fast Fourier transform which will at minimum zero-fill the spectra to maintain the number of points, further zero-filling can be added in *expp*. The output includes both the time domain spectrum and the frequency domain spectrum.

**hyscunpack.m** –  $[Z, freq1]=hyscunpack(spectra)$  – This routine will take the HYSORE output generated in Xepr, which consists of the data in a column format and converts it into a matrix for ease of plotting in Matlab.

**simtobruk.m** –  $spec=simtobruk(spectrum, frequencyscale)$  – This routine will convert the matrix representation of the HYSORE used in Matlab to a format consistent with the Bruker output.

**endorang.m** –  $rawspec=endorang(expp, hfip, gp)$  – A generic angle selected ENDOR routine that will calculate the frequency spectrum.

**endorpowder.m** –  $rawspec=endorang(expp, hfip)$  – A generic powder ENDOR routine

that will calculate the frequency spectrum.

The two ENDOR simulations are generic in the sense that they will calculate the frequency spectrum irregardless of the nuclear spin. At present however it is only equipped to calculate the  $\Delta I=1$  and  $\Delta I=2$  transitions if they are present. We have not been faced with higher order transitions so those have been neglected in the code.

The output from these simulation routines consists of two columns, the first is the frequency histogram for the alpha spin manifold, the second for the beta spin manifold. If faced with  $S \geq 5/2$  the output will consist of a column for each spin manifold much like the output from the HYSORE simulations. To properly utilize this output it needs to be sent through **engausconv.m**.

**engausconv.m** – *spec=engausconv(rawspec,expp)* – This routine will assemble the raw ENDOR frequency histograms from the simulations. The spectrum is further convoluted with a Gaussian to remove any “fence-like” appearance due to coarse integrations and too few points. The output consists of two columns, the frequency scale and the normalized intensity.

The following scripts are used within the simulation programs themselves to perform repeated functions.

**eulerrotation.m** – *[rot-hfi,rot-eeqq]=eulerrotation(hfip)* – This routine will take the nuclear hyperfine parameters stored in hfip and generate hyperfine and quadrupole tensors in the principle axis system.

**nucval.m** –  $[s, g, I_x, I_y, I_z] = \text{nucval}(a)$  – Used to store and recal the nuclear spin, g values and pauli spin matrices for a handful of commonly used nuclei.

**pareng.m** –  $[\text{theta}, \text{ncross}] = \text{pareng}(\text{freq}, \text{dth}, \text{phi}, \text{mi}, \text{field}, g1, g2, g3, a1, a2, a3)$  – This search routine is called by the simulation scripts when angle selection is needed. This is operated by taking a phi value and cycling through theta,  $0 \rightarrow \pi/2$  until the frequency is at resonance then it will cycle from  $\pi/2 \rightarrow 0$  to determine if there is a second theta which satisfies the resonance condition. Outputting the theta values in theta and the number of crossing points in ncross.

**eseft.m** –  $FT = \text{eseft}(\text{raw})$  – This routine will take partially processed spectra output from Xepr and complete the processing. Ideally the raw spectrum will have the background removed. The script will further remove any residual DC component, apply a hamming window and Fourier transform the time domain, maintaining the number of points.

**loadfiles.m** – *loadfiles* – Useful command line script to import into Matlab text files that may contain a header.

**loadcw.m** – *loadcw* – Useful command line script to import into Matlab, remove the header and normalize CW spectra exported from Xepr.

**loadtd.m** – *loadtd* – Useful command line script which imports into Matlab, removes the header, and runs through **eseft.m**, the time domain spectra exported from Xepr

**gval.m** –  $[g_x, g_y, g_z] = \text{gval}(g1, g2, g3, E/D)$  – This routine will calculate effective g values in a S=3/2 Fe-NO system.

## **Notes on simulation structure**

All of the simulations are structured in a similar fashion, within an orientation integration loop the Hamiltonian matrix is diagonalized and the spectrum is calculated. The orientation integration loop is a numerical integration performed over theta and phi using simpsons rule. It is within this loop the that Hamiltonian matrix for the specific orientations is assembled and diagonalized. The Eigenvalues and Eigenvectors are then used either in an analytical formula or a matrix expression derived through the use of the density matrix formalism of Mims, these modulation functions are then used to calculate the modulation depth over time.

## **Future Work**

The simulation scripts work and with very low instance of error produce spectra which properly reflect the input Hamiltonian parameters. This package still requires more work to be considered complete. Following is a list of work that will be necessary to reach that goal:

- A single format for the raw data output for all the different simulations.
- Re-implementation of  $S=5/2$  calculations using the ideas presented by Astashkin and Raitsimring 2002 for use with  $Mn^{2+}$ .
- Optimize and increase the speed of the simulations. The HYSCORE simulations for  $I=1$  are a specific example of one program in desperate need of optimization.
- Expand the number of different simulation to include various other pulse schemes such as 2-Pulse ESEEM, 5-Pulse ESEEM, 6-Pulse HYSCORE, Mims-

ENDOR, remims-ENDOR , etc.

## APPENDIX II

### ELECTRON SPIN ECHO ENVELOPE MODULATION SPECTROSCOPY

This appendix is to provide a brief description of the pulsed EPR experimental methods used in this thesis. These pulsed methods help to resolve the electron-nuclear hyperfine couplings that are masked by inhomogeneous broadening in the CW-EPR spectra. First, a semi-classical description of the 2-Pulse ESEEM experiment for a  $S=1/2$   $I=1/2$  spin system, loosely based on the treatments by McCracken<sup>1</sup> and/or Schweiger<sup>2</sup>, will be presented. Following this will be a basic description of the 3-Pulse ESEEM and the 4-Pulse HYSCORE experiments.

In a magnetic field the interaction between an  $S = 1/2$  electron with an  $I = 1/2$  nucleus can be represented by the Hamiltonian:

$$\hat{H} = g_e \beta_e H_0 \hat{S}_z - g_n \beta_n H_0 \hat{I}_z + \hat{S}_z \cdot A \cdot \hat{I} \quad [\text{A2.1}]$$

For this treatment of the Hamiltonian, unlike the one in chapter 2, we assume that the  $g$ -matrix is isotropic and the hyperfine interaction is axially symmetric. The diagonalization of Hamiltonian A2.1 can be performed within the individual electron spin manifolds, independent of one another, to yield the eigenvalues and eigenvectors for the NMR transitions. This is possible because  $\hat{I}$  is the only spin operator within the Hamiltonian that contains off diagonal elements, these off diagonal terms mix the nuclear states but have no effect on the electron states. The resulting NMR transitions within the  $\alpha$  and  $\beta$  electron spin manifolds are given by:

$$\omega_\alpha = \left[ \left( \omega_N + \frac{A}{2} \right)^2 + \left( \frac{B}{2} \right)^2 \right]^{1/2} \quad [\text{A2.2a}]$$

$$\omega_{\beta} = \left[ \left( \omega_N - \frac{A}{2} \right)^2 + \left( \frac{B}{2} \right)^2 \right]^{1/2} \quad [\text{A2.2b}]$$

where  $\omega_N = g_n \beta_n H_0 / \hbar$ , the nuclear Larmor frequency;  $A = a_{iso} + T(3\cos^2\theta - 1)$  and  $B = 3T\sin\theta\cos\theta$ , with  $a_{iso}$  and  $T$  being the isotropic and the dipolar hyperfine couplings and  $\theta$  is the angle between the electron-nuclear vector and the magnetic field  $H_0$ . The two electron spin manifolds are separated by  $\omega_S = g\beta_e H_0 / \hbar$ , the electron Zeeman splitting. The resulting four level system is shown in figure A2.1a:

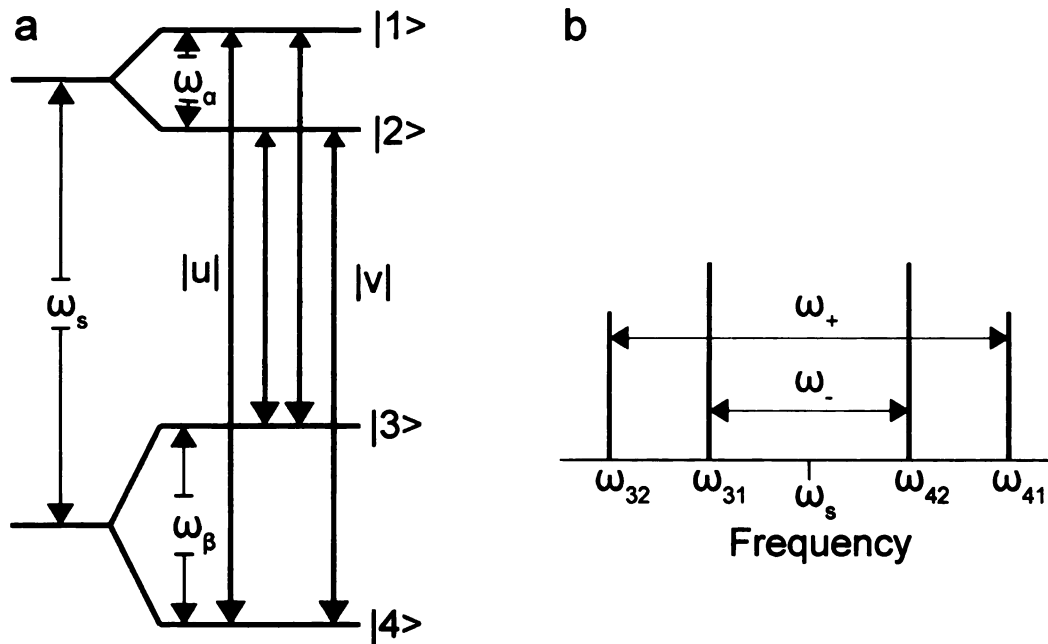


Figure A2.1: Energy level diagram(a) and the corresponding EPR spectrum(b) for an  $S=1/2$   $I=1/2$  spin system.

The off diagonal elements introduced into the Hamiltonian by the nuclear spin operator,

$\hat{I}$ , mix the nuclear sub-levels within each electron spin manifold resulting in  $m_I$  no longer being a good quantum number. The four energy levels are therefore labelled by their Eigenvector,  $|n\rangle$  where  $n=1-4$ . The normalized probability amplitude for the EPR transitions is then given by  $|u|$  and  $|v|$ . where:

$$|u| = \langle 2|\hat{S}_x|3\rangle / (0.5 g \beta H_1) = \sin\{(\varphi_\alpha - \varphi_\beta)/2\} \quad [\text{A2.3a}]$$

$$|v| = \langle 1|\hat{S}_x|3\rangle / (0.5 g \beta H_1) = \cos\{(\varphi_\alpha - \varphi_\beta)/2\} \quad [\text{A2.3b}]$$

In which  $\sin \varphi_\alpha = B/2\omega_\alpha$  and  $\sin \varphi_\beta = B/2\omega_\beta$ . Shown in figure A2.1b is the EPR spectrum corresponding to the transitions seen in the energy level diagram, where  $\omega_+ = \omega_\alpha + \omega_\beta$  and  $\omega_- = \omega_\alpha - \omega_\beta$ .

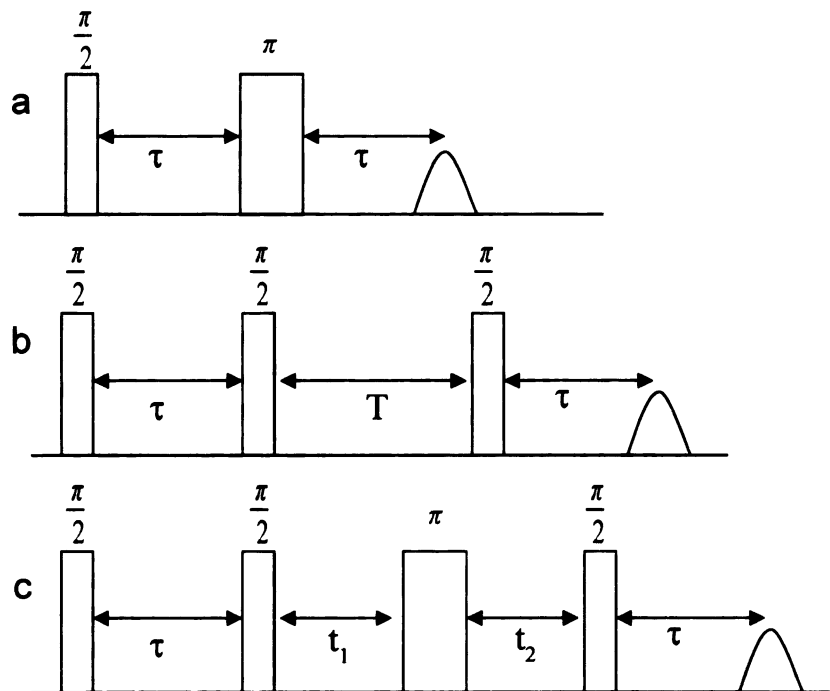


Figure A2.2: EPR pulse sequences for (a) 2-pulse ESEEM, (b) 3-pulse ESEEM, and (c) HYSCORE

The two pulse ESEEM experiment, shown in figure A2.2a, consists of a  $\pi/2$  pulse and  $\pi$  pulse separated by the time increment  $\tau$ . The intensity of the echo at time  $\tau$  after the  $\pi$  pulse is recorded as a function of incrementally increasing the pulse spacing  $\tau$ . The effect that the incremental spacing of the pulses has on the echo intensity can be understood by combining the quantum mechanical description of a four level spin system, given above, with a classical model for echo formation.

Prior to the application of the microwave pulses, the bulk magnetization of the sample,  $\mathbf{M}$ , is aligned with the laboratory magnetic field,  $H_0$ , which is directed along the z axis. In order to simplify the problem, the coordinate system is taken to rotate about the z axis at an angular frequency of  $\omega_s$ . The microwave pulses,  $H_1$ , are directed perpendicular to the z axis, in the direction of +y in the rotating frame. Application of the first  $\pi/2$  pulse torques the magnetization into the plane perpendicular to the lab axis, along +x; in addition, provided the pulse has the necessary bandwidth, it excites all four transitions seen in fig. A2.1a. The result of these transitions splits the magnetization into four spin packets with the angular frequency of the transition. During the free precession time  $\tau$ , these spin packets accumulate a phase angle with respect to the x axis. This can be seen in figure A2.1b, in a frame rotating with a frequency of  $\omega_s$ , two will precess faster moving ahead of the rotating frame and two will fall behind.

The second pulse torques the magnetization vectors  $180^\circ$  about the y-axis and leads to the formation of an electron spin echo along -x, at time  $\tau$  after the  $\pi$  pulse. Again, the pulse excites all four transitions seen in fig. A2.1a and the spin packets precess with the frequency of the transition. The spins packets that proceed through the same transition refocus along -x at time  $\tau$  producing an echo. There is however a finite probability that a portion of each spin packet branches, following a different transition, and precesses at a different angular frequency. At time  $\tau$  after the  $\pi$  pulse, the packets which underwent branching will not have refocused along the -x axis with the formation of the echo. They will instead have accumulated a phase at two different frequencies during the free precession periods and will contribute to the echo based on their projection onto the x-

axis and weighted by the probability for the branching.

This description of the two pulse ESEEM experiment can be more completely understood on examination of the analytical expression for the echo modulation of an  $S = 1/2$ ,  $I = 1/2$  spin system:

$$E_{mod}(\tau) = |u|^4 + |v|^4 + |u|^2|v|^2 \left[ 2 \cos \omega_\alpha \tau + 2 \cos \omega_\beta \tau - \cos(\omega_\alpha - \omega_\beta) \tau - \cos(\omega_\alpha + \omega_\beta) \tau \right] \quad [\text{A2.4}]$$

This equation shows that the echo is composed of the sum of the transition probabilities of the spin packets which proceed through the same transition with each pulse,  $|u|^4$  and  $|v|^4$  and the transition probability that the spin packets branch,  $|u|^2|v|^2$ . It can also be seen that the contribution to the echo amplitude by the branching transitions is modulated in time by the hyperfine frequencies and their sums and differences. Substituting A2.3a-b into A2.4 yields:

$$E_{mod}(\tau) = 1 - \frac{k}{4} \left[ 2 - 2 \cos \omega_\alpha \tau - 2 \cos \omega_\beta \tau + \cos(\omega_\alpha - \omega_\beta) \tau + \cos(\omega_\alpha + \omega_\beta) \tau \right] \quad [\text{A2.5}]$$

Where the depth of the modulation is given at:

$$k = \left[ \omega_I B / (\omega_\alpha \omega_\beta) \right]^2 \quad [\text{A2.6}]$$

Two pulse ESEEM, while useful to describe the basic principles of these techniques has proven to not be nearly as useful in the  $\{\text{FeNO}\}^7$  systems. This is due to rather fast relaxation ( $T_2^*$ ) of the spins, in practice the transverse magnetization is lost within approximately 200 ns. The principle 1-dimensional technique used in this thesis, shown in figure A2.2b, is three-pulse ESEEM which can be described with the following equation:

$$E_{mod}(\tau, T) = 1 - \frac{k}{4} \left[ 1 - \cos \omega_{\beta} \tau \right] \left[ 1 - \cos \omega_{\alpha} (\tau + T) \right] - \frac{k}{4} \left[ 1 - \cos \omega_{\alpha} \tau \right] \left[ 1 - \cos \omega_{\beta} (\tau + T) \right] \quad [\text{A2.7}]$$

The three-pulse ESEEM experiment consists of a preparation period with two  $\pi/2$  pulses separated by a fixed time period  $\tau$ . The reason for this two pulse preparation is to allow for a longitudinal evolution period, making the time dependence of the echo relatively independent of the relaxation effects from  $T_2^*$ . This preparation period however adds a secondary time dependence into the modulation function, due to the fixed nature of this time it can have a negative effect on the observed spectrum by contributing blind spots. Specific frequencies of  $\omega_{\alpha}$  will suppress the modulation of the related  $\omega_{\beta}$ , or vice versa. In this work we exploited this blind spot behavior to suppress the strongly modulating hydrogen matrix line which allowed for the higher resolution of weakly modulating nuclei.

The other method used extensively in this thesis was HYSORE spectroscopy. The basic pulse scheme for this technique is shown in fig. A2.2c. Similar to three-pulse ESEEM it begins with preparation period of two  $\pi/2$  pulses separated by a fixed time period  $\tau$ ; this style of preparation is performed for the same reasons, removal of  $T_2^*$  time dependence. HYSORE differs from three-pulse ESEEM by separating the single evolution period into two by a mixing  $\pi$  pulse, this allows for the collection of two separate time evolution periods. The resulting two-dimensional data set contains the frequency correlation between the  $\alpha$  and  $\beta$  electron spin manifolds. The portion of the modulation function due exclusively to these frequency correlations is given as:

$$S(t_1, t_2) = \frac{k}{4} C \left[ c^2 \cos(\omega_\beta t_2 + \omega_\alpha t_1 + \delta_+) + s^2 \cos(\omega_\beta t_2 - \omega_\alpha t_1 - \delta_-) \right. \\ \left. + c^2 \cos(\omega_\alpha t_2 + \omega_\beta t_1 + \delta_+) + s^2 \cos(\omega_\alpha t_2 - \omega_\beta t_1 - \delta_-) \right] \quad [\text{A2.8}]$$

Where the amplitude factor  $C = -2 \sin \omega_\alpha \tau / 2 \sin \omega_\beta \tau / 2$  and the phase factors  $\delta_+ = (\omega_\alpha + \omega_\beta) \tau / 2$  and  $\delta_- = (\omega_\alpha - \omega_\beta) \tau / 2$  contains the  $\tau$  dependence. The actual amplitudes of the modulations are equal to:

$$s^2 = \left| \frac{\omega_I^2 - (\omega_\alpha + \omega_\beta)^2 / 4}{\omega_\alpha \omega_\beta} \right| \quad [\text{A2.9a}]$$

$$c^2 = \left| \frac{\omega_I^2 - (\omega_\alpha - \omega_\beta)^2 / 4}{\omega_\alpha \omega_\beta} \right| \quad [\text{A2.9b}]$$

$$k = 4c^2 s^2 \quad [\text{A2.9c}]$$

This portion of the modulation function is useful for understanding the correlations; however, when dealing with more than a single nuclei the full modulation function which includes the DC components needs to be utilized.

## REFERENCES

1. Poole, C. P.; Farach, H. A., *Handbook of electron spin resonance : data sources, computer technology, relaxation, and ENDOR*. American Institute of Physics: New York, 1994.
2. Hanson, G., *Metals in biology*. Springer: New York, 2009.

MICHIGAN STATE UNIVERSITY LIBRARIES



3 1293 03220 8724